



Skolkovo Institute of Science and Technology

MICROSTRUCTURAL, MECHANICAL, AND THERMAL PROPERTIES  
EVALUATION OF FUNCTIONALLY GRADED FE-CU STRUCTURES AFTER  
DIRECT ENERGY DEPOSITION

*Doctoral Thesis*

by

KONSTANTIN I. MAKARENKO

DOCTORAL PROGRAM IN MATHEMATICS & MECHANICS

Supervisor  
Associate Professor Igor V. Shishkovsky

Moscow - 2023

© Konstantin Makarenko 2023

I hereby declare that the work presented in this thesis was carried out by myself at Skolkovo Institute of Science and Technology, Moscow, except where due acknowledgement is made, and has not been submitted for any other degree.

Candidate (Konstantin Makarenko)

Supervisor (Prof. Igor Shishkovsky)

## Abstract

This study is related to fabrication of SS 316L – bronze FGMs via the DED and investigation of their microstructural, mechanical, and thermal properties. Crystallization rate and dendritic structure parameters were measured via numerical methods, optical, and scanning electronic microscopy. Phase and elemental composition of the alloys were found by EDX and XRD methods. Mechanical strength, microhardness, elasticity modulus, yield stress, Poisson's ratio, and other mechanical characteristics were experimentally determined by tensile testing and microhardness measurements. It was found that the difference in microstructural parameters caused by varying operation conditions, chemical composition, and deposition strategies led to significant scatter in mechanical properties of the resulting alloys. The DIC method showed the alternating character of the principal strain distribution in the gradient specimens. The existence of  $\delta$ -ferrite in UNS C61800-based non-gradient alloys slowed grain growth, increased mechanical strength, and reduced the fatigue properties. Precipitations of  $\text{Cr}_2\text{O}_3$  and  $\text{MnO}$  were reasons for the yield strength increase of these structures. The absence of the  $\delta$ -ferrite in the alternating-layered C61800 + SS materials and their less grain refinement diminished the mechanical parameters. Thermal characteristics of these materials were analyzed by the DSC. Long-term phase transitions and the formation of lower bainite lead to a decrease in specific heat capacity and its subsequent increase. Rapid polymorphic transformations caused appearance of small exothermic peaks in the DSC curves of Fe-Cu-Cr alloys.

The results of the research can be used for producing functionally graded parts from SS 316L with Al, Sn, and Cr bronzes for aerospace, automotive, nuclear, electronics/optoelectronics, tooling, medicine, defense, and milling areas of industry.

Keywords: direct energy deposition (DED), functionally graded materials (FGMs), sandwich structures, heterogeneous Fe-Cu system alloys, digital image correlation (DIC), ultrasonic-assisted DED, SS 316L, aluminium bronze, dendritic structure, crystallization rate, coefficient of linear thermal expansion (CLTE), differential scanning calorimetry (DSC), microhardness

## Publications

1. Makarenko K, Konev S, Dubinin O, and Shishkovsky I. Mechanical Characteristics of Laser-deposited Sandwich Structures and Quasi-homogeneous Alloys of Fe-Cu System. *Materials & Design* **2022**, *224*, 111313. DOI: 10.1016/j.matdes.2022.111313
2. Makarenko K, Dubinin O, and Shishkovsky I. Linear Thermal Expansion and Specific Heat Capacity of Cu-Fe System Laser-Deposited Materials. *Metals* **2023**, *13(3)*, 451. DOI: 10.3390/met13030451
3. Makarenko K, Dubinin O, and Shishkovsky I. Analytical Evaluation of the Dendritic Structure Parameters and Crystallization Rate of Laser-deposited Cu-Fe Functionally Graded Materials. *Materials* **2020**, *13(24)*, 5665. DOI: 10.3390/ma13245665
4. Makarenko K, Dubinin O, Shornikov P, and Shishkovsky I. Specific Aspects of the Transitional Layer Forming in the Aluminium Bronze – Stainless Steel Functionally Graded Structures After Laser Metal Deposition. *Procedia CIRP* **2020**, *94*, pp. 346–51. DOI: 10.1016/j.procir.2020.09.143
5. Makarenko K, Dubinin O, and Shishkovsky I. Perspective Chapter: Direct Energy Deposition of Cu-Fe System Functionally Graded Materials – Miscibility Aspects, Cracking Sources, and Methods of Assisted Manufacturing. Chapter in book: *Advanced Additive Manufacturing*. **2022**. DOI: 10.5772/intechopen.102562
6. Makarenko K, and Shishkovsky I. Direct Energy Deposition of Cu-Fe System Functionally Graded Structures. *IOP Conference Series: Materials Science and Engineering* **2020**, *969*, 012104. DOI: 10.1088/1757-899X/969/1/012104

## **Acknowledgements**

Konstantin Makarenko expresses gratitude to his supervisor Professor Igor V. Shishkovsky and to his co-author Oleg N. Dubinin. The author of this thesis is also grateful to the instructors of the Bauman Moscow State Technical University MT12 department for the great technical education, and to Nikolay N. Kolachevsky, head of the Lebedev Physical Institute, who was the first person who gave to author the opportunity to join Skoltech and become its part for years.

## Table of Contents

Abstract .....	3
Publications .....	4
Acknowledgements .....	5
Table of Contents .....	6
List of Symbols, Abbreviations .....	10
List of Figures .....	12
List of Tables .....	17
<b>I LITERATURE REVIEW .....</b>	<b>18</b>
<b>Chapter 1. Introduction. Practical Application and Manufacturability of Fe-Cu FGMs</b>	<b>18</b>
<b>Chapter 2. State of the Art .....</b>	<b>21</b>
2.1 FUNCTIONALLY GRADED MATERIALS (FGMS).....	21
2.1.1 SYSTEMS OF FGMS .....	22
2.1.2 NI-CU AND FE-CU FGMS .....	24
2.2 DIRECT ENERGY DEPOSITION TECHNOLOGY AND ITS COMPARISON WITH TRADITIONAL METHODS.....	25
2.3 MICROSTRUCTURE EVALUATION METHODS FOR THE DED .....	38
2.3.1 RELEVANT THEORY. THE DIFFUSION OF ELEMENTS AND THE PARAMETERS OF DENDRITES .....	38
2.3.2 RELEVANT THEORY. THE CRYSTALLIZATION RATE .....	42
2.4 PHYSICAL SPECIFICITY OF FE-CU SYSTEM.....	44
2.5 ISSUES AND CHALLENGES OF FE-CU SYSTEM.....	49
2.5.1 HOT CRACKING .....	50

2.5.2 LIQUATION CRACKING.....	50
2.5.3 DUCTILITY DIP CRACKING.....	51
2.5.4 COLD CRACKING.....	51
2.5.5 REWARMING CRACKING.....	53
2.5.6 SUMMARY.....	54
2.6 EXPERIMENTAL METHODS.....	55
2.6.1 OPTICAL MICROSCOPY.....	56
2.6.2 SCANNING ELECTRONIC MICROSCOPY.....	56
2.6.3 ENERGY-DISPERSIVE X-RAY SPECTROSCOPY.....	56
2.6.4 X-RAY DIFFRACTION ANALYSIS.....	56
2.6.5 DIGITAL IMAGE CORRELATION (DIC) ANALYSIS.....	57
2.6.6 MICROHARDNESS MEASUREMENT.....	58
2.6.7 MEASUREMENT OF COEFFICIENT OF LINEAR THERMAL EXPANSION.....	58
2.6.8 DIFFERENTIAL SCANNING CALORIMETRY.....	58
2.6.9 VIBRATING SAMPLE MAGNETOMETRY.....	59
2.7 THESIS RESEARCH PROBLEM STATEMENT.....	59
<b>II EXPERIMENTAL PART.....</b>	<b>61</b>
<b>Chapter 3. Experimental Research of Deposition Strategies: Direct Joining, Alternating Layers' Techniques, and Gradient Path Method.....</b>	<b>61</b>
3.1 MATERIALS, METHODS, AND EQUIPMENT.....	62
3.2 DIRECT JOINING SS 316L AND BRONZE.....	64

3.3 ALTERNATING SS316L AND BRONZE LAYERS .....	65
3.4 FABRICATION OF SS 316L – BRONZE FGMS USING THE GRADIENT PATH METHOD .....	67
3.5 DISCUSSION .....	68
3.6 INTERIM CONCLUSION .....	69
<b>Chapter 4. Microstructural Characteristics of SS 316L – Bronze FGMS .....</b>	<b>70</b>
4.1 MATERIALS, METHODS, AND DESIGN OF THE EXPERIMENT .....	70
4.2 SPECIFICITIES OF MICROSTRUCTURE FORMATION IN SS 316L – BRONZE FGMS.....	72
4.3 PHASE AND ELEMENTAL COMPOSITION OF SS 316L – BRONZE FGMS	75
4.4 CRYSTALLIZATION RATE AND DENDRITIC STRUCTURE OF SS 316L – BRONZE FGMS.....	78
4.4.1 EVALUATION.....	79
4.4.2 SUMMARY.....	91
4.5 INTERIM CONCLUSION .....	93
<b>Chapter 5. Mechanical Properties of SS 316L – Bronze FGMS .....</b>	<b>94</b>
5.1 MATERIALS, METHODS, AND DESIGN OF EXPERIMENT .....	94
5.2 RESULTS OF TENSILE TESTING AND THEIR CORRELATION WITH MICROSTRUCTURE OF MATERIALS .....	95
5.3 DIC ANALYSIS.....	104
5.4 FRACTURE ANALYSIS .....	111
5.5 MICROHARDNESS ANALYSIS .....	118

5.6 INTERIM CONCLUSION .....	122
<b>Chapter 6. Thermal Properties of SS 316L – Bronze FGMS .....</b>	<b>125</b>
6.1 MATERIALS, METHODS, AND DESIGN OF EXPERIMENT.....	125
6.2 COEFFICIENT OF LINEAR THERMAL EXPANSION OF SS 316L – BRONZE FGMS.....	125
6.2.1 EXPERIMENTAL MEASUREMENT OF CLTE .....	125
6.2.2 ANALYTICAL ESTIMATION OF CLTE .....	126
6.2.3 NUMERICAL ANALYSIS OF THE DEPENDENCE BETWEEN THERMAL EXPANSION, TEMPERATURE, AND LASER TREATMENT PARAMETERS....	130
6.3 HEAT CAPACITY OF SS 316L – BRONZE FGMS AND ITS CORRELATION WITH CLTE .....	132
6.4 INTERIM CONCLUSION .....	136
<b>Chapter 7. Summary and Conclusion.....</b>	<b>138</b>
<b>Chapter 8. Future Research Direction.....</b>	<b>141</b>
8.1 MAGNETIC PROPERTIES OF SS 316L – BRONZE FGMS .....	142
8.2 ULTRASONIC-ASSISTED DED OF SS 316L – BRONZE FGMS .....	153
8.3 LASER DEPOSITION OF A REAL SS 316L – BRONZE GRADIENT PART	161
8.4 ADDITIONAL DIRECTIONS OF THE RESEARCH .....	164
Bibliography .....	166
Appendix.....	191

## **List of Symbols, Abbreviations**

AM – additive manufacturing

BCC – body-centered cubic

BTR – brittle temperature range

CLTE – coefficient of linear thermal expansion

CP – commercially pure

CVD – chemical vapor deposition

DED – direct energy deposition

DIC – digital image correlation

DMD – direct metal deposition

DMT – direct metal tooling

DSC – differential scanning calorimetry

EBM – electron beam melting

EBSD – electron backscatter diffraction analysis

EDX – energy-dispersive X-ray spectroscopy

FCC – face-centered cubic

FG – functionally graded

FGCM – functionally graded composite material

FGM – functionally graded material

HAZ – heat affected zone

JSC – joint stock company

LENS – laser engineered net shaping

LMD – laser metal deposition

NPP – nuclear power plants

SS – stainless steel

SEM – scanning electronic microscopy

SHS – self-propagated high temperature synthesis

SLM – selective laser melting

SLS – selective laser sintering

SMC – sheet molding compound

STP – steam turbine plants

TKR – total knee replacement

THR – total hip replacement

UA – ultrasonic-assisted

UTS – ultimate tensile strength

WAAM – wire and arc additive manufacturing

XRD – X-ray diffraction analysis

XRF – X-ray fluorescence analysis

YS – yield stress

## List of Figures

Figure 1. The illustration of the mutual bracing of the vectors $\overline{v}_{cryst}$ and $\overline{v}_{DED}$ [142] .....	42
Figure 2. The moving ellipsoid crystallization front scheme .....	43
Figure 3. A Fe-Cu system phase diagram [7,100-102,136].....	45
Figure 4. A 600 °C experimental isothermal section of the Fe-Cu-Al system ternary phase diagram [104-106] .....	48
Figure 5. Build strategies of joining a metal A and a metal B [71] .....	62
Figure 6. Configuration of the tracks' formation in a single layer of all experimental samples (left picture – layers with an odd numerical order, right picture – with an even order).....	63
Figure 7. Crack formation on a border of SS and aluminium bronze. The dark structure – aluminium bronze, the light structure – SS.....	65
Figure 8. The laser deposition scheme (a) and the resulting gradient structure (b).....	66
Figure 9. Edge effects in the gradient specimens (a,b).....	67
Figure 10. Schemes of the gradient path approaches.....	68
Figure 11. The dendritic structure of the FG specimen of group 7.....	73
Figure 12. The results of EDX analysis of group 7 ((a)—the base image, (b)—the Fe-based regions, (c)—the Cr-based regions, (d)—the Cu-based regions) .....	74
Figure 13. SEM micrographs of fabricated specimens. a-c: C61800+SS (50/50 wt.%); d-f: C61800+SS (alt.) .....	75
Figure 14. XRD pattern data of group 7. 1 <sup>st</sup> , 3 <sup>rd</sup> , 5 <sup>th</sup> , 7 <sup>th</sup> , 8 <sup>th</sup> , and 10 <sup>th</sup> peaks correspond to the $\gamma$ -Fe phase; 2 <sup>nd</sup> , 4 <sup>th</sup> , 6 <sup>th</sup> , 9 <sup>th</sup> , and 10 <sup>th</sup> – to $\alpha$ -Cr.....	77

Figure 15. The alloy structure type dependence on the solutal undercooling criteria and the admixture concentration [142,143].....	78
Figure 16. The sub-microscale porosity of the specimen .....	80
Figure 17. The SEM micrograph of the Fe-Cu FGM .....	80
Figure 18. The evaluation of the secondary elements of the dendrites sketch .....	81
Figure 19. The laser source focusing scheme .....	83
Figure 20. The crystallization rate function graph ( $[z] = m$ , $[y] = m$ , $[v_{cryst}] = m/s$ ) .....	88
Figure 21. The area of the «small dendrites» ( $z$ , $y$ , and $a$ are provided in meters).....	90
Figure 22. The width of the secondary elements of the dendrites function graph ( $z$ , $y$ , and $a$ are provided in meters).....	90
Figure 23. Stress-strain behavior of $e_{xx}$ (a) and $e_{xy}$ (b) components of a strain tensor .....	96
Figure 24. The $\sigma_{xy}$ 's behavior of group 8 .....	96
Figure 25. Distribution of principal strains in specimens of all groups before breaking. a-h: groups 1-8.....	105
Figure 26. A relationship between build direction and axes X, Y and Z.....	106
Figure 27. Frames of breaking of all groups. a: group 1; b: group 2; c: group 3; d: group 4; e: group 5; f: group 6; g: group 7; h: group 8.....	111
Figure 28. Crack at the surface of group 8 specimen (a, b).....	116
Figure 29. Selected fractography images of the specimens of all groups. a-h – groups 1-8, respectively .....	117
Figure 30. A microhardness and elasticity modulus research №1 performed with the different experimental samples' series №1 .....	119

Figure 31. A microhardness and elasticity modulus research №2 performed with the experimental samples' series №2 .....	120
Figure 32. The microhardness research results.....	120
Figure 33. CLTE of groups 1–8. The experimental CLTE for CP SS 316L was equal to $1.820 \cdot 10^{-5} \pm 9.5 \cdot 10^{-7} \text{ K}^{-1}$ .....	126
Figure 34. DSC curves of materials from groups 1-8.....	133
Figure 35. DSC curves of CP SS 316L measured during 4 cycles (measurement precision was $\pm 2.5\%$ ).....	134
Figure 36. As-deposited specimens of the Fe-Al system.....	146
Figure 37. Microstructure images of the Fe-Al specimens fabricated via the DED .....	147
Figure 38. Saturation curves of laser deposited SS-Al and SS-bronze specimens at room temperature .....	148
Figure 39. Saturation magnetization values for different concentrations of aluminium in the DED-fabricated SS 316L-Al alloy .....	150
Figure 40. The ultrasonic-assisted DED process scheme .....	154
Figure 41. The ultrasonic-assisted DED process .....	154
Figure 42. Parts fabricated: a) with ultrasonic assistance (built in a vertical direction) (left picture); b) with ultrasonic assistance (built in a horizontal direction) (middle picture); c) without ultrasonic assistance (built in a vertical direction) (right picture).....	159
Figure 43. The scheme of the blast furnace [246,247] .....	161
Figure 44. The sketch of the cooling stove .....	162
Figure 45. The resulting cooling stove after processing .....	163

**Supplementary Figures:**

Figure S.1. Engineering stress-strain curve of C61800 + SS 316L (50/50 wt.%) (group 1, specimen 1) .....191

Figure S.2. Engineering stress-strain curve of C61800 + SS 316L (50/50 wt.%) (group 1, specimen 1). .....192

Figure S.3. Engineering stress-strain curve of C18400 + SS 316L (50/50 wt.%) (group 2, specimen 1). .....192

Figure S.4. Engineering stress-strain curve of C18400 + SS 316L (50/50 wt.%) (group 2, specimen 2) .....193

Figure S.5. Engineering stress-strain curve of CB480K + SS 316L (50/50 wt.%) (group 3, specimen 1). .....193

Figure S.6 Engineering stress-strain curve of CB480K + SS 316L (50/50 wt.%) (group 3, specimen 2). .....194

Figure S.7. Engineering stress-strain curve of C61800 + SS 316L (75/25 wt.%) (group 4, specimen 1) .....194

Figure S.8. Engineering stress-strain curve of C61800 + SS 316L (75/25 wt.%) (group 4, specimen 2). .....195

Figure S.9. Engineering stress-strain curve of C18400 + SS 316L (75/25 wt.%) (group 5, specimen 1) .....195

Figure S.10. Engineering stress-strain curve of CB480K + SS 316L (75/25 wt.%) (group 6, specimen 1) .....196

Figure S.11. Engineering stress-strain curve of CB480K + SS 316L (75/25 wt.%) (group 6, specimen 2).....	196
Figure S.12. Engineering stress-strain curve of CB480K + SS 316L (75/25 wt.%) (group 6, specimen 3). .....	197
Figure S.13. Engineering stress-strain curve of C61800 + SS 316L (alt.) (group 7, specimen 1).....	197
Figure S.14. Engineering stress-strain curve of C61800 + SS 316L (alt.) (group 7, specimen 2). .....	198
Figure S.15. Engineering stress-strain curve of C18400 + SS 316L (alt.) (group 8, specimen 1). .....	198
Figure S.16. Engineering stress-strain curve of C18400 + SS 316L (alt.) (group 8, specimen 2). .....	199
Figure S.17. Engineering stress-strain curve of C18400 + SS 316L (alt.) (group 8, specimen 3). .....	199

## List of Tables

Table 1. The classifications of functionally graded composite materials (FGCMs) and solid-state methods-produced FGMs [4,6,21,22] .....	22
Table 2. Resulting parameters for copper powder deposited onto copper, aluminium, steel and titanium alloy substrates.....	35
Table 3. Physical properties of SS 316L and three bronzes fabricated by traditional technologies .....	48
Table 4. Chemical composition of the aluminium bronze .....	62
Table 5. Chemical compositions of bronzes (wt.%).....	71
Table 6. Set of groups [125]. .....	71
Table 7. Elemental concentrations in points 1-3 of SEM micrographs (Figure 10a,d) ....	76
Table 8. Mechanical characteristics of all groups.....	95
Table 9. The results of the microhardness and elasticity modulus tests performed with the experimental samples series №1 and №2 .....	121
Table 10. Analytically estimated CLTE of all groups based on the CLTE of pure metals.	128
Table 11. Experimental groups of laser deposited Fe-Al and Fe-Cu specimens .....	145
Table 12. Values of output laser power of all groups .....	145
<b>Supplementary tables:</b>	
Table S.1 Max/min values of strain tensor components $e_{xx}$ , $e_{xy}$ , and $e_{yy}$ of all groups. ....	200

## I Literature Review

### Chapter 1. Introduction. Practical Application and Manufacturability of Fe-Cu FGMs

Functionally graded materials (FGMs) with a periodical or irregular gradient of phase, structure, chemical composition, physical, and mechanical properties are widely implemented in various fields of industry. The significant interest is attributed to manufacturing FGMs of the Fe-Cu system, which combine thermal expansion properties, low friction coefficient, electrical and thermal conductivity of bronze with high rigidity, mechanical strength (yield stress, ultimate tensile strength (UTS), flexure strength, creep resistivity), and corrosion resistance of stainless steel [6]. Moreover, the Fe-Cu alloys, especially multi-layered, are characterized by significant values of magnetoresistance [7-12]. Fe-Cu FGMs are widely applied in the aerospace, nuclear, milling, automotive, defense, tooling, medicine, deep-sea exploration, super high-speed railways, electronics/optoelectronics, and other areas of industry [1–5,13]. Specific examples of Fe-Cu gradient parts include bearing bushes (parts of diesel engines), molding guide plates (critical guiding and positioning components in the moldings), cooling staves (components of blast furnaces), cartridge cases, combustion chambers, nozzles, gas vanes, fuel valves, piston crowns, bimetal pipes and wires for machinery, energy, and chemical shipping industries (including gas/liquid pipelines, condenser pipes, and heat-exchange equipment, conductive cables and springs), friction pairs of hydraulic pumps, engineering structural components (such as train pantographs and switch sliding baseplates) [13,19].

The work [20] summarizes that the materials with multifunctional properties, which can be highly sought in different fields of industry, cannot be obtained using

standard metallurgy techniques. Additive manufacturing (AM) technologies have the potential to change the paradigm for materials selection in mechanical design. AM, also known as 3D printing, is a set of various technologies associated with adding material to the substrate and making entire part without any assembly operation. It allows the cost-efficient production of parts from the FGMs with a complicated geometry in a single technological step without assembly operations, along with low waste of the material. A problem of the functionally graded (FG) structures and products synthesis via methods of AM was mentioned as early as nine years ago [3]. Earlier FGM had been made by methods of spark plasma sintering, self-propagated high temperature synthesis (SHS), thermally sprayed coating, chemical vapor deposition, photo- or electro-lithography, galvanoplasty, sol-gel process, epitaxial growth, etching technique, etc [14] according to [3]. A usage of these technologies mainly leads to creating of FG coatings (multilayer welding) instead of complete 3D parts. The more prospective 3D printing technologies for FGMs fabrication are selective laser melting (SLM), selective laser sintering (SLS), electron beam melting (EBM), wire and arc additive manufacturing (WAAM), direct energy deposition (DED) [4], also known as laser metal deposition (LMD), laser engineered net shaping (LENS<sup>TM</sup>) [16,17], 3D direct laser fabrication [18] or 3D laser cladding. The advantages of the last technology are higher performance in comparison with SLM, SLS, EBM and WAAM, low substrate deformation and the high automation of the process.

Summarizing, AM of FGMs, including Fe-Cu FGMs, is a prospective scientific and industrial track of research. Its scientific novelty and importance depend, on the one hand, on practical applicability and usability of the parts, and, on the other hand, on issues and

challenges associated with heterogeneous system of materials (Fe and Cu). It is a complicated challenge to achieve a good quality of the microstructure in the system of immiscible materials with a positive mixing enthalpy and rather different thermomechanical characteristics (thermal expansion coefficient, elasticity modulus, microhardness, thermal conductivity, thermal diffusivity, radiation absorption coefficient). At the same time, microstructural parameters (type of crystalline structure, cell parameter, grain shape and size) strongly impact on mechanical properties and other physical characteristics of these materials. The problem of microstructural and other physical properties evaluation in Fe-Cu FGMs is poorly studied in the up-to-date literature and needs to be investigated in detail. The current work is mainly devoted to researching this topic, which scientific significance is also described below in the chapter 2 «State of the Art».

## Chapter 2. State of the Art

### 2.1 Functionally Graded Materials

The choice of the specific combination and chemical composition of the conjoining base materials in FGMs depends on the required final properties of the manufactured part or the whole assembly. It can be the composition of the materials with high mechanical strength and high thermal conductivity, a base material without unique properties and materials with high antifriction characteristics (such as friction-proof bronze for bearings), high surface hardness, corrosion resistance, thermal stability and so on. Otherwise speaking, the final technical purpose and the necessary physical characteristics of the parts, assemblies or their components determine materials, phases (such as, for example, cementite, ferrite or austenite in the case of a Fe-C system) and structures (such as martensite, perlite or ledeburite of Fe-C), which form the new FGM with a gradient in an intended direction.

The first time the most important, both metallic and non-metallic, FGMs (named FGCMs—functionally graded composite materials [21]) were divided into the 16 groups was in 1995 [21,22] (Table 1, column 1). Twenty-five years after that, the authors of [4] presented the classification of FGMs in dependence on three broad groups of fabrication methods: deposition-based methods (vapor deposition, electrodeposition, thermal spray method), liquid state methods (centrifugal force methods, slip casting, tape casting, infiltration method and Langmuir–Blodgett method) and solid-state methods (powder metallurgy, friction stir welding and AM). The list of metal-based FGMs produced by the group of solid-state methods is given in Table 1, columns 2–4 [4].

**Table 1** – The classifications of functionally graded composite materials (FGCMs) and solid-state methods-produced FGMs [4,6,21,22].

FGCMs Systems [21,22]	FGMs Systems Fabricated through Powder Metallurgy Method [4]	FGMs Systems Developed via Friction Stir Welding (FSW) Method [4]	FGMs Systems Fabricated through the AM Methods (LMD/DED, SLM) [4]
SiC-SiC	Ni-Ti <sub>3</sub> AlC <sub>2</sub>	AA5083-Al <sub>2</sub> O <sub>3</sub> &SiC <sub>p</sub>	Ti6Al4V-TiC <sub>p</sub>
Al-SiC	Al2124-SiC	Pure Al-TiC <sub>p</sub>	Ti6Al4V-AlSi10Mg
SiCw-Al-alloy	Al2024-SiC	AA5083-SiC <sub>p</sub>	Ti-Al alloys
E-glass-Epoxy	Ni-Al <sub>2</sub> O <sub>3</sub>	AA6082 T6-SiC <sub>p</sub>	SS 304L-Inconel 625
Al-C	Al-Steel	Al 6061-SiC <sub>p</sub>	Ti6Al4V-Mo
Al-SiC	Al-B <sub>4</sub> C	AA6061 T6-SiC <sub>p</sub>	Fe-Cr-Ni alloy
SiCp-Al-alloy	SS 316-HA	Pure Al-Al <sub>2</sub> O <sub>3</sub> & TiC <sub>p</sub>	Ti6Al4V-TiC <sub>p</sub>
Carbon and glass fibers	SS 316L-CS	-	SS 316L-P21
Glass-Epoxy	Al2124-Al <sub>2</sub> O <sub>3</sub>	-	Ti6Al4V-Invar
TiAl-SiC fibers	ZrO <sub>2</sub> -Ni	-	Ti6Al4V-SS 304L-V
Be-Al	Cu-NbC	-	Ni-Cr-B-Si-SS 316L
Al <sub>2</sub> O <sub>3</sub> -Al-alloy	ZrO <sub>2</sub> -NiCr	-	SS 316L-IN625
Carbon-Bismaleimide	Al-SiC	-	Ti6Al4V-Al <sub>2</sub> O <sub>3</sub>
Carbon-Epoxy	AlN-Mo	-	Graded SS 316L
SiCw-6061	-	-	-
Al-alloy-CNT	-	-	-

### 2.1.1 Systems of FGMs

The list of the FGMs systems fabricated through the AM methods (Table 1, column 4) [4] lacks the several important types of metallic FGMs such as Fe-Cu system FGM [24-26], Cu-Ni [27,28], maraging-tool steel [29,30], and so on. According to the results of a deep literature review, another actual classification of the majority of metal-based FGMs (in dependence on a base material) that could be produced via AM methods can be suggested as the eight consolidated groups described below [15].

The **first** group is Ni-based FG superalloys (such as Diamalloy 1005 [31]) which are combinations of Ni, Cr and Al. These superalloys are commonly used for tools working in elevated temperatures like airfoils of turbines [32]. Such intermetallic phases as NiAl and Ni<sub>3</sub>Al, which have good oxidation resistance in intense heat conditions, even under influence of hot flows of various gases, find their application as protective coverings in aerospace and power mechanical engineering, including components of gas turbine units

and engines for missiles of diverse purposes. The advantages of these materials are their moderate density, unique mechanical characteristics under high temperatures, chemical and erosion resistance within a wide temperature range [31].

The **second** group is Ti-based FG superalloys (Co-V-Ta-Ti, Co-Ni-Al-Ti, Nb-Ti, Ti-B-Cu, Ti-Al-V-C, Ti-W-C and so on), Ti & TiO<sub>2</sub> [33], and aluminides of titanium. They are also widely used in aerospace and power industries, above all in high temperature conditions [34,35]. The area of application of these FGM is larger in comparison with pure Ti alloys. The advantages of Ti-based superalloys are higher rigidity, hardness, thermal stability, and heat resistance [36,37]. The results of investigation tests performed with TiB<sub>2</sub>-Cu FGM in conditions similar to missile operation with thermal shock influence demonstrated absence of brittle failure or cracking [38]. Ti alloys-based FG structures, as well as technically pure titanium, due to their biocompatibility also find their application in endoprosthetics [39].

The **third** group is aluminium-based FGM such as AlSi40 and Al [40] where particles of Si serve as hard reinforcements of an inhomogeneous Al-based structure. The resulted material has enhanced mechanical and chemical resistance properties in comparison with initial components [40].

The **fourth** important group is Fe-Al system (such as Fe<sub>3</sub>Al and SS 316L) FG alloys. These compounds have many special characteristics [41]: corrosion, creep and heat resistance, significant mechanical strength in high temperature conditions [42-45]. Manufacturing of these FGM is not so expensive partly owing to reasonable cost of substrates [46-48].

The **fifth** group is CoCrMo multimaterial alloys, which play an important role in biomedicine. They are used, in particular, in producing of implants for TKR (total knee replacement) and THR (total hip replacement) [49].

The **sixth** group is FG system of Ni-Cr-B-Si and steel such as SS 316L [50]. Ni-Cr-B-Si alloys are widely used in corrosive and high temperature conditions. These FGM have many different solid inclusions and are applicable for hardfacing [51].

The **seventh** group is Ti-Fe system FGM [52,53]. They combine low density, high mechanical strength and heat resistance of Ti with specific properties of steel (such as processability and lower price) [52].

The **eighth** group we should mention is Ni-Cu (including Inconel-Cu) and Fe-Cu (including steel-bronze) FG systems [24,28,54,55]. This group is a main topic of study of this work; therefore, it has to be discussed in more detail.

### *2.1.2 Ni-Cu and Fe-Cu FGMs*

Combining two aerospace alloys such as, for example, GRCo-84 and Inconel 718, allows enhancing thermophysical properties of a resulting bimetallic structure [54]. Copper allows combining good oxidation resistance in aggressive atmospheres (such as alkaline and salt) with high values of heat and temperature conductivity coefficients [28]. Nickel is a common component of high temperature alloys. Perfect notch toughness, mechanical strength, and corrosion resistance in elevated temperature conditions characterize them. High temperature strength of Ni and thermal conductivity of Cu provide usage of these FGM in extreme temperature conditions [28]. FGMs sintered using tool steel H13 and copper can be used for purposes of casting industry as materials for injection moulding

tools due to high mechanical strength, wear resistance and thermal conductivity [24]. The stainless steel and Cu combination find its application for producing of food processing, steam turbine and power nuclear plants, electronic components and so on because of mutually supportive characteristics, such as electrical and thermal conductivity of copper along with good corrosion resistance and manufacturability of SS [25].

The FGMs of the eight group are widely used in the manufacturing of space industry parts due to the mentioned physical and exploitation properties of copper and advantages of nickel alloys and stainless steel. The first steps in research of FGMs usage for the space industry were performed 18 years ago [38]. There is a description of FGMs application for producing thermal barrier materials for space shuttles and creating air and gas vanes, thrust chambers, piston tops, nosetips and so on. A radial laser deposition additive technology [20] allows producing axially symmetric gradients, such as metallic parts for spaceship elements created from carbonaceous filaments. Such gradient parts can be fabricated radially from the center of a sample to the outside.

As mentioned above, our research is devoted to the DED of the FGMs associated with eight group, their microstructural, crystallization, mechanical, thermal, and magnetic characteristics.

## **2.2 Direct Energy Deposition Technology and Its Comparison with Traditional Methods**

Several main traditional techniques for making FGMs were described in [19]: chemical vapor deposition (CVD), powder metallurgy, plasma spraying and SHS. A type of a production technology and regimes strongly influence on the properties and structure of a sintered part. For example, the research of the copper and cast-iron composites

fabrication in an induction furnace [60] demonstrated a significant influence of copper on the structure and properties of cast iron; at high concentration of copper, a phase separation in the liquid was observed. This phenomenon leads to the formation of  $\epsilon$ -copper inclusions with a composition of aluminium bronze. An increase of copper promotes the formation of lamellar perlite and decreases its interlamellar spacing. With copper concentrations less than or equal to 7 wt.%, the tendency of the alloys to form white cast iron decreases. However, when a large amount of copper is added, it acts as a strong whitening element, promoting the formation of ledeburite structure.

Another example is a research about copper coatings producing [61] by low pressure cold spraying and laser cladding techniques. The thick copper coatings of 3 mm were deposited on the SS 316L specimens using CO<sub>2</sub>-laser system with 4 kW output power and a low-pressure cold spray equipment. Various process parameters used for the laser cladding and the cold spraying were optimized in order to develop good quality coatings in terms of good metallurgical bonding of Cu and steel, good surface finish with reasonable dilution properties and low porosity. The resulted process parameters were different for both technologies and the resulted quality of parts was unequal. In this research, energy dispersive X-ray spectroscopy (EDX) of Cu cladded and cold sprayed samples has been carried out at some selected areas. In the cold spraying there was presence of 100% Cu, which was also supported by XRD (X-ray diffraction) analysis. The absence of oxides in cold spraying according to [61] could be attributed to its low temperature operation which always remains less than melting point of the particles. The traces of oxygen were found inside the coating in the laser cladding, which might be due to evolution of gases during

cladding process owing to higher process temperature (more than melting point of copper). The heat affected zone (HAZ) consisted of pure Cu interfacial layers on the melted layers of steel substrate. EDX analysis showed the presence of both copper and iron along the interface (HAZ) in the laser cladding, owing to diffusion and spattering on molten state at high working temperature during the laser processing [62,63].

It was demonstrated as a result of the research [61] that better combination of strength, density, and thermal conductivity could be achieved by cold spraying techniques in comparison with that with the laser cladding method. The adhesion strength achieved through laser cladding was found better than the low-pressure cold spraying process due to diffusion of substrate elements inside the coating during melting at the interface. No severe oxide formation was observed in both the coatings. So, it was made a decision that laser cladding can be used in the applications where moderate thermal conductivity is required with good adhesion strength, whereas, low pressure cold sprayed coatings could be used for the applications where thermal conductivity is required with moderate adhesion strength for instance electrical circuits.

DED is a reliable AM technology [64-67], which allows the rapid accurate fabrication of parts with complicated geometry from a single material or several materials simultaneously without assembly operations [20,68,69]. Mentioned aspects are common advantages of overall AM over conventional technologies [70]. These advantages are primarily provided by a layer-by-layer fabrication method and a high-resolution laser beam. The DED is the most suitable method to produce metallic FGMs with a compositional gradient in a flexible fashion [71]. This technology is widely used for

producing new parts and repairing broken ones including the case of dissimilar materials [70]. The DED provides various applications, which can change parts' properties by varying process parameters and reduce rheological instability [70]. Metallurgical issues such as residual stresses and cracks between dissimilar materials fabricated by the DED can be eliminated by various technological approaches [72]. They include making transitional areas in FGMs and performing post-treatment techniques [73]. The advantages of the DED to other AM technologies include technological availability to fabricate complex FGMs, higher productivity, and easier printing of parts with internal cavities.

Common process of the DED of an FGM can be divided into the several stages briefly described below.

a) Preheating of the substrate (optional; decreases temperature difference between substrate and material, reduces stresses and strains in the resulted part, prevents warping and the separation from the substrate [74]).

b) Laser heating of the substrate along with heating and melting of the first particles of powder, which falls on the substrate and particularly absorbs the energy from the laser beam.

c) While the laser head moves in the X-Y coordinate plane, the new powder particles becomes heated and melted; simultaneously previous areas rapidly cool down and solidify. The physical and mathematical model of the bed forming process was discussed in [75]. The presented model combined powder transportation and heating and formation of bed-like cladding in the conjugate statement. The model of bed surface growth and formation was constructed from the physical and mathematical description proposed in [28]. If the powder particles come into the melt zone, or melt in the laser beam, they adhere

to the surface, and the bead grows due to this. In this statement, it is necessary to know the parameters of the particles coming on the substrate.

The powder flow and average temperature of the particles approaching to the substrate surface  $z = 0$  could be presented as functions  $q_m(x, y)$ ,  $\widetilde{T}_p(x, y)$ , where  $q_m(x, y)$  is the function of the distribution of the particle mass flow density over the substrate surface (powder flow function),  $\widetilde{T}_p(x, y)$  is the average temperature of the particles approaching to the substrate surface  $z = 0$  [75]. The mechanism of particle adhere to the substrate is governed by the particle adhere coefficient  $E_p$ , which is  $E_p = 1$  if the powder particle is heated by the laser up to the melting point or more, and it comes into the melt-occupied area. In all other cases,  $E_p = 0$ , so such particles are excluded from the analysis.

d) When the first layer of the part is finished, the laser turns off and the powder stream stops (it may take small time delay between shutdown of the laser and moment when the last powder particles are thrown away from the powder nozzle by the feeding gas; thus, these particles can anyway sinter with substrate or previous layer and cause satellite defects such as balled-up protrusion [74,76]. These defects could be eliminated by machining, or prevented by the proper scan path planning, appropriate terminations, and suitable powder delivery [74,77,78]);

e) Cooling time between layers: a process is paused for several seconds to let the previous layer(-s) cool down. On the one hand, it prevents overheating and re-melting of previous layer(-s) (especially if they were fabricated from another material characterized by higher thermal conductivity, higher laser radiation absorption, and lower melting point)

and provides the more appropriate thermal history (therefore, in some cases, the cooling time could be artificially increased to provide more intense cooling), but on the other hand, it could increase the further undesired thermal strains and stresses due to growth of the temperature gradient, and cause cracking. Besides that, it is significantly simpler to embed the new material inside the previously fabricated layers if they are preheated.

f) The next layer is deposited on the previous, and the steps №№a)-e) are repeated; the difference from the first layer is that the heat is spread not only in the substrate, but inside the previous layer(-s) too. Depth of the laser influence  $z$ , [m] in case of laser-pulsed DED could be approximately estimated by the following equation [79]:

$$z \simeq 2 \cdot \sqrt{\frac{a \cdot \tau_p}{\pi} - \frac{T \cdot \kappa}{q}}, \quad (1)$$

where  $\tau_p$ , [s] is an average duration of the laser pulse;  $T$ , [K] is a temperature of the point with a coordinate  $z$ ;  $q$ , [W/m<sup>2</sup>] is a laser power density;  $a$ , [m<sup>2</sup>/s] and  $\kappa$ , [W/(m·K)] are a thermal diffusivity and thermal conductivity of the material respectively (in case of two or more component material it is permissible, for a first approximation, to apply the rule-of-mixture equation to estimate the average  $a$  and  $\kappa$  of the complex system).

g) The fabrication of FGM by transition from the one material to another requires gradual modification of the powder chemical composition starting from the definite layer № $n$  (gradient path method), or beginning of the layer № $n$  from completely new material (direct joining) [80]. In both these cases, a joint melt pool emerges, where both materials and the admixtures are distributed mainly by diffusion through the moving phase interface. It also should be mentioned here that the fluid motion in the melt pool could be also caused

by the pressure of vapor that evaporates from a front wall of the shallow vapor cavity [81,82] but this mechanism associated with boiling is common for several other laser treatment technologies such as laser cutting and laser alloying, but not relevant for the DED, where laser power is less than that is needed for boiling:  $P < P_{\text{boil}}$ .

Applicability of AM technologies for Fe-Cu FGMs fabrication was generally justified by the results of the following researches:

a) For the DED:

– X. Zhang et al. [83] successfully produced SS 304L – commercially pure (CP) copper FGM with ~370% average thermal diffusivity and ~100% thermal conductivity improvement in comparison with CP SS, through the intersections of a nickel-based alloy using the intermediate section technique [80];

– the authors of study [84] fabricated Fe-Cu FGM via the direct joining [80] with the resulted morphology of partially elongated columnar dendrites, and observed a microstructure refinement (up to 50  $\mu\text{m}$  grain size) due to rapid solidification rate, but identified poor yield stress (123 MPa) and UTS (250 MPa), caused by the issues of direct bonding of such dissimilar materials;

– H.S. Prasad et al. [85] deposited a 99.9% CP Cu on various metal substrates (Al, steel, and Ti) using high-absorbable green (515 nm) disk laser source instead of common industrial infrared emitters. The longitudinal cracking in case of steel-copper FGM was observed, and it was noted that the substrate preheating can be applied for the wettability of dissimilar materials improvement, which affects the resulted bonding parameters.

Engineering and physical aspects of synthesis of metal matrix FG composites such as Fe-Cu with ternary intermetallic inclusions via the DED are described in [86]. The possibility of controlling the hardness of the multilayer structure by changing the powder composition in the proposed combinatorial approach can expand the range of the 3D FG metal matrix composites applicability in the aerospace and nuclear industries. The results of the studies can be the basis for development and manufacturing of a new class of construction materials – intermetallic embedding matrix composites.

b) For other AM technologies:

– Y. Bai et al. [87] prepared the SS 316L – C52400 metal composite via the SLM with two different interfaces (transition from SS 316L to C52400 and vice versa) without any observable brittle intermetallics except CuNi;

– K.S. Osipovich et al. [88] fabricated the bimetallic samples from electrolytic tough pitch copper C11000 and SS 304 wire materials by the electron beam wire-feed AM technology with appropriate metallurgical bonding between SS and Cu with free of defects transition zone.

Besides, many other experiments were performed during last 10–15 years on the FG structures producing with Fe-Cu and similar materials using the DED. Some of them are briefly described below. For the first, we mention laser cladding technique, which is the simplest version of the DED. The last can be considered as «multilayer cladding» technology. In the study [89], the experiments on the single phosphor bronze ( $\text{Cu}_{15}\text{Sn}_{0.4}\text{P}$ ) laser cladding tracks deposited at the AISI 4340 high tensile steel surface [89] with the 1600 W diode laser with a wavelength between 915 and 976 nm were performed. The

resulting alloy demonstrated no big defects such as cracks [90], nor dilution in any sample, just a few micropores. The treatment conditions varied from 2.5 to 20 mm/s scanning speed, from 500 to 1000 W laser output power and from 200 to 400 mg/s powder rate. The powder particles had size between 150  $\mu\text{m}$  and 180  $\mu\text{m}$  and the powder was carried by argon and laterally injected in the molten pool by a convergent nozzle. The clad angle in this case was more than  $100^\circ$  in order to obtain coatings without inter-run porosity between overlapped tracks [91-93]. The microstructure of the clad coatings consisted of  $\alpha$ -dendrites surrounded by  $(\alpha+\delta)$ -eutectoid. HAZ depth was 0.4 mm and its hardness ( $630 \pm 50$  HV) was higher than that of the untreated substrate ( $335 \pm 40$  HV). The bronze coating presented the lowest hardness ( $172 \pm 12$  HV), 56% higher than the one reported for cast bronze. The increase in hardness of bronze was attributed to the fine microstructure caused by the high cooling rates during laser processing and a higher presence of the harder  $\delta$ -phase. Based on the results of this research, a laser cladding was proposed as a method to create a bronze surface in an area of a shaft as a substitute of warm shrink fitting of bronze bushes.

The research of the thick copper claddings deposited on SS 316L steel for In-vessel components of fusion reactors and copper-cast iron canisters was described in [94]. Thick pure copper claddings of 1 mm and 3 mm were deposited on the steel specimens using Cu powders of particle sizes  $< 63 \mu\text{m}$  and  $> 63 \mu\text{m}$  respectively via  $\text{CO}_2$  TRUMPF laser system with 4 kW ultimate output power. The experiment laser system consisted of a laser beam delivery system with transport optics, a nozzle incorporating powder delivery arrangement with carrier gas, a cooling system, and a laser beam shielding gas unit. The process

parameters for laser cladding were optimized in order to develop the cladded joints of a good quality in terms of good metallurgical bonding of copper and steel, good adhesion properties, low porosity and fine surface finish with reasonable dilution properties. It was observed that high power beyond 3 kW resulted into complete melting pure copper powder leading to high porosity effects in the clad layer. The laser cladding process tended to the generation of HAZ in the steel substrate; therefore, heat input had to be reduced as much as possible. The laser power less than 3 kW resulted in improper melting of the first layer and poor metallurgical bond between first layer and the substrate. There are several researches proving that the heat input required for the formation of the cladding layer reduces as the particle size decreases. Temperature of melting particles increases by using smaller size of powder. It was anticipated that both the HAZ and heat input could be decreased by reducing the size of particles [95-97]. Therefore, it was decided in research [94] to develop the 1-mm-thickness layer by using smaller particle size ( $< 63 \mu\text{m}$ ) in a single pass. It was proved that 1-mm-thickness layer can be developed properly with laser power of 3 kW in a single pass – for conserving the energy associated with each pass and cost effectiveness – with a lesser HAZ, proper dilution, proper melting, proper metallurgical bonding between the substrate, and absence of porosity.

The results of a microhardness research of manufactured specimens showed an average microhardness of the SS 316L substrate on a level of 198 HV, an average microhardness values for the 1-mm-thickness cladding and 3-mm-thickness cladding equal to 105 HV and 98 HV, respectively. The decrease in microhardness in case of 3-mm-thickness cladding might be due to increase in the size of grains ( $20 \mu\text{m}$ ) in comparison to

1-mm-thickness cladding ( $10\ \mu\text{m}$ ), thus the results were in accordance with the Hall-Petch equation.

The results of the research [94] demonstrated that the laser cladding process could be used to develop copper claddings with a thickness in the range of 1-3 mm without any significant oxidation. The cladding was found to have adhesion strength of the order of 48 MPa. The corrosion studies showed that the developed cladding can retain for many years (more than million) in active corrosion conditions. It was concluded from this study that the thickness of the cladding led to more the porosity and thicker HAZ, which finally resulted in lesser thermal conductivity. The study indicated that thermal conductivity, surface roughness, density, relative elongation, and elastic modulus are possible to be improved by refining the laser process parameters.

The research of the DED of copper on diverse metals using green laser sources was described in [98]. Green laser sources are advantageous in the processing of copper due to the increase of absorptivity compared with more commonly available infrared lasers.

Laser deposition of copper with a green laser onto various substrate metals (copper, aluminium, steel, and titanium alloy) was carried out and observed through high-speed imaging [99] in [98]. The effects of process parameters such as laser power, cladding speed and powder feed rate, and material attributes such as absorptivity, surface conditions, and thermal conductivity were tied together to explain the size and geometry of the melt pool as well as the fraction of the power used for melting material. The melt pool length and depth, dilution, incorporation time, laser power used for melting, and clad parameters

(track width and height) are collected in Table 2. Laser power was equal to 1 kW, cladding speed – 0.5 m/min, and powder feed rate – 1.3 g/min [98].

**Table 2** – Resulting parameters for copper powder deposited onto copper, aluminium, steel and titanium alloy substrates.

Substrate material	Melt pool length, mm	Track width, mm	Track height, mm	Melting depth in substrate, mm	Dilution, %	Laser power used for melting, %	Incorporation time, ms
Copper	–	1.04	0.26	0	0	0.73	0.3
Aluminium	1.74	1.4	0.24	0.306	53.2	2.94	0.1
Steel	2.60	2.34	0.14	0.382	77.5	5.15	0.2
Titanium alloy	6.49	2.96	0.26	0.706	76.2	9.78	0.1

The results of the DED of copper on copper, aluminium, steel and titanium alloy substrates carried out with a 515 nm wavelength laser system were described below.

1) The copper substrate required the highest power and the slowest cladding speed to form a continuous melt pool and clad. Aluminium, steel, and titanium alloy substrates followed the order of decreasing laser power requirement for the same cladding speed. Size and geometry of the melt pool in the process depended on multiple physical and thermal factors of the substrates as well as process parameters.

2) Incorporation of the copper powder grains in the melt was very fast and occurred within 0.1 ms for aluminium and titanium alloy substrates, but could be 0.2 and 0.3 ms for the steel and copper substrates, respectively. It was affected by a complex interdependence of multiple material properties including melt pool temperatures, melting temperatures for the various materials, viscosity, and surface tension-driven forces.

3) The oxide skin presented on melt pools could have a strong influence on powder incorporation in the case of the aluminium substrate. The scanty oxide skins on the melt

pools of steel and titanium substrates had a little effect on powder incorporation. No oxide skin was seen on the copper melt pool in the research [98].

4) The high angle and the small size of the melt pool during deposition on the copper substrate along with the longer incorporation time made the probability of powder catchment lower than that for the other substrate materials. Preheating of the substrate might improve wettability, and thus the melt pool geometry and the catchment efficiency.

5) The lower limit of percentage of laser power used purely for melting of material [98] was lowest for a single track at 0.73% (2.66% in a multilayer build) for copper deposition on copper substrate, 2.94% for the aluminium substrate, 5.15% for the tool steel substrate, and the highest at 9.78% for the titanium alloy substrate. These values were strongly influenced by the degree of absorptance of laser radiation and the thermal conductivity of the materials. The remaining power was reflected, scattered, or used for workpiece heating.

Microhardness variation from the SS 304L substrate to the Cu deposit is presented in the study [215]. Microhardness varied from 260 HV<sub>0.98N</sub> to 269 HV<sub>0.98N</sub> in the case of SS 304L and from 79 HV<sub>0.98N</sub> to 95 HV<sub>0.98N</sub> in the case of Cu. Different laser power provided changing the microhardness values of the deposited Cu track: from 86 HV<sub>0.98N</sub> to 95 HV<sub>0.98N</sub>, from 83 HV<sub>0.98N</sub> to 92 HV<sub>0.98N</sub>, and from 79 HV<sub>0.98N</sub> to 89 HV<sub>0.98N</sub> at a laser power of 1.5 kW, 1.2 kW, and 1.0 kW respectively. This increase of microhardness at a higher laser power was associated with a more Fe penetration degree.

Implementation of a new oscillating laser DED technology [193] allowed achieving 345 MPa YS and 418 UTS at 200 Hz frequency. Improving mechanical strength was

attributed to grain refinement: the grain size was reduced of 52.2% and 66.7% (down to 4.4  $\mu\text{m}$  and 7.2  $\mu\text{m}$ ) of Cu and Fe phases respectively compared to the absence of oscillation. This technique can be investigated for implementation in the frames of future studies following this thesis research.

In the significant study [173], the microstructural and mechanical characteristics of Fe-Cu DEDed alloys are given. For instance, the ultimate engineering compressive stress of studied composite samples was equal to approximately 1000 MPa in the case of  $\text{Cu}_{25}\text{Fe}_{75}$  alloy and 900 MPa of  $\text{Cu}_{50}\text{Fe}_{50}$ . Nevertheless, it was found that grains in the  $\text{Cu}_{50}\text{Fe}_{50}$  samples were significantly smaller than those in the  $\text{Cu}_{25}\text{Fe}_{75}$  alloys. This phenomenon was attributed to the differences in the effective cooling rate and grain nucleation and growth. The grain refinement was found to appear due to increased Cu content, which increased the cooling rate, and because of differences in the liquid/solid interface.

### **2.3 Microstructure Evaluation Methods for the DED**

This subchapter discusses analytic approaches, which describe the microstructural behavior of the DEDed materials including their crystallization rate and the sizes of structural elements.

#### *2.3.1 Relevant Theory. The Diffusion of Elements and the Parameters of Dendrites*

During the process of metal deposition, a crystallization front moves towards the direction of a heat flux, and the crystallites grow in the direction of the maximal temperature gradient (normally to the crystallization front surface) [142]. The solubility of the admixtures in a liquid and solid metal is different; therefore, the movement of the crystallization front induces diffusion processes. Distribution of the admixtures between

liquid and solid phases influences the drift of the alloy melting point. Therefore, the diffusion phenomena influence not only the chemical inhomogeneity of the deposited part, but its crystallization kinetics too.

The diffusion coefficients decrease with the transition of the metal from a liquid to solid state [142]. Therefore, the phase interface movement induces different diffusion equalizations of the admixtures in liquid and solid phases. In our further calculations, the diffusion equalization of the admixtures in the solid state is ignored because of the high crystallization rate of the laser deposition process.

Below, crystallization is considered as a linear process (movement of the flat crystallization front in a normal direction). This task was solved in [144,145] on the following assumptions:

1. Diffusion of dissolved matter in solid phase is insignificant;
2. Convection and non-diffuse mixing in liquid is important or insignificant;
3. The admixture distribution constant  $k$  is invariable.

We do not take into consideration the influence of the unequal temperature distribution on the diffusion fluxes of admixtures [144,145] and the influence of the phase interface distortions on admixture distribution towards the normal of this surface. In case of a laser treatment, a significant evolution of the admixtures flow normally to the isotherms is expected because of the change in the admixtures' solubility with the changing temperature. A solution to the task of the admixtures' intermixing in the consolidated part of the slab was solved in [144] in respect to the full intermixing of the admixtures in a liquid phase.

An increase in admixture concentration per second near the phase interface due to the movement of the crystallization front can be represented in the form

$$\frac{dC_l}{dt} = \frac{dC_l}{dx} \cdot \frac{dx}{dt} = v_{cryst} \cdot \frac{dC_l}{dx}, \quad (1)$$

where  $C_l$  is the admixture distribution in a liquid phase near the crystallization front, and  $v_{cryst}$  is the crystallization rate [145].

The process was considered to be steady-state; therefore, the amount of the admixture that elbows out is equal to the amount of the admixture, which diffuses in liquid. The concentration distribution near the moving phase interface is constant in time:  $dC_l/dt = 0$ . This assumption can be written as a differential equation:

$$\frac{dC_l}{dt} = D \cdot \frac{d^2C_l}{d(x')^2} + v_{cryst} \cdot \frac{dC_l}{dx'} = 0, \quad (2)$$

where  $x'$  is a coordinate in a moving coordinate system associated with the shifting phase interface, and  $D$  is the diffusion coefficient. The resulting admixture distribution is as follows:

$$C_l = C_0 \cdot \left( 1 + \frac{1-k}{k} \cdot e^{-\frac{v_{cryst}}{D}x'} \right), \quad (3)$$

where  $k$  is the admixture distribution constant as it was mentioned above. It is seen from (3) that  $C_l = \frac{C_0}{k}$  if  $x' = 0$  and the concentration exponentially falls to  $C_l = C_0$  if  $x' = \infty$ .

The criterion of the exponent increases with the growth of the crystallization rate, so the admixture concentration decreases, more rapidly moving away from the phase interface.

The value of the gradient  $dC/dx'$  determines a fall in the admixture concentration.

Derivation of Equation (3) shows

$$\frac{dC_l}{dx'} = C_0 \cdot \frac{k-1}{k} \cdot \frac{v_{cryst}}{D} \cdot e^{-\frac{v_{cryst}}{D}x'}. \quad (4)$$

It is seen from (6) that the concentration gradient has its ultimate value at the point  $x' = 0$  and then falls down up to 0 if  $x' = \infty$ . The intensity of the admixture concentration decrease increases with the growth of the crystallization rate.

The thickness of the admixture concentrating densification layer near the phase interface according to (4) is

$$\delta = x' = \frac{D}{v_{cryst}} \cdot \ln \frac{C_0 \cdot (1-k)}{k \cdot (C_l - C_0)}. \quad (5)$$

For a first approximation, according to (5), the half-width of the secondary element (secondary branch) of the dendrite may be assumed equal to the width of the concentration seal  $n_y$ :

$$n_y = \frac{D_l}{v_{cryst}} = \frac{a}{2}, \quad (6)$$

so

$$a = \frac{2 \cdot D_l}{v_{cryst}}, \quad (7)$$

where  $D_l$  is a diffusion coefficient in a liquid phase of the alloy. After estimation of the crystallization rate and the diffusion coefficient, the approximate value of the width of the secondary element of the dendrite  $a$  can be found and compared with the results of the experiments.

### 2.3.2 Relevant Theory. The Crystallization Rate

In every point of the crystallization front, the vector of the crystallization rate is normal to it [142]. The vector  $\overrightarrow{v_{cryst}}$  can be found from the equation

$$\overrightarrow{v_{cryst}} = \overrightarrow{v_{DED}} \cdot \cos\alpha, \quad (8)$$

where  $\alpha$  is an angle between a vector of a scanning speed  $\overrightarrow{v_{DED}}$  and a vector of the crystallization rate  $\overrightarrow{v_{cryst}}$  (as it is mentioned above, it is normal to the crystallization front (Figure 1)) [142]. On this basis, and as it will be demonstrated below, according to [142], it is possible to estimate a cooling rate and a temperature gradient by the analytical approach and compare the results with the experimental data to validate the theoretical model and approve its usability for the future applications.

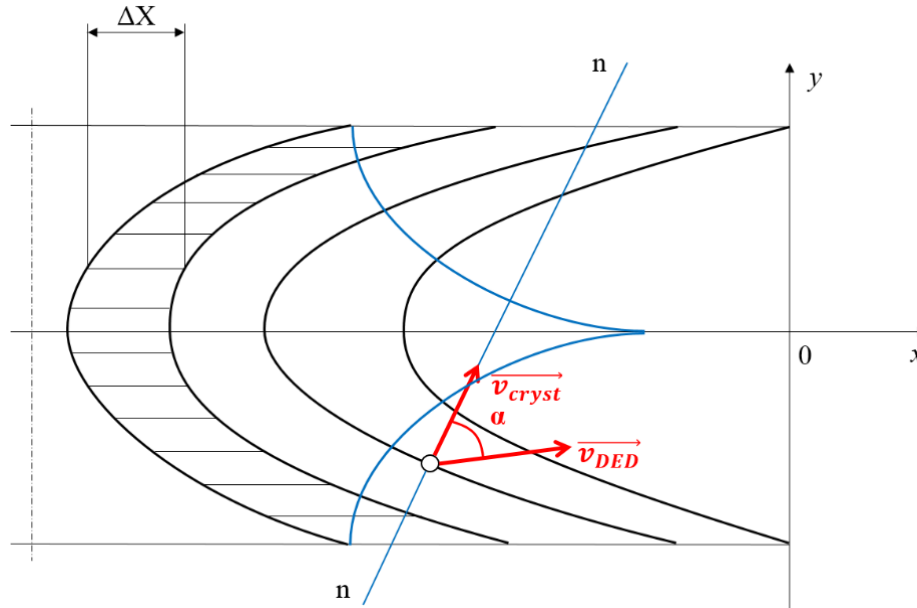


**Figure 1** – The illustration of the mutual bracing of the vectors  $\overrightarrow{v_{cryst}}$  and  $\overrightarrow{v_{DED}}$  [142].

The most common types of the crystallization front surfaces classes can be divided into the three groups: paraboloid surfaces classes, conic surfaces classes and classes of

surfaces with a knuckle line [142]. Our model was assumed as the most widespread paraboloid-type surface class with the equation

$$F(x, y, z, i) = \frac{x + i}{L} + \frac{y^2}{P^2} + \frac{z^2}{H^2} - 1 = 0, \quad (9)$$

where  $i$  is a shift of the surface class towards the  $O''x$  axis;  $L$ ,  $P$ , and  $H$  are the semi-major axes of the ellipsoid (Figure 2). Our assumption about the paraboloid surface type is spontaneous to a significant degree but allows us to make a good estimation for a first approximation. As it will be demonstrated below, our choice provided accurate results, proved by comparison with the experimental data.

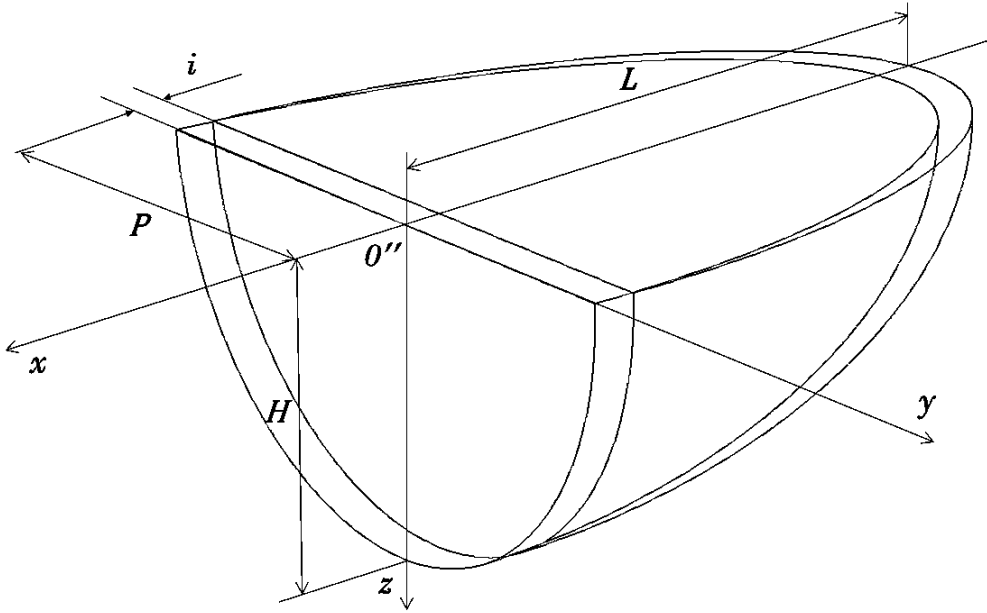


**Figure 2** – The moving ellipsoid crystallization front scheme.

A class of crystallization fronts can be submitted from (9) in a form of ellipsoids:

$$x = f(y, z) = L \cdot \sqrt{1 - \left(\frac{y}{P}\right)^2 - \left(\frac{z}{H}\right)^2} - i. \quad (10)$$

The angle  $\alpha$  between the  $O''x$  and a normal to the crystallization front surface in any point can be defined by

$$\cos\alpha = \frac{1}{\sqrt{1 + \left(\frac{\partial f(y,z)}{\partial y}\right)^2 + \left(\frac{df(y,z)}{dz}\right)^2}} \quad (11)$$

From Equation (10)

$$\frac{\partial f(y,z)}{\partial y} = -\frac{L}{P^2} \cdot \frac{y}{\sqrt{1 - \left(\frac{y}{P}\right)^2 - \left(\frac{z}{H}\right)^2}} \quad (12)$$

$$\frac{\partial f(y,z)}{\partial z} = -\frac{L}{H^2} \cdot \frac{z}{\sqrt{1 - \left(\frac{y}{P}\right)^2 - \left(\frac{z}{H}\right)^2}} \quad (13)$$

## 2.4 Physical Specificity of Fe-Cu System

The diffusion processes commonly have a positive influence on the mechanical properties of as-deposited parts due to intensification of the intermixing, but the increase of a crystallization rate (what is common for laser technologies such as DED) leads to decrease of the liquid alloy lifetime and lowers a diffusion intermixing in the liquid phase. Moreover, in specific Cu-I binary systems (where I = Fe, Co, Nb, Cr, and so on [136]), a liquid phase separation exists that prevents intermixing and makes difficulties for the desired alloy development. A discussion of this phenomenon along with parameters of temperature-and-concentration-dependent behavior of the material should be conducted using a Fe-Cu binary system phase diagram that is demonstrated in Figure 3 [7,100-102,136].

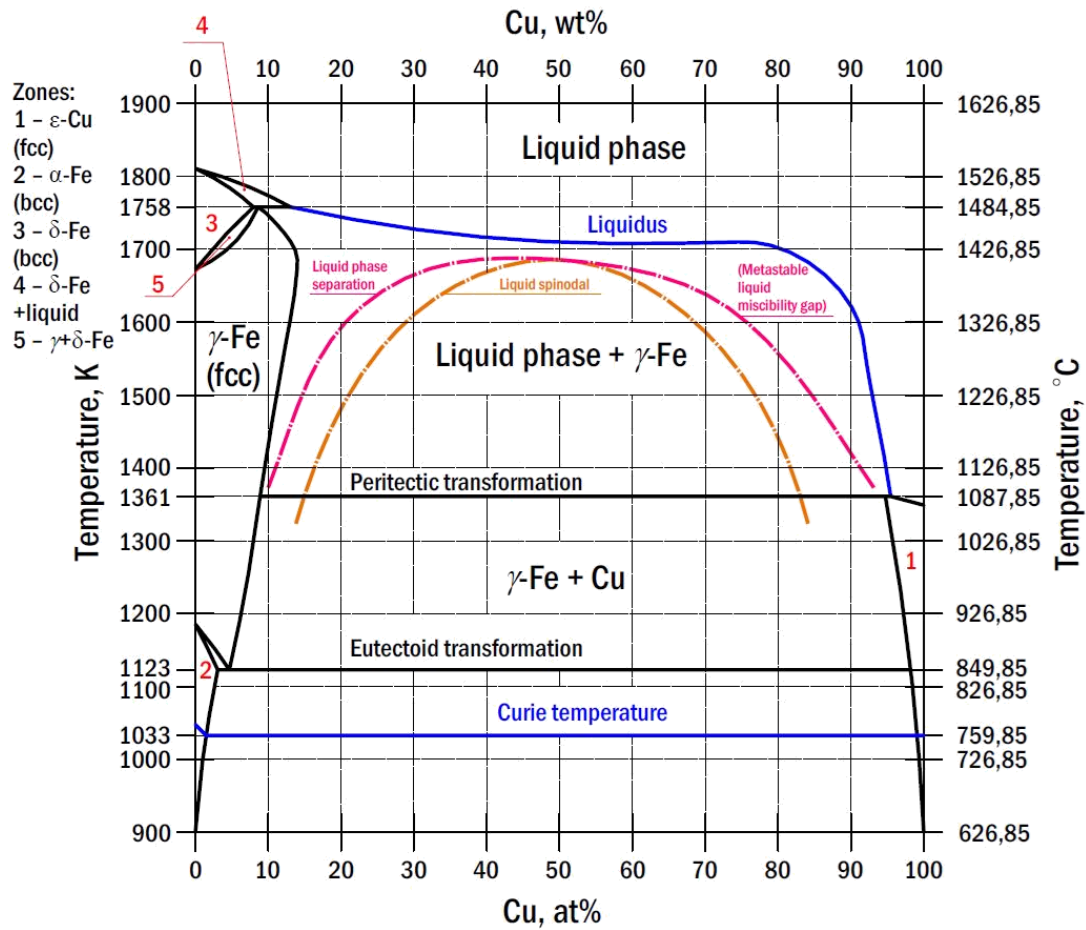


**Figure 3** – A Fe-Cu system phase diagram [7,100-102,136].

As it was mentioned above, a Fe-Cu system is characterized by existence of metastable liquid miscibility gap [7,101-103,136] (binodal, or coexistence curve), which shows a specific transient temperature for each concentration of Fe and Cu: if the liquid is undercooled below this temperature (what is convenient for rapid solidification induced by laser treatment), a liquid separation of immiscible Fe and Cu appears [136], followed by further coagulation and dendritic crystallization after cooling. A position of this gap is shown by the pink line in Figure 3. A spinodal curve [102] (orange line in Figure 3) denotes the stable states, where such separation of undercooled liquid phases isn't observed any

more (these states are located below this curve). The spinodal curve could be analytically described as a geometrical locus of points, where the Gibbs free energy second partial derivative with respect to concentration equals zero. The intersection point of these two curves (binodal and spinodal) is known as a critical point. Under that, a black horizontal line at the level of 1361 K shows the position of peritectic transformation (forming of an equilibrium solid solution consisting of a solid-state  $\epsilon$ -Cu matrix around the  $\gamma$ -Fe dendrites, from the  $\gamma$ -Fe primary phase and surrounding liquid). The next line, associated with eutectoid transformation, corresponds to the temperature of 1123 K and shows a reversible disassociation of equilibrium solid solution into the two stable phases:  $\alpha$ -Fe and  $\epsilon$ -Cu. The Curie temperature of Fe-Cu system equals to approximately 1033 K [136] (1043 K in case of pure Fe [102]) (blue line in Figure 3). The Fe-rich areas of the phase diagram (located near its left side) are characterized mostly by face-centered cubic (FCC) crystal lattice; Cu-rich (right side) – by body-centered cubic (BCC). The phases observed at different temperatures and various Fe-Cu ratios are shown in the left top side of the diagram (and titled «zones») or are specified at the coordinate plane directly.

As it was said before, the existence of a metastable miscibility gap, caused by huge positive enthalpy between Fe and Cu, has a negative influence on mechanical properties and applicability of Fe-Cu system FGMs [7]. The possible way of solution of this problem is a consideration of a ternary system Fe-Cu-X, where X is a third chemical element, which reduces the incompatibility of Fe and Cu by forming of sustainable equilibrium phases, including the case of a high-speed solidification. Aluminum could be suggested as the

possible example of this element according to the Fe-Cu-Al system ternary phase diagram shown in Figure 4 [104-106]. The Fe-Cu-Al system has three established ternary phases:

- tetragonal  $\omega\text{FeCu}_2\text{Al}_7$  ( $\omega$ , which is shown in Figure 4, is the designation of this phase with Pearson symbol  $tP40$  and space group  $P4/mnc$  [106]);
- stable icosahedral quasicrystalline  $\tau_1\text{FeCu}_2\text{Al}_6$  forming between 750 and 800 °C (I in Figure 4), which was known before as  $\psi\text{FeCu}_2\text{Al}_6$  previously found by Bradley and Goldschmidt [106] ( $\psi$  and  $\tau_1$  are the designations of this phase, which has a considerable homogeneity region of 62–66 at.% Al, 22–28 at.% Cu, and 10–12.5 at.% Fe at temperatures between 560 and 600 °C [106]);
- $\varphi\text{FeCu}_{10}\text{Al}_{10}$  ( $\varphi$ , which is shown in Figure 4, is the designation of this rhombohedral phase with space group of  $P\bar{3}m1$  and homogeneity range of 46–49.5 at.% Al, 45–51 at.% Cu, and 2–5 at.% Fe at temperatures between 560 and 620 °C [106]), which forms in a solid state and exists at 600 °C [104-106]. It was observed at 600 °C by Prevarskiy but not detected by Gayle et al. at 680 °C [106]. It is formed by a solid-state polymorphous reaction  $\beta \leftrightarrow \varphi$  at 650 °C and stabilized at lower temperatures [106].

In practice, such ternary system could be realized by using a SS – aluminium bronze FGM, which was discussed, for example, in the studies [6,118]. Other notations in Figure 4: B2 – ordered BCC phase, L – liquid phase,  $\varepsilon_2$  – binary compound  $\varepsilon_2\text{Cu}_3\text{Al}$ ,  $\delta$  – binary compound  $\delta$  in the Al-Cu system,  $\eta_1$  – binary compound  $\eta_1\text{CuAl}$ , (Al) – solid solution

based on disordered FCC Al phase,  $\beta'$  – phase separated from the solution of FeAl in the ternary system [106].

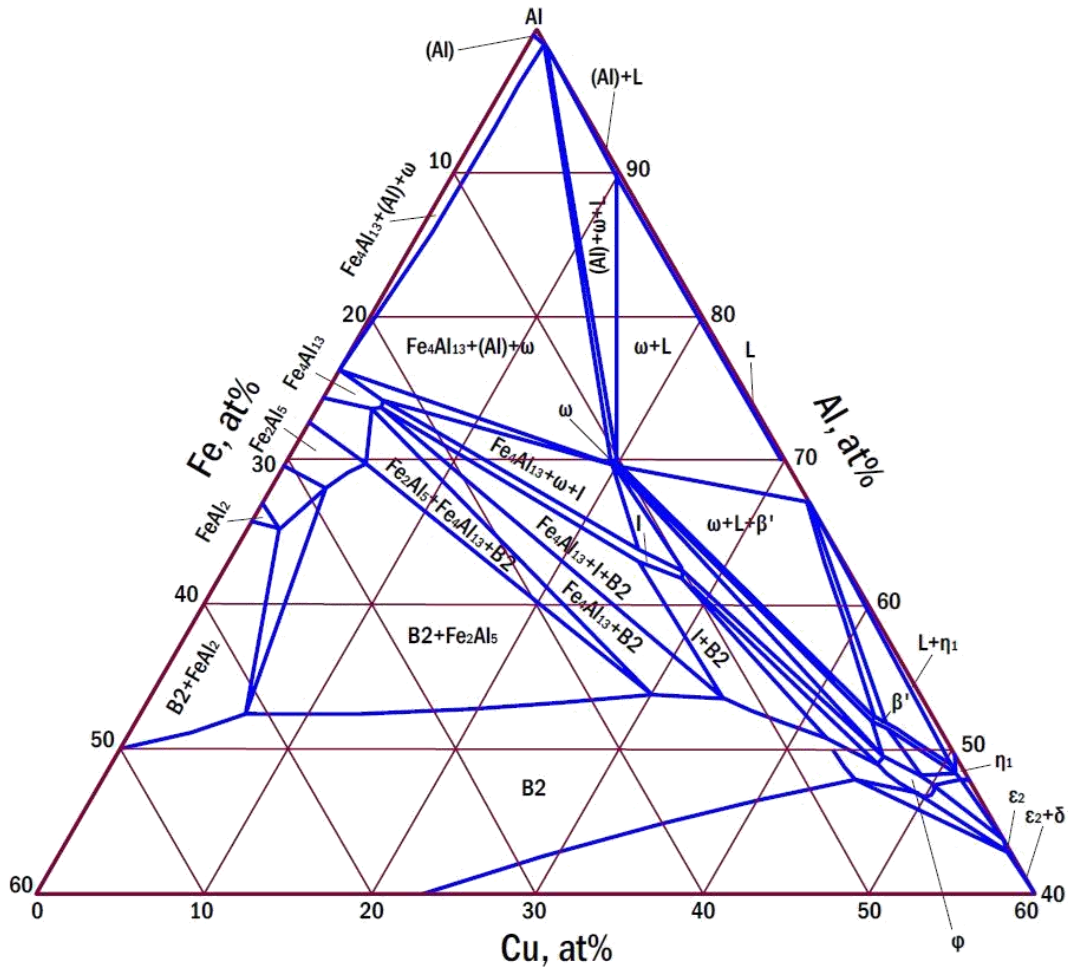


**Figure 4** – A 600 °C experimental isothermal section of the Fe-Cu-Al system ternary phase diagram [104-106].

The comparison of important physical parameters of steel (on the example of SS 316L) and bronzes (on the example of Al-based C61800, Cr-based C18400, and Sn-based CB480K, which were investigated in the current study) fabricated via traditional technologies is presented in Table 3.

**Table 3** – Physical properties of SS 316L and three bronzes fabricated by traditional technologies.

Material	Approx. linear thermal expansion coefficient	Approx. UTS, MPa	Approx. YS, MPA	Lattice type at room temperature	Lattice parameters, Å
SS 316L	$1.60 \times 10^{-5} \text{ K}^{-1}$	560	290 MPa	FCC ( $\gamma$ -Fe)	a = b = c = 3.6
C61800	$1.68 \times 10^{-5} \text{ K}^{-1}$	550	270 MPa	FCC (Cu)	
C18400	$1.65 \times 10^{-5} \text{ K}^{-1}$	280	110 MPa	FCC + BCC	
CB480K	$1.80 \times 10^{-5} \text{ K}^{-1}$	280	170 MPa	Orthorhombic (Cu <sub>3</sub> Sn)	a = 5.5; b = 4.8; c = 4.3

## 2.5 Issues and Challenges of Fe-Cu System

The key difficulties with AM of Fe-Cu system FGMs are: the stepping junction of elasticity modulus of elasticity and coefficient of linear thermal expansion during transition from Cu-based to Fe-based part; mismatch of the lattice parameters; poor mutual miscibility of steel and copper/bronze (especially during rapid solidification); embrittlement due to intermetallic phases forming [118]. The discussed factors have influence on miscibility and intermixing in liquid phase of Fe-Cu system alloys, they include possible sources of cracking of DED-fabricated Fe-Cu FGMs, and can be eliminated by the assisted manufacturing techniques, which could be used for improvement of the resulted parts quality.

During the laser treatment processes associated with melting of metal (laser welding, laser cladding, DED, SLM, SLS), the different types of cracking processes may appear. They are intensive in the case of the DED of Fe-Cu FGMs (especially at their interface areas [118]) because of significant difference between physical properties, chemical compositions of base materials, and their limited miscibility that was discussed above. Common cracking types include a hot (solidification) cracking, liquation cracking, ductility dip cracking, cold cracking, and rewarming cracking (including postweld heat

treatment cracking). Below all these types of cracking and their sources are briefly described.

### *2.5.1 Hot Cracking*

The hot cracking, also known as solidification cracking, is a brittle intercrystallite (intergranular) failure that appears along boundaries of grains during the material crystallization [107-109]. Elastoplastic strains taking place during solidification cause hot cracking if their values exceed a strain capacity of the material [79]. One of the most significant parameters at this stage is a temperature derivative of the strain:

$$\alpha = \frac{\partial \varepsilon}{\partial T}. \quad (14)$$

Thermophysical properties of base metals of the FGM, their rigidity, and the operation conditions determine a temperature derivative of the strain in the high-temperature range significantly. There is a specific temperature interval, where plasticity and strength of both components of the FGM, or of one of them, are low; it is called a brittle temperature range (BTR) [79]. This interval is characterized by decrease of plasticity and is the most probable for cracking. Overall, three factors play a leading role in forming of hot cracks:

- 1) Temperature derivative of the elastoplastic strain;
- 2) BTR range;
- 3) Minimal plasticity of the material within BTR.

### *2.5.2 Liquation Cracking*

The liquation cracking is also a kind of intergranular failure that occurs during solidification in the partially melted («mushy») zones of the material because of grain

boundary liquation [108-110]. This kind of cracking is the most common for Al-, Ni-, and Fe-based systems [110]. High thermal contraction of bronze and presence of intermetallics provokes the increase of this type of cracking in case of Fe-Cu system FGMs [108,110]. Several works state that a high-energy input of the AM could also be a reason of the liquation cracking [111,112].

### *2.5.3 Ductility Dip Cracking*

The ductility dip cracking, associated with a local ductility loss, occurs between the different grains only in a solid state of material [108,110,113,114] in an elevated temperature range of  $(0.5 \cdot T_{melt}) \lesssim T \lesssim T_{sol}$ , where  $T_{sol}$  is a recrystallization (solidus) temperature (according to the other data – in a temperature range about  $0.4 \cdot T_{melt} - 0.7 \cdot T_{melt}$  [111]). This type of cracking is actual for FCC alloys including Fe-, Ni- and Cr-based, but the systems that contain Cu also may suffer the ductility dip cracking: for instance, the Al-9Cu-6Ce (wt.%) -based AM-fabricated alloys demonstrated the ductility dip at elevated temperatures ( $\leq 400$  °C), which was attributed to a concomitant dip in a strain-rate sensitivity of deformation [115]. It should be noted that as distinguished from the liquation cracking, the ductility dip cracking doesn't exhibit a liquation [110].

### *2.5.4 Cold Cracking*

Cracking, which appears in material during its cooling at  $T \lesssim 473$  K or within several days after printing, is called cold cracking. Cold cracking has a character of a slow failure. A long-time influence of the internal residual stresses causes elastoplastic strain on the borders between different grains. Boundaries of grains have less stress resistivity

comparing with grain bodies, because the most part of the crystal lattice distortions are concentrated at the boundaries of grains [79]. Therefore, the most common areas of cold cracks appearance are boundaries of the grains. Besides, further movement of a crack may include as boundaries, as bodies of the grains. The high solidification rate, which is common for laser 3D-printing, may provide intensification of many phase transformations in material, such as  $\gamma \Rightarrow \alpha$  transformation in SS, and decrease the cold cracking resistivity. The grain refinement can contrarily increase this parameter. Overall, three most common sources of the cold cracking could be specified:

1) Source №1 is a forming of the hard and brittle phases in the material during its solidification. If some regions gain low plasticity, high hardness and increased specific volume (in other words, it may be said that these regions suffer full or partial hardening), their interface areas become saturated by the internal stresses.

2) Source №2 is an existence of the hydrogen (in several specific cases). Admixture of the hydrogen also may result in a cold cracking in case of special kinds of steels or titanium alloys. Solubility of hydrogen in these materials strongly increases while the temperature grows. Therefore, the liquid metal during the DED may include a lot of hydrogen that can be taken from the environmental gases. It is one of reasons of the necessity of the shielding gas during the DED.

3) Source №3 is a combined source. The majority of cold cracks in the real cases (specifically of steels and titanium alloys) is provided by both sources simultaneously – appearance of the low-plasticity phases along with filling with the hydrogen.

In the case of DED of Fe-Cu system FGMs, the cold cracks may be observed in three different regions of the FGM:

- in the steel area due to all three sources described before (hardening phases that appear due to transformation of austenite to martensite, inclusion of hydrogen, or combined source);

- in bronze area due to precipitation of hardening phases common for Cu-based alloys ( $\beta'$ -phase – structured solid solution based on electron compound of Cu and Zn with BCC lattice – is more usual for brasses; Sn-enriched phases, such as  $\text{Cu}_{31}\text{Sn}_8$ ; Pb-based phases); admixture of hydrogen or oxygen (the last one is the most undesired chemical element in pure copper or bronze) [79].

- in the border area if it consists of:
  - another material (in case of intermediate section method) – the source depends on the chemical composition of this material;
  - mixture of both materials (gradient path method) due to forming of the new brittle phases based on steel and bronze elements;
  - alternating layers of steel and bronze (alternating layers technique [118]) – the same as in the previous case.

If the border area is a narrow interface between steel and bronze (direct joining method), the most common types of cracking are the hot cracks and liquation cracks.

### *2.5.5 Rewarming Cracking*

The rewarming cracking that occurs due to cyclical repeated heating of the previously solidified layers is also a widespread source of cracking in the laser deposited

FGMs, including Fe-Cu system alloys. The low laser radiation absorption coefficient of copper in the infrared area of spectrum (that is common for most part of commercially available industrial fiber lasers, such as erbium-doped and ytterbium-doped) could be the trigger for the fast-appeared rewarming cracking: necessity of the high laser power implementation during the deposition of Cu-based layers leads to significant overheating of the volume of part that lays beneath; the depth of a such influence could be estimated using the equation (1). The slow-appeared rewarming cracking could appear during the heat post-treatment conducted after printing (postweld heat treatment cracking) [111], such as high tempering, that is carried out under a DED-fabricated part to decrease its residual stresses. The rewarming cracking is characterized by its own BTR, that is lower than BTR of the hot cracking, and is commonly presented by the intercrystalline failure in the coarse-grained area of the part.

#### *2.5.6 Summary*

In case of DED of Fe-Cu system FGMs, the most widespread types of cracking are hot, liquation, and rewarming cracking. Low-temperature cracking (ductility dip and cold) appears rather more uncommonly. The methods that could be suggested to struggle the cracking in these materials are:

- increase of intermixing in the interface zones that could be achieved by implementation of several specific techniques such as ultrasonic-assisted manufacturing and oscillating laser DED;

- grain refinement using such techniques as the ultrasonic vibration assistance, magnetization of the melt pool by the external field, heat treatment (e.g. annealing) by the external laser source during the printing, and oscillating laser DED;
- decrease of microstructural defects such as porosity, shrinkage cavities, unmelted particles and foreign inclusions that could appear as stress concentrators;
- exploitation of another laser sources instead of commercial fiber lasers (such as green disk solid-state lasers) with higher radiation absorption coefficient for Cu-based areas of FGM to decrease the excessive heat input into the material;
- realization of new experimental techniques such as hybrid laser-arc directed energy deposition;
- application of the intermediate section method to suppress a formation of brittle intermetallics that could be also provoked by increase of intermixing as its negative side effect;
- formation of stable phases during solidification by supplementation of additional constituents such as aluminum and nickel (e.g. D22 alloy);
- improvement of the thermal history of the alloy by changing of its fabrication process parameters;
- implementation of the alternating layers technique that could be also suggested as an effective method of cracking reduction in Fe-Cu laser-deposited FGMs.

## **2.6 Experimental Methods**

In this section, the experimental methods applied to study physical characteristics of materials in this research, are discussed.

### *2.6.1 Optical Microscopy*

Optical microscopy is a standard basic method of metallographical research. Optical focusing system allows making scaled image of the object. Magnification of this method varies from x2 to approximately x200.

### *2.6.2 Scanning Electronic Microscopy*

Scanning electronic microscopy (SEM) is a method of more detailed metallographic research. In this technique, magnification is higher than that of optical microscopy. It equals from approximately x250 to x5000 for standard microscope, and to x1000 000 – for advanced. Electron beam hits the surface of the object and removes secondary electrons from it. Their signal is collected by the receiver system, and their quantity depends on the incidence angle of the initial electrons (surface topography).

### *2.6.3 Energy-dispersive X-ray Spectroscopy*

EDX is a method of microelement analysis of various materials. In this method, electron beam focuses on the specimen's surface and provokes the emission of the X-rays. Their energy and quantity are determined by the energy-dispersive spectrometer. These parameters provide the data about the elemental composition of the target material.

### *2.6.4 X-ray Diffraction Analysis*

XRD analysis is a diffraction-based method of the material structure and phase composition research. It is based on the diffraction of X-rays on the 3D crystal cell. Diffraction angle points at possible phases, which can be found in the specimen.

### 2.6.5 Digital Image Correlation (DIC) Analysis

During tensile testing, prepared specimens are fixed in the grips of testing machines and stretched with constant or varied velocity until their failure. Tensile testing principle and conditions are described in ASTM E8/E8M-16a [116]. The results of tensile testing can be analysed using digital image correlation (DIC) approach. It is optical non-interferometric non-contact method based on the measuring the displacement of the loaded structure elements. In this method, the series of images is taken by a high-speed camera and analyzed by the DIC software. Correlation between them provides a set of the strain maps, and the stress fields can be also obtained from them.

Mechanical characteristics of the material except UTS, which is considered to be the value of tensile stress corresponding to the maximum load, can be precisely determined after tensile tests. The elasticity modulus values can be obtained from angles between linear parts of the engineering stress-strain curves and the positive abscissa axis. Also, the stiffness measurements can be performed using indenter (see subsection 5.5). The specific energy of the proportional strain can be determined as a triangle area under the stress-strain curve in the region of the proportional strain. The residual plastic part of the absolute strain  $\Delta L_{\text{plast}}$ , which persists in the specimen after its failure, the elastic part  $\Delta L_{\text{elastic}}$ , which disappears after the rupture, and their ratio  $\Delta L_{\text{plast}} / \Delta L_{\text{elastic}}$ , which indicates the stage of loading related to the failure of the specimen, can be also acquired by the stress-strain curves.

### *2.6.6 Microhardness Measurement*

Microhardness tests (and stiffness measurements too) can be performed in automatic or manual modes via microhardness measuring machines with a different kinds of hard indenters (a steel ball, a diamond cone, a triangular or four-cornered diamond pyramid). The resulted value of microhardness depends on the size of impress. An indentation force is a variable parameter, the resulting value of microhardness can be recalculated in a different scale automatically by means of machine's equipment and software.

### *2.6.7 Measurement of Coefficient of Linear Thermal Expansion*

A CLTE can be measured using different approaches. The precise approach is based on heating up to specific temperature by a heating plate or oven and subsequent strain measurements using dilatometer. A rough approach relies on using less accurate length measuring instrument such as a hand caliper or micrometer. This exact study is based on the second method.

### *2.6.8 Differential Scanning Calorimetry*

Differential scanning calorimetry (DSC) is a thermal analysis technique that measures the energy absorbed or released by a sample as a function of temperature or time [117] thus describing the thermophysical properties and phase transitions of various materials. In the current study, the specific heat capacities of eight different laser-deposited Fe-Cu alloys were experimentally determined by DSC for both heating and cooling cycles.

### *2.6.9 Vibrating Sample Magnetometry*

Vibrating sample magnetometer measures magnetic properties of materials based on the Faraday's Induction Law. The specimen placed in the machine moves up and down, and the induced electric field's current is proportional to the specimen's magnetization. The results of the measurement demonstrate the hysteresis curve.

## **2.7 Thesis Research Problem Statement**

The practical significance of the research of the DED of Fe-Cu system FGMs is reasoned by the wide range of its applications. The novelty of this topic is based on the poor current amount of scientific data in this field. Parts fabricated from Fe-Cu FGMs may work in various external conditions associated with prominent mechanical loads, high temperatures, vibration and impact loads, and can be also applied as components of electromagnetic devices [211-213]. The results of the deep literature review showed that the most of the mentioned physical properties depends on microstructural parameters (grain orientation, shape, and size, cell parameter, phase, structural, and elemental composition, presence of defects) of as-fabricated alloys. However, the specific behavior of these dependences is commonly absented in the up-to-date literature. Therefore, the microstructural, and hence – mechanical, thermal, and magnetic properties of Fe-Cu system FGMs are needed to be studied to a greater extent. Moreover, the most important direction of study in this field is the gradient transition zones between Fe-based and Cu-based sections of the FG part in respect to various building strategies. These zones are the most complicated to produce them and control their parameters due to specificities and obstacles of Fe-Cu system, first of all, limited mutual miscibility and huge gradient of

physical characteristics (thermal expansion, thermal conductivity, thermal diffusivity, elasticity modulus, radiation absorption degree, melting point) between Fe and Cu. Therefore, parameters of the transitional zones themselves have to be investigated in a deep measure to ensure fabrication of flawless Fe-Cu FG parts. Summarizing, it is needed to research microstructural properties of the mentioned alloys and their influence on meaningful mechanical characteristics (UTS, yield stress, elasticity modulus, strain-to-fracture, Poisson's ratio, residual strain, modulus of resilience, and microhardness) and thermal properties (CLTE, specific heat capacity, and correlation between them).

Also, it is needed to experimentally observe methods of improving quality of FG parts and apply the obtained results in fabrication of the prototype of the real FG Fe-Cu system part.

This thesis research is devoted to solving all the above-mentioned problems and states the prospective directions for the further studies in this field including the ultrasonic-assisted DED.

## **II Experimental Part**

### **Chapter 3. Experimental Research of Deposition Strategies: Direct Joining, Alternating Layers' Technique, and Gradient Path Method**

The first point in the experimental part of the research is the comparison of different deposition strategies and realizing the appropriate ones in the further experiments. The common techniques of FG structures synthesis are the direct joining, the gradient path method, the intermediate section method [71], and the alternating layers' technique [118] (Figure 5). The direct joining is a simplest conjunction method with a sharp transition between 100% metal A and 100% metal B. The gradient path method introduces a gradually changed path where the composition changes gradually from one component to the other by applying rule-of-mixtures to guide powder feed rates during the fabrication process. This type of gradient path is a compositional gradient that starts from 100% metal A and gradually changes to 100% metal B. The intermediate section method expands the ability to fabricate metallic FG materials from 100% metal A to 100% metal B by depositing additional materials in the middle as intermediate sections to help get rid of unwanted phases that may be easily formed in the gradient path method. Alternating layers' technique presents multilayer samples with changing single layers of the metal A and the metal B. The current was devoted to the methods, which are the most prospective for Fe-Cu system: direct joining method, which fabricated experimental samples with two sharp transitions (a lot of layers of SS, one layer of aluminium bronze, a lot of layers of SS again), alternating layers' technique, and the gradient path method.

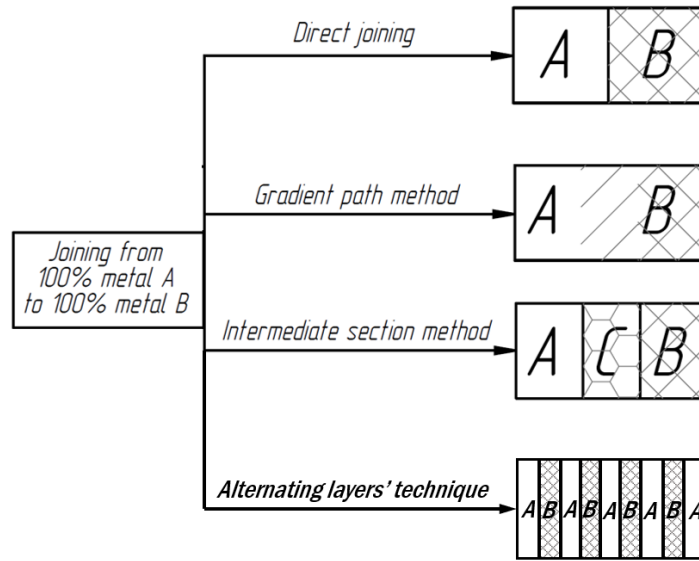


**Figure 5** — Build strategies of joining a metal A and a metal B [71].

### 3.1 Materials, Methods, and Equipment

For the experiment, three series of the experimental samples were fabricated by three mentioned build strategies. The materials used in experiments were SS AISI 316L and aluminium bronze with 10% Al content similar to UNS C61800 (fraction 45-125  $\mu\text{m}$ ). The chemical composition of SS 316L is well-known and can be found in [118]. Chemical composition of the aluminium bronze is shown in Table 4.

**Table 4** – Chemical composition of the aluminium bronze.

Chemical element	Cu	Al	Fe	Pb	Sb	Si	Sn	Zn
Content, wt.%	Base	9.5	1.0	0.02	0.05	0.1	0.05	0.05

All experiments presented in this thesis were performed using the MX-1000 (InssTek, Daejeon, Republic of Korea) technological installation working in the DMT (direct metal tooling) mode [118,119,126]. In this mode, the output laser power automatically changed during printing from the predefined minimum and maximum values

accordingly to a feedback control signal – the distance between a melt pool and a nozzle of the laser head measured using two side cameras mounted on the laser head in each moment [121]. The average output laser radiation power in case of SS was equal to 308 W, maximum power – to 450 W, and in the case of aluminium bronze these values were equal to 500 W and 750 W, respectively. Power of laser radiation was chosen in accordance with the bronze infrared radiation absorption coefficient which was lower than the same coefficient of SS. Other operation conditions were: 0.85 m/min scanning speed (the same as for all the experiments in this thesis except as otherwise noted), 3.5 g/min powder rate, 5 s cooling time between layers, and no substrate preheating. Argon was applied as a feeding and shielding gas. Gas flow rates amounted to (here and everywhere in the thesis except as otherwise specified): coaxial gas — 0.85 L/min; powder gas — 2.0 L/min; shield gas — 10.0 L/min. The geometrical parameters of the deposited powder beds here and everywhere below in the text were: bed height — 300  $\mu\text{m}$ ; layer thickness — 250  $\mu\text{m}$ ; bed width — 800  $\mu\text{m}$ ; hatch spacing — 300  $\mu\text{m}$ .

Scheme of the tracks' formation is shown in Figure 6. Width of a single track was equal to 800  $\mu\text{m}$ ; covering of the tracks (hatch spacing) – to 300  $\mu\text{m}$ .

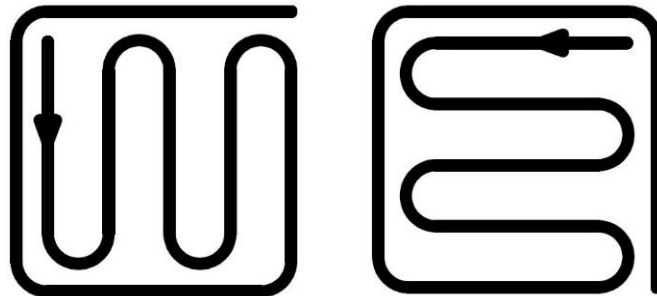


**Figure 6** – Configuration of the tracks' formation in a single layer of all experimental samples (left picture – layers with an odd numerical order, right picture – with an even order).

This configuration can be optimized further for the specific printer, which is used for DED. In this specific case, the additional belting tracks on the periphery of the part were added to remove the defect – sagging of the edges of the printed layer. The disadvantage of the presented approach is additional heat input to the edge area of the part.

A 1 kW cw-ytterbium fiber laser produced by IPG Photonics (Oxford, the United States; Russian branch – Moscow district, Fryazino) was used in the experiments here and below. Output laser wavelength was equal to a 1064 nm. Focus of a laser beam was on a 1 mm level under the surface of the piece.

Here and in all other experiments discussed in this thesis, the specimens were pressurized, grinded, and polished using TechPress 2<sup>TM</sup> and MetPrep 3<sup>TM</sup>/PH-3<sup>TM</sup> (Allied High Tech Products, Inc., CA, United States) with 6 μm minimal grain size concerning ASTM E3-11(2017) [127] and E2014-17 [129]. Microstructure images were obtained via the optical microscope Axio Scope.A1 (Carl Zeiss GmbH, Germany). All samples were previously treated with the etch (the etchant – H<sub>2</sub>SO<sub>4</sub> with ethanol and CuCl<sub>2</sub>, the etching time – from 5 to 7 s concerning E340-13 [128]).

### **3.2 Direct Joining SS 316L and Bronze**

The experimental samples series №1 (Figure 7, the bottom part of the sample is leftward) fabricated via direct joining demonstrated cracking on a border between stainless steel and aluminium bronze. We can see that the nucleus of each crack lies in the bronze part of the sample. The main task in this case is to understand what exactly was an occasion of the cracking: the powder defects (foreign deposits, defects of the shape and size), a local porosity of the part and other defects caused by issues with the treatment regimes, or the

specific aspects of a structure and a chemical composition of the deposited part, local embrittlement caused by forming of brittle and hard structures like intermetallics.

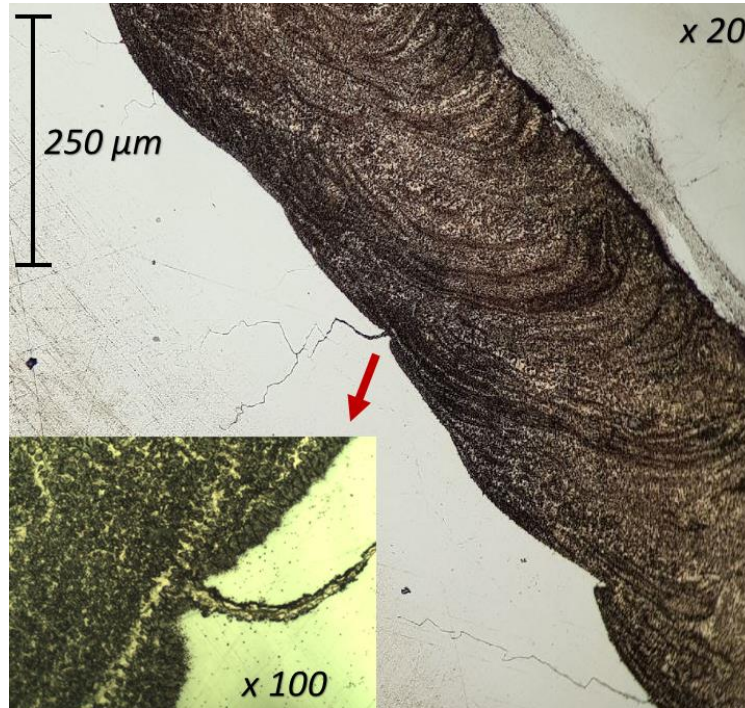


**Figure 7** – Crack formation on a border of SS and aluminium bronze. The dark structure – aluminium bronze, the light structure – SS.

### 3.3 Alternating SS 316L and Bronze Layers

The experimental samples series №2 grown from the same materials on the same operation conditions had no cracks at all. The scheme of the multimaterial deposition is shown in Figure 8a; the resulting microstructure with alternating layers of SS 316L and aluminum bronze optical micrograph is demonstrated in Figure 8b. All images of the microstructure demonstrate the absence of cracking or visible porosity in the whole volume of the specimen. We also observed the interpenetration of steel and bronze between nearby layers in the case of steel-on-bronze deposition, but the bronze-on-steel gives us a sharp and clear interface, as it is seen in Figure 6b. It is the result of higher rigidity and hardness

of steel as well as better miscibility of steel in the melt bath of bronze compared to the miscibility of bronze in the melt bath of steel. The penetration of steel into bronze improves microhardness of bronze layers [215] and its other mechanical characteristics but the intrusion of bronze into steel lowers mechanical properties of the steel layers.

The aluminum bronze forms a cross-linked morphology, which is seen in the  $\times 100$  magnified image. The angle deformations associated with inequal overheating were observed in the edge areas of the specimen (Figure 9). As in Figure 8, the dark layers correspond to bronze, and the light layers correspond to steel in Figure 9.

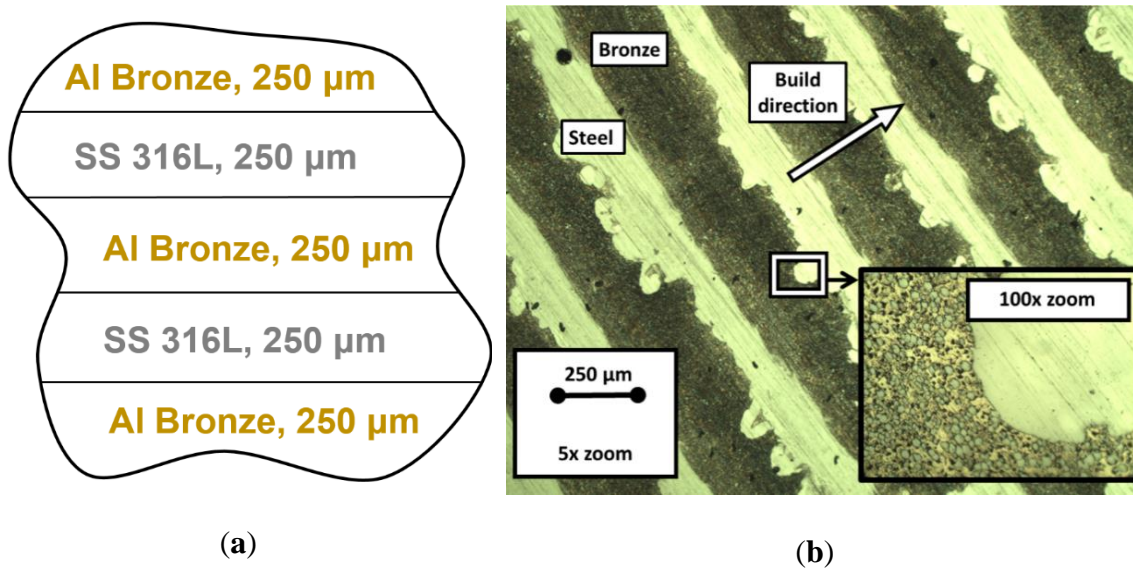


**Figure 8** – The laser deposition scheme (a) and the resulting gradient structure (b).

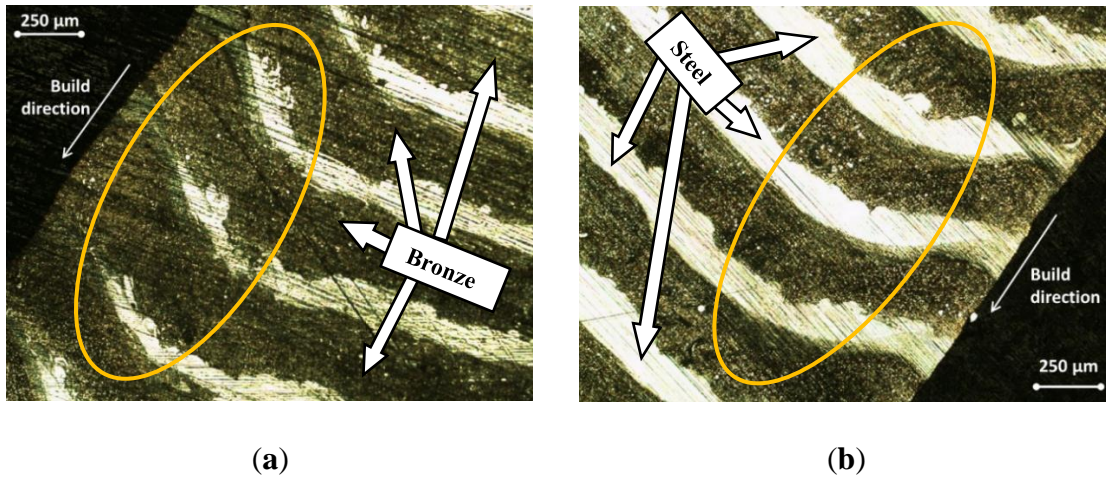


**Figure 9** – Edge effects in the gradient specimens (a,b) (marked by ellipses).

One of the reasons which caused this flawless fabrication was presumably a different thermal history in previous layers of samples series №1 and series №2 associated with differences between thermophysical characteristics of stainless steel and aluminium bronze. The huge number of layers of steel under the single layer of bronze (samples series №1) caused another sort of heat affection on the following layers comparing with structure with «sandwiched layers» (samples series №2).

### 3.4 Fabrication of SS 316L – Bronze FGMs Using the Gradient Path Method

The gradient path method can be realized with the gradual increase of one component amount and decrease of that of another component. This method is strongly effective in the case of DED-fabricated Fe-Cu FGMs and other kinds of FGMs, which consist of initial components with very different physical characteristics. Percentage of the first component of the gradient alloy changes gradually or sharply changes from 100% to 0% while the percentage of the second component increases from 0% to 100%. Gradient transition may include change of chemical composition, microstructure type, physical

properties, etc. Figure 10 schematically demonstrates the gradient transition from the pure material A to the pure material B directly (top picture) and through the intermediate section of the third material C (bottom picture). In the current research, the gradient path method also didn't demonstrate cracking in the specimens, as well as alternating layers' technique.

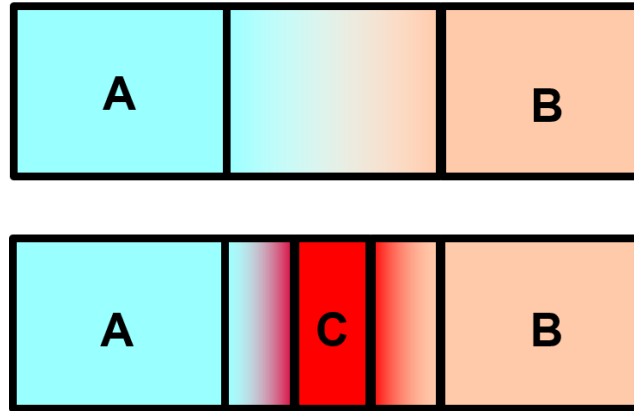


**Figure 10** – Schemes of the gradient path approaches.

### 3.5 Discussion

Difference between thermal expansion coefficients of materials along with rapid intermetallic growth, increase of microhardness, increase of elasticity modulus, and local embrittlement of the FG laser-deposited parts with two sharp transitions created from stainless steel AISI 316L and aluminium bronze in a DMT mode [119] via the direct joining scheme [120] lead to cracking on a border between SS and aluminium bronze. Two other strategies (alternating layers' technique and gradient path method) provided significantly better quality of bonding without observable defects. Porosity of such multilayer structures had an acceptable size and didn't influence on the resulting quality. Presumably, cracking in these structures was entirely excluded because of reassignment of internal stresses and deformations in volume of a part.

### **3.6 Interim Conclusion**

The effects of cracking in Fe-Cu FGMs can be suppressed by producing alternating layers' structures or using the gradient path method instead of direct joining under the same operation conditions. This approach leads to a comparatively favorable thermal history during the laser treatment process and provides an acceptable quality for the resulting part. The microstructure and physical characteristics of such parts are studied below.

## Chapter 4. Microstructural Characteristics of SS 316L – Bronze FGMs

### 4.1 Materials, Methods, and Design of the Experiment

The next experiment was aimed at the more detailed study of microstructural characteristics of the DED-fabricated quasi-homogeneous alloys and sandwich structures of the Fe-Cu system. They were the object of interest because they could be implemented both by themselves and as transitional zones in FGMs [68,121-125] including the Fe-Cu system. All these structures were fabricated using deposition strategies tested in the previous chapter. Three common types of the structures were investigated:

- The first type — 50 wt.% SS 316L + 50 wt.% bronze;
- The second type — 25 wt.% SS 316L + 75 wt.% bronze;
- The third type — a multilayer gradient steel-bronze structure.

Simultaneous powder feed fabricated the 1<sup>st</sup> and the 2<sup>nd</sup> types. Alternated 250- $\mu$ m-width layers created the 3<sup>rd</sup> type.

The experimental specimens were built on a base of four materials, which were prospective for the fabrication of Fe-Cu FGMs [125]:

- SS 316L–5520 (fraction 50–150  $\mu$ m) manufactured by Höganäs Belgium SA;
- Aluminum bronze (was already discussed before) similar to UNS C61800 (fraction 45–125  $\mu$ m), manufactured by Polema JSC (Tula, Russia);
- Tin bronze similar to the copper-tin alloy CuSn10-B/CB480K, (fraction 100–140  $\mu$ m) manufactured by Polema JSC (Tula, Russia);
- Chromium bronze similar to UNS C18400 chromium copper, (fraction 63–125  $\mu$ m) manufactured by Polema JSC (Tula, Russia).

Table 5 presents the chemical compositions of Sn and Cr bronzes. The chemical composition of Al bronze was presented earlier in Table 3. The composition of SS 316L can be found in [118].

**Table 5** – Chemical compositions of bronzes (wt.%).

<b>Element</b>	<b>Sn Bronze</b>	<b>Cr Bronze</b>
Cu	Base	Base
Al	0.05	–
Cr	–	0.76
Fe	0.10	0.05
Ni	0.10	0.05
O <sub>2</sub>	–	0.05
P	–	0.02
Pb	0.05	–
S	–	0.01
Sb	0.05	–
Si	0.05	–
Sn	9.96	–
Zn	0.11	–

Therefore, 8 groups of parts were fabricated in total (group 9 – the alloy of alternating layers of tin bronze and SS 316L – was excluded from consideration because it showed poor laser manufacturability and did not obtain an appropriate shape during the fabrication because of low heat consumption and poor adhesion of Sn bronze and steel). The study [125] approved this methodology and tested this set of groups (Table 6). The same types of alloys were discussed in the thesis [173]. It discussed the applicability of these alloys as transitional zones of Fe-Cu FGMs fabricated via the gradient path method and the alternating layers' technique [125].

**Table 6** – Set of groups<sup>1</sup> [125].

<b>Group №</b>	<b>1</b>	<b>2</b>	<b>3</b>	<b>4</b>	<b>5</b>	<b>6</b>	<b>7</b>	<b>8</b>
Description	C61800+SS (50/50 wt.%)	C18400+SS (50/50 wt.%)	CB480K+SS (50/50 wt.%)	C61800+SS (75/25 wt.%)	C18400+SS (75/25 wt.%)	CB480K+SS (75/25 wt.%)	C61800+SS (alt.)	C18400+SS (alt.)

<sup>1</sup> Abbreviation «alt.» referred to sandwich structures with alternating layers of steel and bronze.

The specific fabrication conditions of the specimens could be found in §3.1 of this study and in [125]. The microstructure analysis was performed using optical microscopes Altami MET 1C (OOO Altami, Saint Petersburg, Russia) and Axio Scope.A1 (Carl Zeiss GmbH, Germany). The specimens were treated with the etching (50 ml HCl + 50 ml C<sub>2</sub>H<sub>5</sub>OH + 2.5 g CuCl<sub>2</sub> during time ~8–10 s) concerning E340-13 [128] and E2014-17 [129]. SEM was conducted using the Quattro SEM microscope (Thermo Fisher Scientific, Netherlands) accordingly to ASTM E766-14(2019) [130] and E2014-17 [129]. The Bruker maXis impact mass spectrometer (Bruker Corporation, Billerica, MA, USA) was used for EDX microelement analysis concerning ASTM E1508-12a(2019) [131] and E2014-17 [129]. The XRD data were received on the Rigaku Ultima IV X-ray diffractometer (Rigaku Corporation, Tokyo, Japan). The Match! software ver. 3.13 build 220 (CRYSTAL IMPACT, Bonn, Germany) analysed the XRD raw data.

#### **4.2 Specificities of Microstructure Formation in SS 316L – Bronze FGMs**

The main goal of this thesis is making a scientific basis for the study of gradient structures that includes both Fe-based and Cu-based zones. Their mutual behavior and characteristics of the resulting alloy is a significant object of interest. It was also seen from the results of chapter 3 that implementation of alternating transitions between layers of steel and bronzes makes the material to be flawless even if the same treatment conditions lead to cracking in the case of direct joining. Therefore, the microstructure of alloys made from alternating layers of aluminium bronze and steel is needed to be discussed specifically. The results of SEM of specimens of group 7 proved the presence of the dendritic structure. These results are shown in Figure 11; the inserts demonstrate the single

dendrites. The dark areas in Figure 11 are related to the Fe-Cr-based regions; light areas are related to the Cu-based regions (see the results of the EDX analysis in Figure 12; the other elements, such as C, Al and Ni, were distributed almost regularly within the entire area of scanning). The significant inequality of the Fe-Cr-based structural elements size is seen in the SEM images. Different regions of the specimen demonstrated different microstructures: Fe-based elements have spherical and quasispherical shapes in one region and columnar and dendritic forms in the other. The ultra-high disproportional dendritic-shape crystal is observed in the right-bottom area of the image (Figure 11). The average width of its primary element was approximately equal to 18  $\mu\text{m}$ .

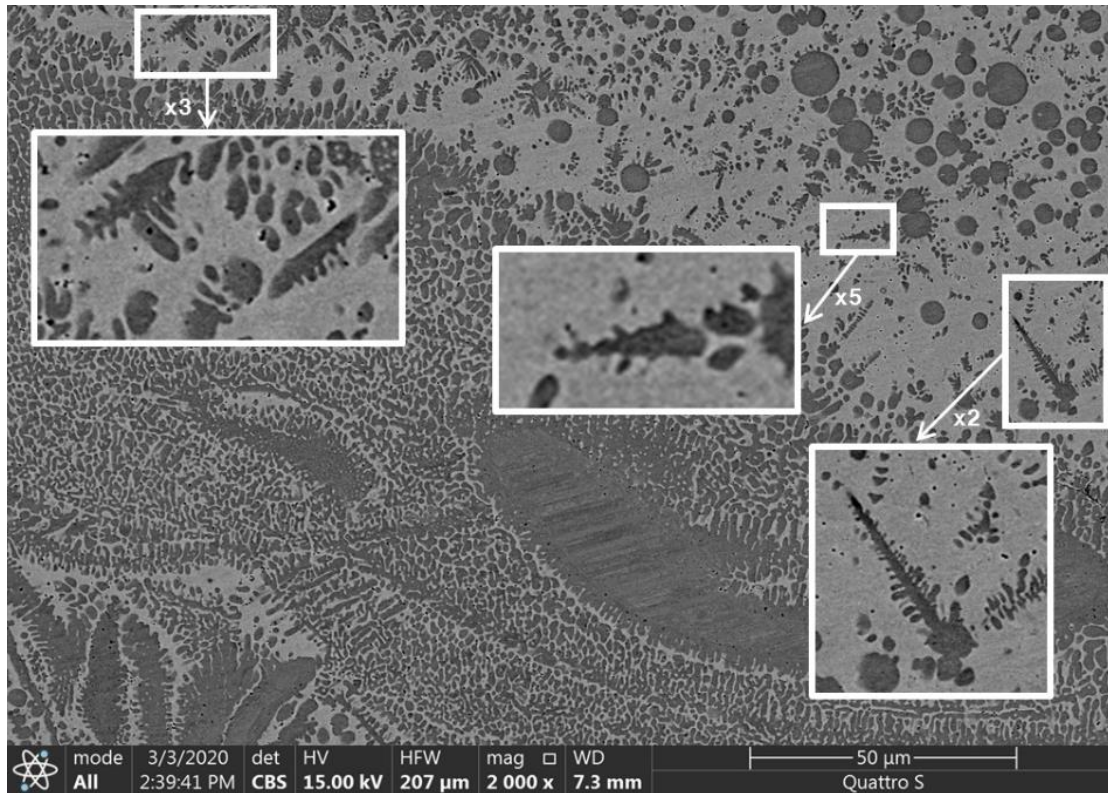


**Figure 11.** The dendritic structure of the FG specimen of group 7.

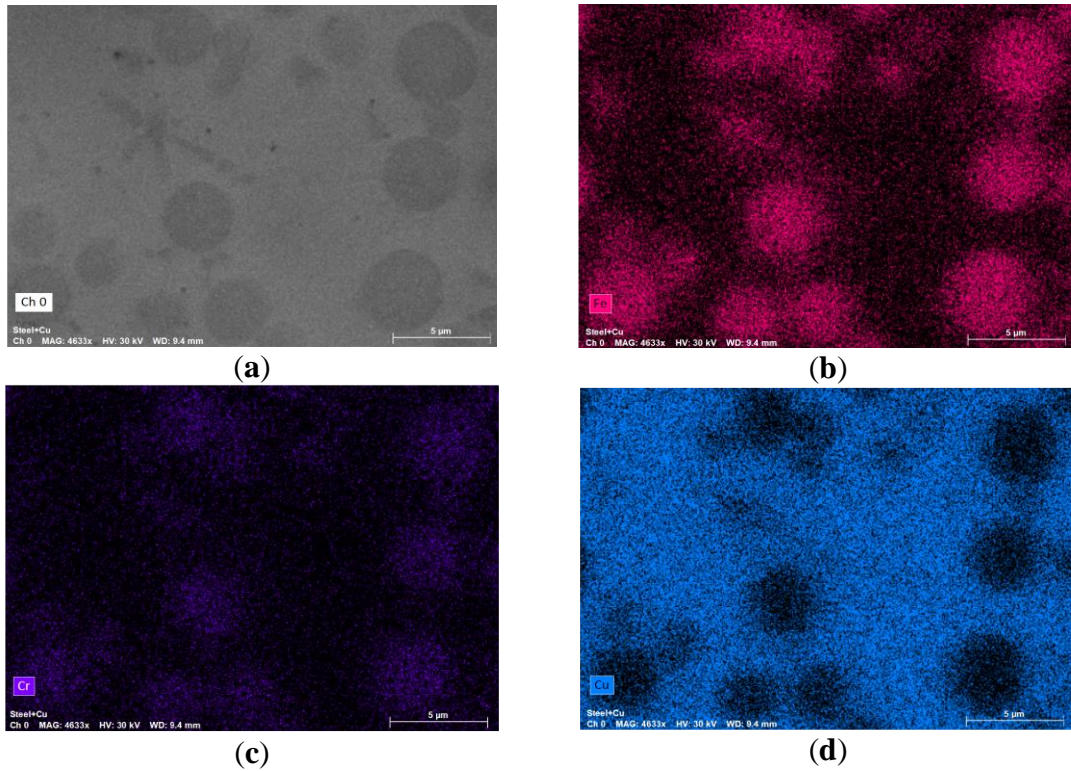


**Figure 12** – The results of the EDX analysis of group 7 ((a) – the base image, (b) – the Fe-based regions, (c) – the Cr-based regions, (d) – the Cu-based regions).

In Figure 13, other SEM images of fabricated specimens are demonstrated. Figure 13a shows the SEM image of the aluminum bronze C61800 and SS (50/50 wt.%) binary material (group 1). SEM micrographs with higher magnification taken from the central areas of group 1 specimens are shown in Figures 13b and 13c. Other images are related to specimens of group 7.

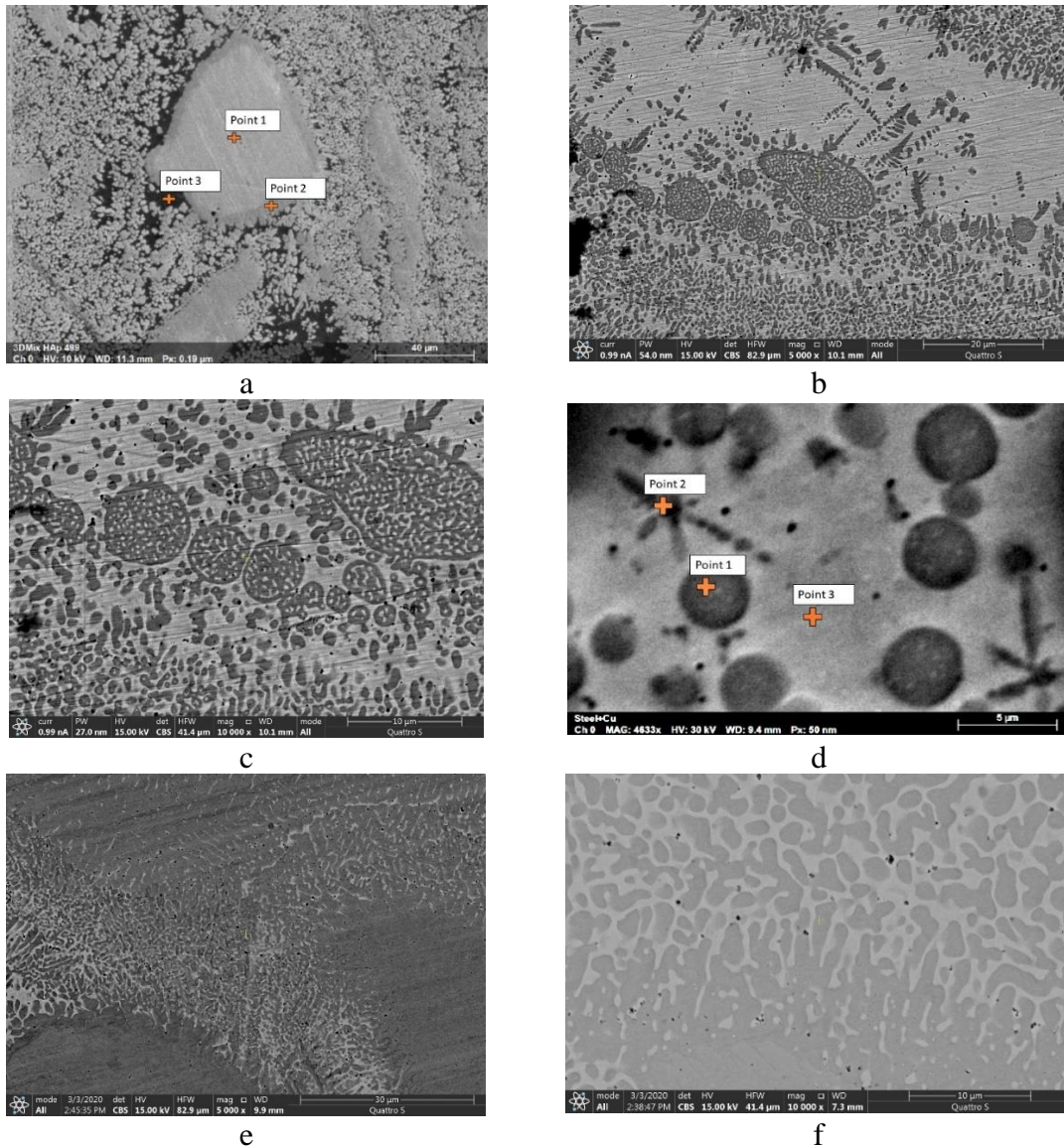


**Figure 13** – SEM micrographs of fabricated specimens. a-c: C61800+SS (50/50 wt.); d-f: C61800+SS (alt.).

### 4.3 Phase and Elemental Composition of SS 316L – Bronze FGMs

Three points were selected for the EDX microanalysis of group 1 (Figure 13a): in the middle zone, a Fe-based island expected (point 1), at its border from a side of the island (point 2), and at the border from the opposite side (point 3).

The EDX microanalysis of the specimen of group 7 was conducted at three points also (Figure 13d): inside the dark cell (point 1), inside the dendritic-shaped element (point 2), and inside the light matrix (point 3). The elemental concentrations in points 1-3 of Figure 13a are presented in 2-4 rows of Table 7; in points 1-3 of Figure 13d – in 6-8 rows. Figure 14 demonstrates the results of XRD analysis of group 7.

**Table 7** – Elemental concentrations in points 1-3 of SEM micrographs (Figure 13a,d).

Row №	Group 1 (UNS C61800+SS 316L (50/50 wt.%) – Figure 13a						
1	Point	Fe, at.%	Cr, at.%	Ni, at.%	Mo, at.%	Cu, at.%	Al, at.%
2	1	67.69	17.56	13.27	1.09	0.21	0.07
3	2	62.79	17.41	6.21	1.33	8.02	4.24
4	3	2.98	0.45	2.23	0.05	82.37	11.92
5	Group 7 (UNS C61800+SS 316L (alt.) – Figure 13d						
6	1	56.92	15.55	3.16	–	15.15	9.22
7	2	21.50	5.01	3.79	–	55.05	14.65
8	3	4.78	0.84	2.68	–	78.69	13.01

A qualitative XRD pattern analysis of group 7 revealed the existence of  $\gamma$ -Fe (unit cell  $a \cong 3.65 \text{ \AA}$  [132]) and  $\alpha$ -Cr ( $a \cong 2.88 \text{ \AA}$  [133]) phases (from now on unit cells were determined using Match! [134] ver. 3.13 build 220). The analysis was conducted on the assumption of a possible existence of Fe, Cu, Cr, Mo, Mn, and Al in the alloy conferring to the initial powder chemical compositions ([118]) and a possible presence of oxygen. This group is not a Cr-bronze-based group but Cr exists in the phase composition of SS 316L. The matching phases demonstrated in Figure 14 (red and green peaks) point at the absence of a  $\delta$ -Fe phase ( $a \cong 2.86 \text{ \AA}$ ) in the group 7 specimens. The formation of  $\gamma$ -Fe in a low-temperature area was typical for the binary Fe-Cu system consistent with its phase diagram [7,135-139] but was not observed in a Fe-Cr system [140,141]. But we see that only  $\gamma$ -Fe and  $\alpha$ -Cr are presented in the diffractogram. Therefore, some kind of third phase had to exist in the alloy except of  $\gamma$ -Fe and  $\alpha$ -Cr. It could be:

- $\epsilon$ -Cu, which could be responsible for the existence for a  $\gamma$ -Fe instead of  $\alpha$ -Fe after solidification in this ternary system. The results of the EDX microanalysis proved the presence of copper in Fe-Cr-based areas of the group 7 deposits (see Table 7).
- Al: its existence was also proved by EDX microanalysis. We observed {FCC austenitic  $\gamma$ -Fe}  $\rightarrow$  {BCC ferrite  $\alpha$ -Fe} phase transformation in DED-fabricated Fe-Cu alloys when deposited SS and C61800 simultaneously. This effect appears only in the presence of Al. The deposition of chromium bronze or tin bronze with SS didn't produce such a result.
- $\text{Cu}_3\text{Al}$ , which is based on the composition of two above-mentioned elements. It may be found here because of discussed { $\gamma$ -Fe}  $\rightarrow$  { $\alpha$ -Fe} phase transition, both existence of Cu and Al in the Fe-Cr-based zones, which was proved by EDX, and the needle-type microstructure of these areas.

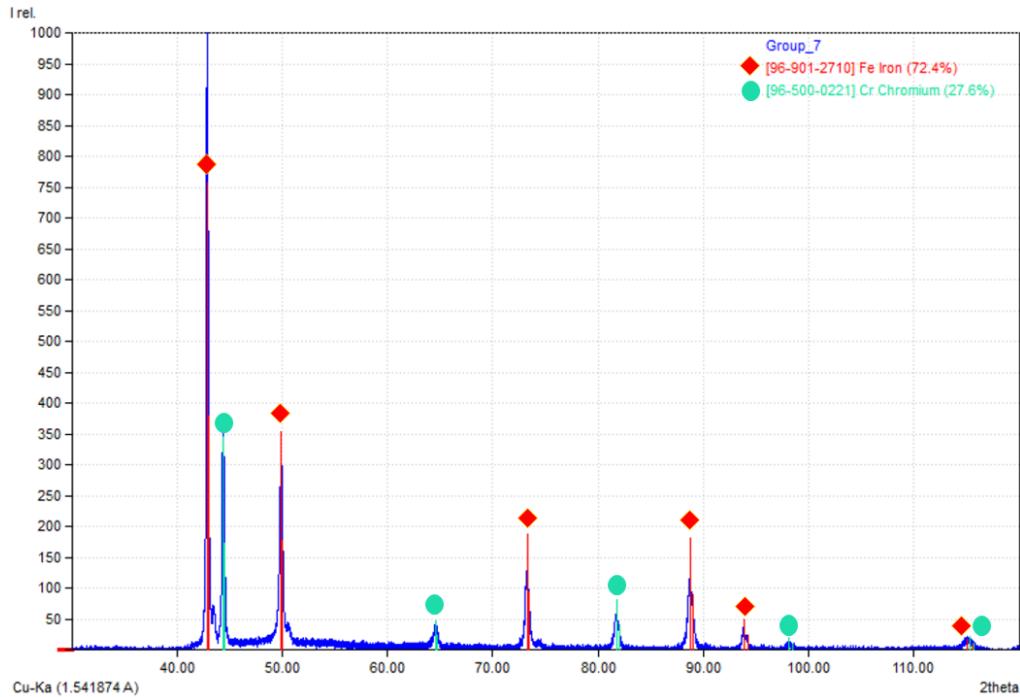


**Figure 14** – XRD pattern data of group 7. 1<sup>st</sup>, 3<sup>rd</sup>, 5<sup>th</sup>, 7<sup>th</sup>, 8<sup>th</sup>, and 10<sup>th</sup> peaks correspond to the  $\gamma$ -Fe phase; 2<sup>nd</sup>, 4<sup>th</sup>, 6<sup>th</sup>, 9<sup>th</sup>, and 10<sup>th</sup> – to  $\alpha$ -Cr

#### 4.4 Crystallization Rate and Dendritic Structure of SS 316L – Bronze FGMs

The existence of the dendritic structure revealed in SS-bronze specimens pointed at necessity of the more detailed study of the microstructure formation characteristics. It is known [142,143] that there is a dependence in different binary metal systems between the structure type (dendritic, cellular–dendritic or cellular), the solutal undercooling criteria  $\sqrt{v_{cryst}}/G$  and the admixture concentration  $C_0$  (Figure 15) [142,143].

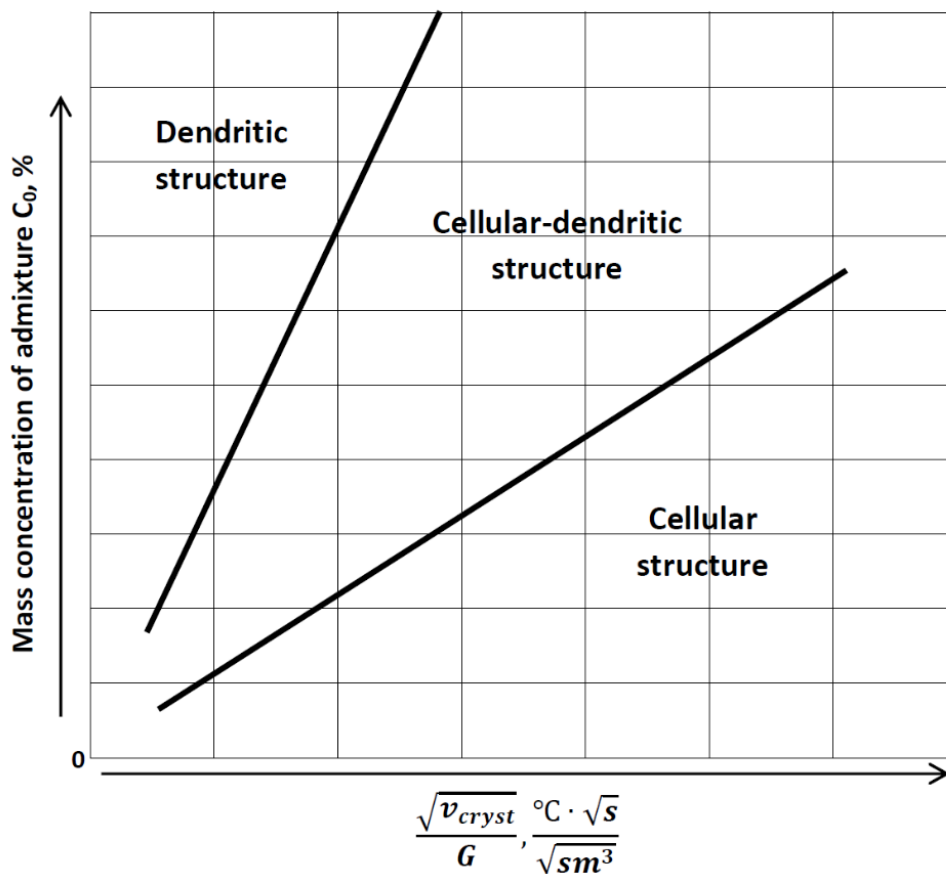


**Figure 15** – The alloy structure type dependence on the solutal undercooling criteria and the admixture concentration [142,143].

In Figure 15,  $v_{cryst}$  is the crystallization rate and  $G = \partial T/\partial n$  is the temperature gradient [142] ( $n$  is the distance from the phase interface to the considered point towards

normal direction). Figure 15 demonstrates the dependencies between the growth of the admixture amount and forming of the dendritic structure within the definite range of the solutal undercooling criteria. This dependence can be experimentally tested for binary system laser-deposited alloys such as Fe-Cu FGMs in three steps. The first step is an analytical estimation of the crystallization rate function, the second step is a determination of the temperature gradient in the volume of the workpiece, and the third one is devoted to the admixture mass concentration evaluation. The current study reports the results acquired in the first step, and further investigation in this field is going to answer other two questions.

#### *4.4.1 Evaluation*

The dendritic structure, which occurred during the crystallization process of the FGM of group 7, in our case was observed mainly in the central part of the slab. It was an area where the temperature gradient near the crystallization front had its minimal value, which is in good accordance with the theory [142]. It is known that the most common occurrence of dendrites is a shrinkage porosity [142]. In our case, all specimens were replete with sub-microscale pores (size of a single pore was less than 500 nm) (Figure 16), and the areas with the highest porosity consisted of the highest number of dendrites.

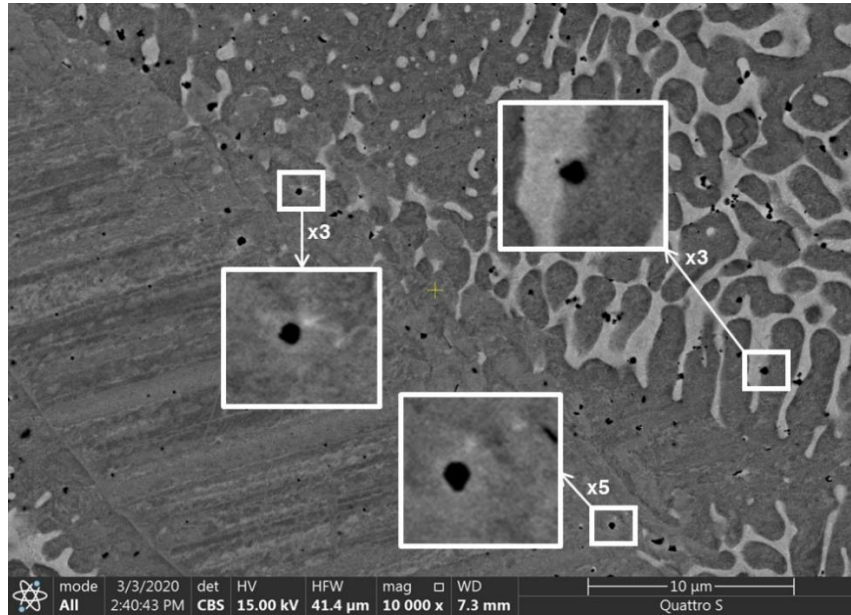


**Figure 16** – The sub-microscale porosity of the specimen.

The dendritic and spherical cellular structure is also seen in the micrograph in Figure 17. The interesting phenomenon here is an inner curvature inside the Cu-based region (a large light area in the middle of the image) that demonstrates a solidified turbulent whirlwind-like flow of the liquid alloy.

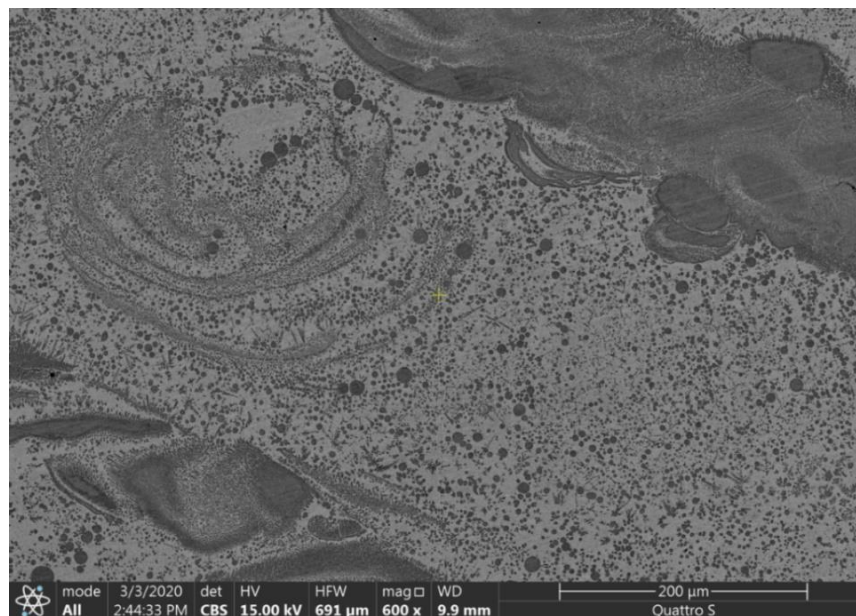


**Figure 17** – The SEM micrograph of the Fe-Cu FGM.

The size of the single dendrite secondary elements was estimated using the results of SEM (Figure 18). The black areas here consist from steel as it was shown by the results of EDX (some of them are demonstrated in Figure 12).

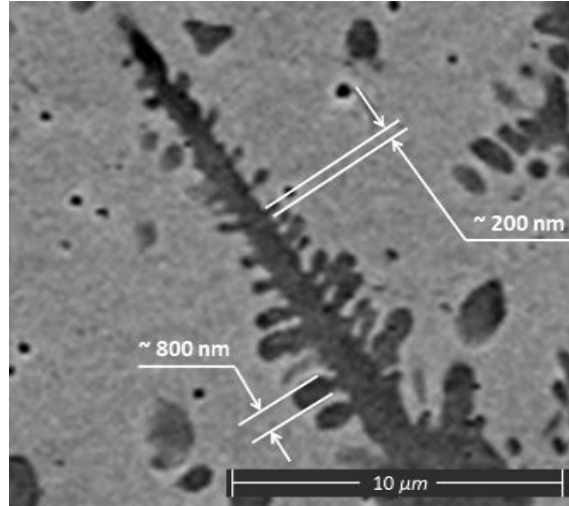


**Figure 18** – The evaluation of the secondary elements of the dendrites sketch.

Let us write Equations (12) and (13) in the dimensionless coordinates  $K_y = y/P$ ,  
 $K_z = z/H$ :

$$\frac{\partial f(y, z)}{\partial y} = - \frac{K_y}{K_{PL} \cdot \sqrt{1 - K_y^2 - K_z^2}}, \quad (15)$$

$$\frac{\partial f(y, z)}{\partial z} = - \frac{K_z}{K_{HL} \cdot \sqrt{1 - K_y^2 - K_z^2}}, \quad (16)$$

where  $K_{PL} = L/P$  and  $K_{HL} = L/H$  are the dimensionless form factors. Here,  $P$  is the half-width of a single track, and  $H$  is the depth of the laser influence (the depth of the HAZ).

$P$  equals:

$$P = \frac{800}{2} = 400 \mu\text{m} = 4 \cdot 10^{-4} \text{ m}. \quad (17)$$

The depth of the HAZ  $H$  can be estimated by equation (18) from [146,147]:

$$H \cong 2 \cdot \sqrt{\frac{a \cdot \tau_p}{\pi}} - \frac{T_{melt} \cdot \lambda}{q}, \quad (18)$$

where  $\tau_p$  is the duration of the laser treatment (under the condition  $\tau_p \leq \tau_{max}$ , where  $\tau_{max} = d_f^w / (2 \cdot a)$  and  $d_f^w$  is the laser beam diameter on the surface of the workpiece [24]), and  $q$  is the laser power density on the surface of the workpiece. In our conditions, the average laser power  $Q_{AB} = 500$  W for aluminum bronze, and  $Q_{SS} = 308$  W for stainless steel. The average laser power for our calculations is assumed equal to

$$Q = \sqrt{Q_{AB} \cdot Q_{SS}} \cong 392 \text{ W}. \quad (19)$$

In our experiments, the approximate diameter of the spot on the surface of the workpiece was estimated as  $d_f^w = 500$   $\mu\text{m}$  (Figure 19), so the average laser power density on the surface of the workpiece is

$$q = \frac{4 \cdot Q}{\pi \cdot (d_f^w)^2} \cong 2.00 \cdot 10^9 \text{ W/m}^2. \quad (20)$$

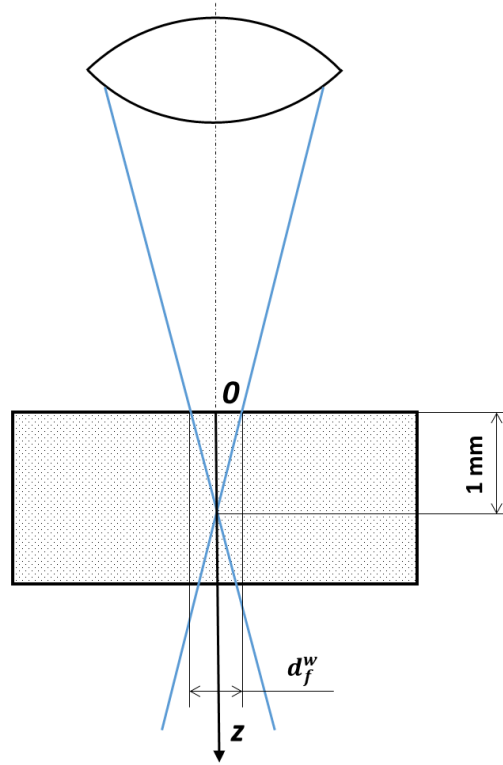


**Figure 19** – The laser source focusing scheme.

Near the melting points, with the atmosphere pressure, the thermal diffusivity of SS 316L is approximately  $a_{SS} \cong 3.5 \cdot 10^{-6} \text{ m}^2/\text{s}$  [56], of aluminium bronze  $a_{AB} \cong 1.5 \times 10^{-4} \text{ m}^2/\text{s}$  [57], and of air  $a_{air} \cong 3.6 \cdot 10^{-4} \text{ m}^2/\text{s}$  [58]. Since the experiments were performed with a binary alloy of both metals with a small amount of porosity, the generalized thermal diffusivity factor was estimated for a first approximation as

$$a = a_{air} \cdot \frac{V_{air}}{V_{\Sigma}} + a_{AB} \cdot \frac{V_{AB}}{V_{\Sigma}} + a_{SS} \cdot \frac{V_{SS}}{V_{\Sigma}} \cong 7.7 \cdot 10^{-5} \text{ m}^2/\text{s} \quad (21)$$

Here, approximately, the volume of air was estimated as 0.1%, of bronze 49.95% and of steel 49.95% of the whole slab.

The same calculation should be provided with a thermal conductivity coefficient:  $\lambda_{SS} \cong 35.1 \text{ W}/(\text{m} \times \text{K})$  [56],  $\lambda_{AB} \cong 75.0 \text{ W}/(\text{m} \times \text{K})$  [59],  $\lambda_{air} \cong 0.1 \text{ W}/(\text{m} \times \text{K})$  [58]:

$$\lambda = \lambda_{air} \cdot \frac{V_{air}}{V_{\Sigma}} + \lambda_{AB} \cdot \frac{V_{AB}}{V_{\Sigma}} + \lambda_{SS} \cdot \frac{V_{SS}}{V_{\Sigma}} \cong 55.0 \text{ W}/(\text{m} \cdot \text{K}). \quad (22)$$

The melting points of our metals are approximately equal to:  $T_{melt}^{SS} \cong 1420 \text{ }^{\circ}\text{C}$  and  $T_{melt}^{AB} \cong 1070 \text{ }^{\circ}\text{C}$ ; the metal with the lower melting point decreases the melting point of the whole alloy [143]; and the reason for the drift of the melting point of the binary alloy is the distribution of the admixtures between liquid and solid phases. Therefore, for a first approximation, the melting point of our binary alloy can be considered as

$$T_{melt} = \frac{T_{melt}^{SS} + T_{melt}^{AB}}{2} \cong 1245 \text{ }^{\circ}\text{C} = 1518.15 \text{ K}. \quad (23)$$

In our case, the laser pulse duration was set as

$$\tau_p = 0.001 \cdot \tau_p^{max} = \frac{d_f^w}{2000 \cdot a} = 1.79 \cdot 10^{-3} \text{ s}. \quad (24)$$

Therefore, from (18)

$$H \cong 8.83 \cdot 10^{-5} \text{ m}. \quad (25)$$

So

$$K_y = \frac{y}{p} = 2500 \cdot y \left[ \frac{1}{\text{m}} \right], \quad (26)$$

$$K_z = \frac{z}{H} \cong 11325 \cdot z \left[ \frac{1}{\text{m}} \right]. \quad (27)$$

Assuming (11), (15) and (16),

$$\cos\alpha = \frac{1}{\sqrt{1 + \frac{\left(\frac{K_y}{K_{PL}}\right)^2 + \left(\frac{K_z}{K_{HL}}\right)^2}{1 - K_y^2 - K_z^2}}}. \quad (28)$$

Let us add new dimensionless form factor  $K_{LP}$  and consider the dimensions of the real melt bath  $l$ ,  $2 \cdot p$ , and  $h$  (length, width, and depth respectively), the dimensionless factor  $B = H/h$ , and dimensionless adjusting factors  $m$ ,  $n$ , and  $j$ , which describe the difference between the real melt bath and the analytical one:

$$K_{LP}^2 = \frac{1}{K_{PL}^2} = \frac{L^2}{p^2} = \frac{l^2 \cdot B^2}{2 \cdot B - 1} = \frac{l^2}{p^2} = \frac{(e-1)^2}{8 \cdot \pi \cdot e} \cdot \frac{n^2}{m^2} \cdot \frac{q \cdot v_{DED}}{a \cdot \lambda \cdot T_{melt}} =$$

$$= 0.043217 \cdot \frac{n^2}{m^2} \cdot \frac{q \cdot v_{DED}}{a \cdot \lambda \cdot T_{melt}}$$
(29)

and paste

$$\frac{1}{K_{HL}^2} = \frac{1}{K_{PL}^2} \cdot \frac{j^2}{n^2 \cdot (2 \cdot B - 1)}$$
(30)

into (22), the dependence of the crystallization rate from the deposition conditions with a fast-moving concentrated source will be found in the case of the ellipsoid crystallization front:

$$v_{cryst} = v_{DED} \cdot \cos \alpha = \frac{v_{DED}}{\sqrt{1 + 0.043217 \cdot \frac{q \cdot v_{DED}}{a \cdot \lambda \cdot T_{melt} \cdot m^2} \cdot \frac{n^2 \cdot K_y^2 + \frac{j^2}{2 \cdot B - 1} \cdot K_z^2}{1 - K_y^2 - K_z^2}}}$$
(31)

If the crystallization front is described as a full ellipsoid, then  $B = 1$ , and  $m = n = j = 1$  [142]. In this light,

$$v_{cryst}(y, z) = v_{DED} \cdot \cos \alpha \cong \frac{v_{DED}}{\sqrt{1 + 0.00672 \cdot q \cdot v_{DED} \cdot \frac{K_y^2 + K_z^2}{1 - K_y^2 - K_z^2}}};$$
(32)

$$\begin{aligned}
v_{cryst}(y, z) &\cong \\
&\cong \frac{0.014}{\sqrt{1 + 0.00672 \cdot 2 \cdot 10^9 \cdot 0.014 \cdot \frac{(6.25 \cdot y^2 + 128 \cdot z^2) \cdot 10^6}{1 - (6.25 \cdot y^2 + 128 \cdot z^2) \cdot 10^6}}} \cong \\
&\cong \frac{0.014}{\sqrt{1 + \frac{1.9 \cdot 10^{11} \cdot (6.25 \cdot y^2 + 128 \cdot z^2)}{1 - (6.25 \cdot y^2 + 128 \cdot z^2) \cdot 10^6}}}.
\end{aligned} \tag{33}$$

Now, the value of  $v_{cryst}$  in any point  $(y, z)$  that belongs to the ellipse segment can be estimated:

$$\begin{cases} \left(\frac{y}{P}\right)^2 + \left(\frac{z}{H}\right)^2 \leq 1, \\ 0 \leq z \leq H, \end{cases} \tag{34}$$

among the research of the function behavior in the irregular points.

In the middle point (the center of a laser beam spot)  $y = 0, z = 0$ , the crystallization rate is equal to the laser scanning speed according to (33):

$$v_{cryst}(0,0) \cong \frac{0.014}{\sqrt{1 + \frac{0}{1}}} = 0.014 \text{ m/s} = v_{DED} \tag{35}$$

In general, this result could be achieved directly from (31): independently of concrete values of the process parameters, the crystallization rate in point  $(0,0)$  is equal to the scanning speed of the source.

**Proposition 1.** Using (33) (in particular) or (31) (in general), the proposition about the crystallization rate in the crystallization front can be proved:

$$\lim_{z \rightarrow H} v_{cryst}(0, z) = \lim_{y \rightarrow P} v_{cryst}(y, 0) = 0. \tag{36}$$

**Proof of Proposition 1.** Firstly, in our case, in the border point  $y = 0, z = H = 8.83 \cdot 10^{-5}$ , from (33)

$$v_{cryst}(0, H) \cong \frac{0.014}{\sqrt{1 + \frac{1.9 \cdot 10^{11} \cdot (0 + 128 \cdot 7.8 \cdot 10^{-9})}{1 - (0 + 128 \cdot 7.8 \cdot 10^{-9}) \cdot 10^6}}} \cong \frac{0.014}{\sqrt{1 + \frac{1.9 \cdot 10^5}{1 - 1}}} \cong \frac{\text{const}}{\sqrt{1 + \infty}}; \quad (37)$$

$$\lim_{z \rightarrow H} v_{cryst}(0, z) = \frac{1}{\sqrt{1 + \infty}} = \frac{1}{\sqrt{\infty}} = \frac{1}{\infty} = 0. \quad (38)$$

Secondly, in the other border point  $y = P = 4 \times 10^{-4}, z = 0$ , from (33)

$$v_{cryst}(P, 0) \cong \frac{0.014}{\sqrt{1 + \frac{1.9 \cdot 10^{11} \cdot (6.25 \cdot 1.6 \cdot 10^{-7} + 0)}{1 - (6.25 \cdot 1.6 \cdot 10^{-7} + 0) \cdot 10^6}}} \cong \frac{0.014}{\sqrt{1 + \frac{1.9 \cdot 10^5}{1 - 1}}} = \frac{\text{const}}{\sqrt{1 + \infty}}; \quad (39)$$

$$\lim_{y \rightarrow P} v_{cryst}(y, 0) = \frac{1}{\sqrt{1 + \infty}} = \frac{1}{\sqrt{\infty}} = \frac{1}{\infty} = 0 = \lim_{z \rightarrow H} v_{cryst}(0, z) \quad \square \quad (40)$$

The melting process stops by reaching the crystallization front, so the crystallization rate in these points becomes equal to zero in the limit, and this phenomenon does not depend on the concrete parameters of process, which can be easily proved using (31).

Figure 20 demonstrates the graph of the two-variable function  $v_{cryst}(y, z)$ . It is seen that the value  $v_{cryst} = v_{DED} = 0.014$  m/s, which was calculated above, is a maximal value of this function (and belongs to point (0,0)), and the crystallization rate steeply decreases with the distance from the center of the laser heat spot.

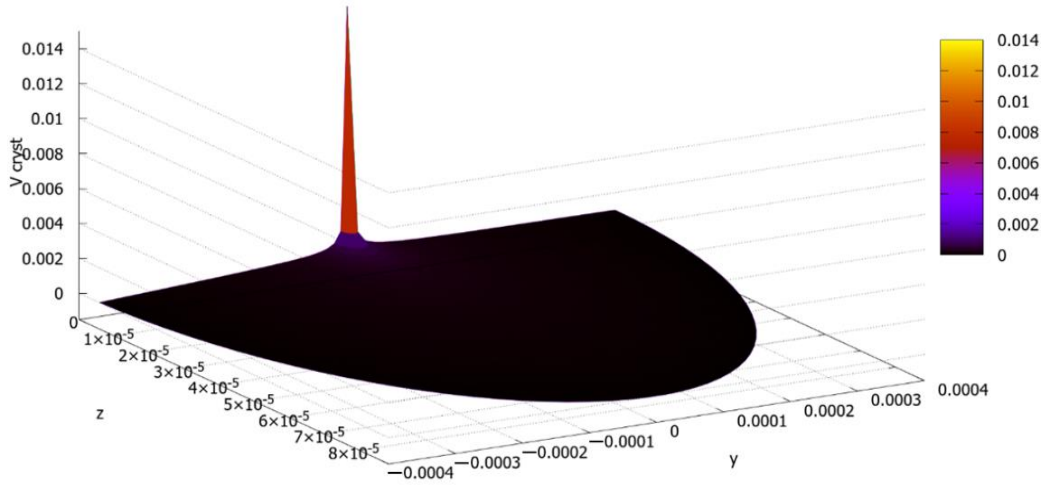


**Figure 20** – The crystallization rate function graph ( $[z] = m$ ,  $[y] = m$ ,  $[v_{cryst}] = m/s$ ).

Now, using the function  $v_{cryst}(y, z)$ , the width of the secondary elements of the dendrites function  $a(y, z)$  can be defined and the size  $a(y, z)$  in any point of the area (34) can be found:

$$\begin{aligned}
 a(y, z) &= \frac{2 \cdot D_l}{0.014} = \\
 &= \frac{D_l \cdot \sqrt{1 + \frac{1.9 \cdot 10^{11} \cdot (6.25 \cdot y^2 + 128 \cdot z^2)}{1 - (6.25 \cdot y^2 + 128 \cdot z^2) \cdot 10^6}}}{0.007}.
 \end{aligned} \tag{41}$$

For the Fe-Cu system, the diffusion coefficient was estimated in [148] as

$$D_l = 0.03 \cdot 10^{-4} \cdot e^{\frac{-187 \cdot 10^3}{R \cdot T}}. \tag{42}$$

In our case,  $T = T_{melt} = 1518.15$  K, and  $R = \text{const} \cong 8.315$  J/(mol·K). Therefore,

$$D_l = 0.03 \cdot 10^{-4} \cdot e^{\frac{-187 \cdot 10^3}{8.315 \cdot 1518.15}} \cong 1.12 \cdot 10^{-12} \text{ m}^2/\text{s}. \tag{43}$$

Firstly, it can be seen that the width of the secondary elements of the dendrites at the center of the laser source spot (0,0) depends only on the laser scanning speed  $v_{DED}$  (35) and the diffusion coefficient  $D_l$ :

$$a(0,0) = \frac{D_l \cdot \sqrt{1 + \frac{0}{1}}}{0.007} \cong 1.6 \cdot 10^{-10} \text{ m} \cong 0.2 \text{ nm} = \frac{2 \cdot D_l}{v_{cryst}(0,0)} = \frac{2 \cdot D_l}{v_{DED}}. \quad (44)$$

Therefore, from (41) and (43)

$$a(y,z) = 1.6 \cdot 10^{-10} \cdot \sqrt{1 + \frac{1.9 \cdot 10^{11} \cdot (6.25 \cdot y^2 + 128 \cdot z^2)}{1 - (6.25 \cdot y^2 + 128 \cdot z^2) \cdot 10^6}}. \quad (45)$$

The width of the secondary elements of the dendrites is in inverse proportion with the crystallization rate (7). While the crystallization rate decreases, the secondary elements become wider. In the border points  $(P,0)$  and  $(0,H)$ , where the crystallization rate reaches zero in limit (36), the width of the secondary elements of the dendrites function reaches the infinite value in limit

$$\lim_{y \rightarrow P} a(0,z) = \lim_{z \rightarrow H} a(y,0) = \frac{const}{0} = \infty. \quad (46)$$

Function (45) demonstrates that there are two approximate theoretical areas of the dendrites in our specimen. The first area (Figure 21) is the region of the nanoscale and quasi nanoscale ( $\sim 50$  nm) dendrites («small dendrites»). The minimum value of the function is reached at point (0,0) (as it was calculated above, it is equal to 0.2 nm). The second area is the region of the «huge dendrites», where the secondary elements of dendrites reach the submicronic size (approximately from  $10^{-7}$  to  $3 \times 10^{-7}$  m). Figure 22 demonstrates the function behavior for interval  $0 \leq a \leq 3.5 \times 10^{-7}$  m. It is seen from Figure

22 that there is a steep increase in  $a$  by getting closer to the crystallization front. It is evident that point  $a = a_{\max}$ , aligned with the hugest dendrites of the specimen, should exist.

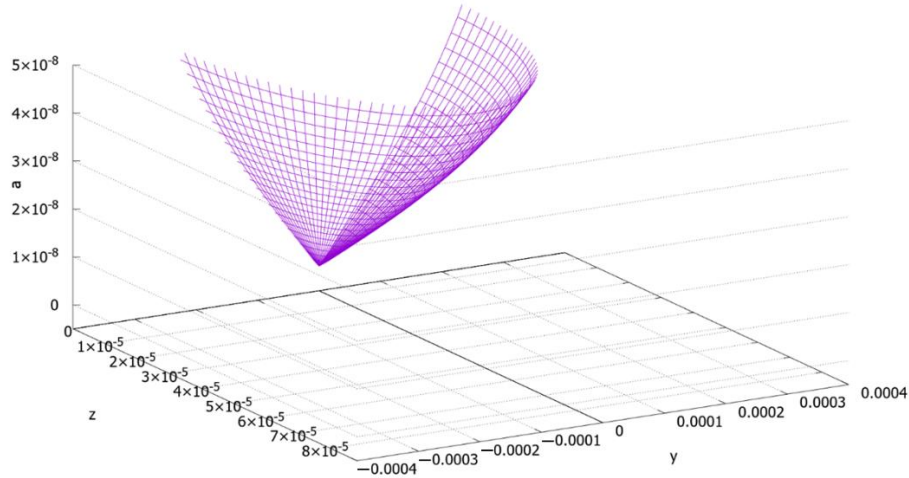


**Figure 21** – The area of the «small dendrites» ( $z$ ,  $y$ , and  $a$  are provided in meters).

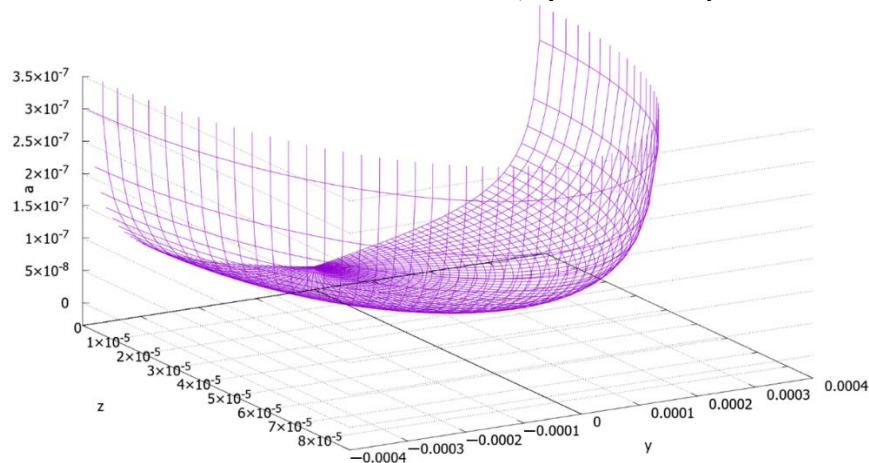


**Figure 22** – The width of the secondary elements of the dendrites function graph ( $z$ ,  $y$ , and  $a$  are provided in meters).

It can be seen from Figure 18 that the numerical results have a good accordance with the experimental data in the area of the «huge dendrites». The width of the secondary elements of the dendrites from Figure 18 was estimated as being from 200 to 800 nm (from  $2 \times 10^{-7}$  to  $8 \times 10^{-7}$  m).

In conclusion, it should be mentioned that there is a theoretical dependence between the width of a secondary element of a dendrite and the temperature gradient  $G = \partial T / \partial n$  [142]:

$$a = \frac{2\Delta T \cdot \operatorname{tg}\gamma}{G}, \quad (47)$$

where  $\gamma$  is the vertex angle of the element of the dendrite [149], and  $\Delta T$  is the crystallization interval of the alloy. Using equation (7), we can achieve the system (50) for  $\gamma$ :

$$\frac{2 \cdot D_l}{v_{cryst}} = \frac{2\Delta T \cdot \operatorname{tg}\gamma}{G}, \quad (48)$$

$$\operatorname{tg}\gamma = \frac{G \cdot D_l}{v_{cryst} \cdot \Delta T}, \quad (49)$$

$$\begin{cases} \gamma = \operatorname{arctg}\left(\frac{G \cdot D_l}{v_{cryst} \cdot \Delta T}\right), \\ -\frac{\pi}{2} < \gamma < \frac{\pi}{2}. \end{cases} \quad (50)$$

The estimation of the vertex angles of the dendrites growing in the Fe-Cu FGMs using (50) and comparison of the analytical values with the angles measured during experiments is a viable task for future research in this field.

#### 4.4.2 Summary

The dendritic structure analysis was performed in the case of the DED of an FGM created from aluminum bronze with 10% Al and 1% Fe content and SS 316L using the alternating layers' technique [118] (group 7). The microstructure was observed using optical and SEM methods, and the EDX analysis was performed. Using the fast-moving point source model with an ellipsoid crystallization front, two important crystallization parameters were analytically evaluated: the crystallization rate and the width of the secondary elements of the dendrites. The analytical dependence between vertex angles of

the dendrites, the crystallization rate, crystallization interval and temperature gradient were demonstrated. It was shown that in the case of a model of a fast-moving concentrated source with an ellipsoid crystallization front, the crystallization rate at the center point of the heat spot is equal to the laser scanning speed. The width of the secondary elements of the dendrites  $a$  at this point of the Fe-Cu laser-deposited FGM was evaluated using the model as 0.2 nm. The function  $a(y,z)$  demonstrated the existence of an area of «small dendrites» (with the width of the secondary elements from 0.2 to approximately 50 nm) and «huge dendrites» (approximately from 0.1 to 0.3  $\mu\text{m}$ ) (these results were calculated using the resulting equation). The theoretical width of the secondary elements of the «huge dendrites» was found to be in good accordance with the experimental data (it was estimated as being from 0.2 to 0.8  $\mu\text{m}$  using the SEM micrographs). Near the crystallization front, the crystallization rate tends to zero, and the width of the secondary elements of the dendrites tends to infinity, according to the results of the theoretical analysis. It was supposed that there were no dendrites in the FGM after the «critical point», whose coordinates  $(y_{\text{max}}, z_{\text{max}})$  could be also estimated by numerical methods. The results of this research can be applied in further investigations of the crystal structure of laser-deposited binary system FGMs, for improvement of the mathematical models and methods in this area of the crystallization process physics. The possibility to predict the geometrical parameters of the micro- and nanostructure at the single-crystal level allows varying the necessary physical and mechanical characteristics of the resulting gradient materials [150-155].

#### 4.5 Interim Conclusion

The observed types of microstructure of SS 316L – bronze laser-deposited alloys were mainly dendritic and cellular-dendritic. Deposition parameters (scanning speed, laser power) strongly influence the resulting microstructural characteristics of as-fabricated parts. For instance, the size of dendritic elements depends on the crystallization rate, and the crystallization rate itself depends on the scanning speed of the laser source.

Decreasing dimensions of dendritic elements such as their secondary elements are expected to lead to an improvement in the mechanical properties of FG alloys. {FCC austenitic  $\gamma$ -Fe}  $\rightarrow$  {BCC ferrite  $\alpha$ -Fe} phase transformation is the most important phase process in these materials in terms of possible influence on the physical and mechanical properties of the resulting parts. This effect was observed in the presence of Al in the case of the deposition of aluminium bronze and SS 316L.

Specific elements (Fe, Cu, Cr) were distributed unevenly in all cases, and intermixing in the gradient alloys was difficult due to the huge positive enthalpy of mixing. This issue can be reduced by using several specific techniques such as ultrasonic-assisted laser deposition (discussed later in the text of the current study) and oscillating laser DED.

The most common microstructural defects of Fe-Cu parts are porosity, gas pockets, hot and liquation cracking, which can be eliminated by the proper choice of the deposition strategy, material composition, and operation conditions. The observed porosity had a sub-microscale size with a characteristic dimension of a single pore lower than 500 nm. The fewer defects were observed in the parts deposited by the alternating layers strategy (varying 250- $\mu$ m-layers of the bronze and the steel).

## Chapter 5. Mechanical Properties of SS 316L – Bronze FGMs

The next goal of this study is the investigation of important mechanical properties of the resulting FGMs and their elements (quasi-homogeneous structures) and determining their correlation with microstructural characteristics of the alloys studied before.

### 5.1 Materials, Methods, and Design of Experiment

The materials and methods of making Fe-Cu structures were the same as it was discussed in Chapters 3 and 4. Specimens for tensile tests were prepared via electrical discharge machining using Mitsubishi-MV-1200R (Mitsubishi Electric Europe B.V., Ratingen, Germany). The resulting tensile test specimen shape was chosen according to [156-164]. Tensile tests were performed under the terms and conditions of ASTM E8/E8M-16a [116] at the rate of 2.7 mm/min using INSTRON 5969 dual column testing system and an INSTRON Bluehill® Universal materials testing software (Norwood, Massachusetts, United States), later the results were analyzed via Vic-3D DIC package (Correlated Solutions, Inc., Irmo, South Carolina, United States). The elasticity modulus values were obtained from angles between linear parts of the engineering stress-strain curves and the positive abscissa axis. The specific energy of the proportional strain was determined as a triangle area under the stress-strain curve in the region of the proportional strain. There were estimated the residual plastic part of the absolute strain  $\Delta L_{\text{plast}}$ , which persists in the specimen after its failure, the elastic part  $\Delta L_{\text{elastic}}$ , which disappears after the rupture, and their ratio  $\Delta L_{\text{plast}} / \Delta L_{\text{elastic}}$ , which indicates the stage of loading related to the failure of the specimen. UTS is considered to be the value of tensile stress corresponding to the maximum load. The macrofractography analysis was conducted in the same way as it was

done for microstructural characterization in Chapter 4. Microhardness tests and stiffness measurements were performed in automatic mode via the PB-1000 mechanical hardness tester (Nanovea, CA, United States) with a triangular Berkovich diamond pyramid as an indenter. An indentation force was equal to 3 N, the resulting values of microhardness were automatically recalculated in a Vickers's scale.

## 5.2 Results of Tensile Testing and Their Correlation with Microstructure of Materials

Based on the results of mechanical tests, the engineering stress-strain curves were obtained for all groups (see supplementary Figures S.1 – S.17). The elasticity modulus is seen in these curves as an angle between their linear parts and the positive abscissa axis. The squares of shaded triangle regions show the quantitative meaning of the specific energy of the proportional deformation (modulus of resilience).

The calculated mechanical characteristics of materials of all groups acquired from engineering stress-strain curves are collected in Table 8.

**Table 8.** Mechanical characteristics of all groups.

Characteristic \ Group №	1	2	3	4	5	6	7	8
Ultimate tensile strength, MPa	838.6	450.8	562.6	709.0	411.4	471.1	715.6	466.3
Yield stress, MPa	665	325	415	445	280	340	625	355
Strain-to-fracture ( $\Delta L/L_0$ )	0.035	0.114	0.139	0.139	0.102	0.145	0.065	0.090
Modulus of resilience, MJ/m <sup>3</sup>	1.03	0.84	0.88	0.94	0.35	0.68	1.51	0.51
Plastic-to-elastic strain ratio ( $\Delta L_{\text{plast}}/\Delta L_{\text{elastic}}$ )	0.87	2.40	3.44	4.37	3.41	3.25	1.53	3.29
Elasticity modulus <sup>1</sup> , GPa	6.53	18.53	21.26	16.88	33.11	20.25	8.20	22.26
Poisson's ratio	0.230	0.292	0.331	0.289	0.370	0.308	0.359	0.250

The stress-strain behavior of the other two field-averaged components of the strain tensor  $e_{xx}$  and  $e_{xy}$  is presented in Figures 23a and 23b, respectively. Blue dotted lines (groups

<sup>1</sup> The sources of such low values of elasticity modulus are discussed in the text further.

1-3) refer to C61800-based alloys; solid red lines (groups 4-6) – to C18400-based; green dashed lines (groups 7-8) – to CB480K-based. The  $\sigma_{xy}$  graph of group 8 was excluded from consideration because of the unstable behavior of the strain-sensor gauges readings. It can be found in Figure 24. The ultimate absolute values of  $e_{xx}$ ,  $e_{xy}$ , and  $e_{yy}$  are summarized in supplementary Table S.1.

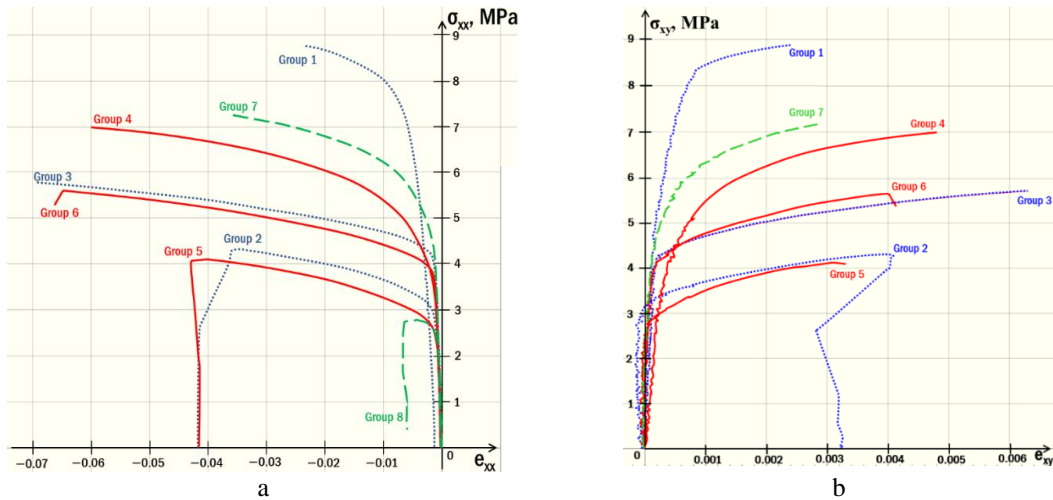


**Figure 23** – Stress-strain behavior of  $e_{xx}$  (a) and  $e_{xy}$  (b) components of a strain tensor.

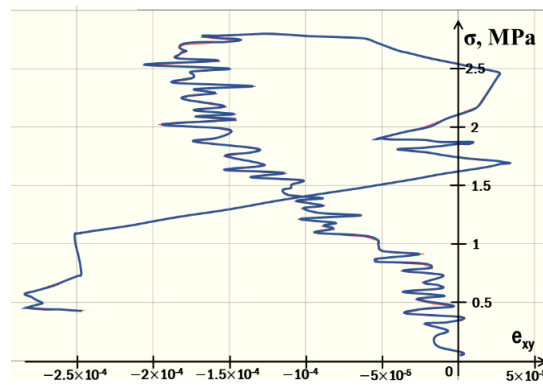


**Figure 24** – The  $\sigma_{xy}$ 's behavior of group 8.

It is seen from Table 8 that C61800-based specimens (groups 1, 4, and 7) had better tensile mechanical characteristics (moduli, YS, UTS) than other groups. The highest average UTS was demonstrated by groups 1, 4, and 7. The lowest mechanical strength was

associated with C18400-based parts: group 5, group 2, and group 8. Therefore, it was seen that laser-deposited Fe-Cu materials based on SS had the highest tensile mechanical strength combined with C61800. Binary materials with C18400 demonstrated the worst quality. The CB480K-based alloys had intermediate UTS characteristics.

Analysis of the obtained values of UTS and comparison with recently published related studies demonstrated the excellent mechanical characteristics of the fabricated C61800-based parts. The results presented by I. Sen et al. [165] showed the lower values of the engineering UTS of 0 wt.% and 3 wt.% Cu-added stainless steel 304H annealed up to 100 h. The highest measured UTS value was equal to 710.5 MPa. The tensile mechanical testing of Cu-SS FG structures deposited directly and through the Deloro 22 intersections [166] were estimated to be  $648.2 \pm 25.4$  MPa UTS for D22-SS FG structures,  $720.1 \pm 13.3$  MPa for pure D22 alloy, and showed comparatively poor results for multi-metallic structures with copper:  $226.2 \pm 4.4$  MPa for Cu-D22-SS specimens, and  $124.4 \pm 30.2$  MPa for Cu-SS. It was higher than SLM-fabricated 99.2 wt.% Cu (195-211 MPa;  $49 \pm 10$  MPa) [166-168] and cold spray-produced CP copper (125 MPa) [166,169], but were relatively lower than any specimen presented above in Table 8 (including 75% bronze – 25% steel groups, and groups with alternating layers of bronze and steel too). The maraging steel-copper functional bimetal fabricated via the SLM combined with the subtractive process [170] also showed lower UTS (not more than 557 MPa, which was slightly higher than that of copper [170] but lower than the UTS of the C61800-based groups 1, 4, and 7 showed in Table 8).

Moreover, not only AM-fabricated Fe-Cu and CP Cu structures showed lower UTS. Even the SS specimens, laser-deposited using different building directions (0°, 15°, 30°, 90°), demonstrated a lower UTS: less than 700 MPa – in the study [171]; from ~220 to ~510 MPa – in the work [172] (it was less than UTS of the bar stock (~600 MPa) [172]). Because the building direction of 90° to the direction of loading exhibited higher UTS [171,240], it was expected to be possible to improve the tensile mechanical characteristics of all discussed groups 1-8 by varying their building directions. P. Guo et al. [240] demonstrated a ~17% increase of UTS of the high-power laser deposited SS 316L (from 770 to 900 MPa), and Zhang et al. [174] reported about 19% UTS improvement (536 → 639 MPa) provided by changing the building direction from 0° to 90°. The 90° building direction also revealed a preferable microstructure because of a higher homogeneity of the alloy. At the same time, 0°-built parts consisted of large dendritic grains due to the specificity of the thermal history (the high-temperature gradient between the melt pool and the previously deposited areas) [240]. These grains were produced by epitaxial nucleation.

The specimens of groups 2-4 and 6 showed the highest values of the strain-to-fracture (from 0.114 to 0.145). All of them were of the quasi-homogeneous structure without compositional gradient and mostly contained the tin bronze CB480K (groups 3 and 6). The lowest values were related to aluminum bronze C61800. This material was also associated with high mechanical strength; therefore, these two factors pointed to favorable mechanical properties expressed in the high failure-and-strain resistivity.

From Table 8, it was seen that all 75/25 wt.% alloys (groups 4-6) had low average specific proportional strain energy. The same could be said about groups with C18400

(2,5,8). Groups with C61800 (1,4,7) had the highest value of this parameter. The ultimate value of the specific proportional strain energy was observed in the case of C61800+SS alternating layers' material and amounted to 1.51 MJ/m<sup>3</sup>.

Engineering tensile stress-strain curves allowed the estimation of residual plastic strain and elastic strain, which entirely disappears when a specimen fails. Only group 1 demonstrated an average plastic-to-elastic strain ratio less than unity among others. It means that the failure occurred during low plastic strain in this case. The applied stretching force caused internal stresses, which were lower than critical values that triggered an intercrystalline slip (initial phase of significant plastic strain) but were higher than stresses that could break interatomic bonds (beginning of the elastic strain). This phenomenon was observed only in the group of C61800-based specimens.

Overall low value of elasticity moduli can be associated with porosity and gas pockets in the specimens. Their presence was proved by the results of the fracture analysis (see §5.4). Besides, it was seen from Table 8 that the highest average values of elasticity modulus (up to 33.1 GPa) corresponded to groups 5 and 8 (both – based on C18400). These materials also had the worst mechanical strength, but the highest brittleness. The lowest elasticity modulus was associated with groups created from C61800 and SS (groups 1, 4, and 7). Therefore, it could be concluded that these materials had both high mechanical strength and high elasticity. The current results were significantly lower (6.5–16.9 GPa versus 35.6–43.2 GPa) compared to previously measured elasticity modulus of alternating layers' structures published in [118]. This distinction could be associated with the chemical compositions of the bronze powders, their grain particle's size and shape, amount and size

of as-built parts porosity. Also, it should be noted that measurements discussed in [118] were conducted using another method. They were performed locally, mainly near the border zone between steel and bronze, which was enriched by intermetallics and tended crack formation. The difference between average and local elasticity modulus values was proved using the virtual local extensometer function in the Vic-3D. It was shown that the local strain differed from the section's strain between two nearby points. It also differed from the overall specimen strain.

As expected, the elasticity modulus of all Fe-Cu structures based on SS was lower than the same one of the laser-deposited SS (6.5–33.1 GPa versus ~150–200 GPa [172]). Groups fabricated from the tin bronze CB480K recognized intermediate elasticity modulus values compared to other groups (from 20.2 to 21.3 GPa).

Similar research on the mechanical properties of CP SS parts fabricated by the DED was conducted by S.-H. Park et al. [175] using almost the same technological installation (InssTek MX-400). The elasticity modulus and the Poisson's ratio were indirectly determined by measurement of velocities of the GHz-THz range ultrasonic waves that occurred in the material during a post-treatment – surface shallow melting-mechanism laser polishing using the femtosecond laser system. The resulting elasticity modulus values ranged from approximately 209 GPa to 232 GPa (the direct measurement using tensile testing approved the accuracy of the indirect method based on the ultrasonic waves). This result was also predictably higher than the average results in Table 8 and even higher than the findings of [172]. Therefore, it could be concluded that adding 50 wt.% and more

bronze in the SS powder significantly lowers the elasticity modulus of the resulting DED-fabricated binary Fe-Cu system part.

Groups with the highest bronze fracture (№№ 4-6) exhibited higher average elasticity modulus (23.41 GPa) than groups 1-3 (15.44 GPa) and gradient groups 7-8 (15.23 GPa). Therefore, they were more rigid and less elastic. It was correlated with the results of the  $e_{xx}$  and  $e_{yy}$  behavior analysis and pointed to the expected decrease of the mechanical strength in the areas of Fe-Cu FGMs with the highest amount of bronze. Still, according to the stress-strain maps of  $e_{xx}$  and  $e_{xy}$  (Figures 23a,b), materials with the most significant stress tensor components  $\sigma_{xx}$  and  $\sigma_{xy}$  had almost the lowest corresponding strains  $e_{xx}$  and  $e_{xy}$ , respectively. They also had the most prominent angles between linear sections of stress-strain curves and abscissa axes. The lengths of these linear sections had the highest values too. These particularities contrasted with the lowest elasticity moduli of specimens of groups 1 and 7 determined using engineering stress-strain curves (see Table 8). Therefore, the elastic behavior of the C61800-based alloys had an anisotropic character along the build direction and orthogonal. Although it ensured good isotropy within a plane of a single layer as stated above. This result had good agreement with the literature mentioned above [171,172,174,240]. The unusual shape of  $\sigma_{xx}(e_{xy})$  and  $\sigma_{xy}(e_{xy})$  diagrams in the case of group 8 didn't show a clear relationship with the resulting value of its elasticity modulus (see Table 8), which was presumably a result of a significant inhomogeneity of this alloy. The reason for this unexpected stress behavior is unclear yet and should be explicitly studied.

The average yield stress estimation results show that C61800-based groups (1 and 7) had comparatively high average yield stress values (625 and 665 MPa). It was higher than

the SLM-fabricated SS (440 MPa) [176]. Moreover, they were even comparable with additive manufactured TiB<sub>2</sub>-reinforced SS matrix nanocomposite – sheet molding compound (SMC)-5 (~830 MPa at room temperature and ≤520 MPa at temperatures of 600°C and higher) and SMC-10 (~980 MPa at room temperature and ≤410 MPa at temperatures of 800°C and higher) [177]. The 0.2% yield stress measurements of DED-fabricated SS samples presented by S. Kersten et al. [172] also showed lower average values (from 212.1 MPa to 285.56 MPa in dependence from the build direction). The SS yield stress demonstrated in the study [171] in reliance on a building direction was higher than the findings of [172]. Nevertheless, it was also lower than the yield stress of the C61800-based alloys of groups 1 and 7. This significant property of materials based on the C61800 considered their high mechanical strength and allowed them to be implemented as parts of high-loaded equipment. On the other side, the lowest values of the YS were attributed to the C18400-based materials of groups 2, 5, and 8 (from 280 to 355 MPa). As mentioned earlier, these materials were also characterized by the lowest UTS. The CB480K-based materials of groups 3 and 6 exhibited intermediate yield stress, near 415 and 340 MPa respectively.

The possible way of an increase of the YS in AM-fabricated parts of the system with positive enthalpy of mixing (as Fe-Cu) could be a grain refinement. A. Zafari and K. Xia [178] reported that compressive yield stress increased by a factor of 2.2 from ~400 MPa in an SLM-produced Fe to ~900 MPa in immiscible Fe-Cu parts with 250 nm average grain size. It was associated with liquid separation, monotectic reaction, and solid-state phase transformations upon cyclic heating. These parts also showed an ultrahigh ultimate

compressive strength of ~1200 MPa. The same increase in the YS of the Fe-Cu system due to grain refinement could be expected in the case of the DED technology too.

The notable specificity of groups of FG alternating layers' alloys was the existence of the distinctive plateau between the elastic and the plastic strain, which was characterized by the increase of absolute elongation with almost constant internal stresses (see supplementary Figures S.13 and S.17). This plateau was associated with 700 MPa internal stress in the case of a specimen of group 7 and with 280 MPa in the case of a specimen of group 8. The last was equal to these specimens' yield stresses. The visual analysis of the loaded specimens correlated with the existence of this plateau by the appearance of the Lueders-Chernov's lines dense network on the flat surfaces of the stressed specimens. These lines were approximately 45° angle to the axis of load and are attributed to the displacements of the crystal planes with ultimate shear stresses.

An average Poisson's ratio of all experimental groups was calculated using the results of the evaluation of principal and additional components of a strain tensor through the Vic-3D. As predicted before experiments, all materials showed a Poisson's ratio of 0.2 – 0.4 average value. Comparing the resulting values with CP SS fabricated via traditional methods showed that Poisson's ratio (0.28 – 0.31) was close to the presented average results of groups 2, 4, and 6. Almost the exact Poisson's ratio (0.33) of laser-deposited SS 316L was discussed in the study [171]. Still, the results for the same material presented in [175] were significantly lower – from ~0.182 to ~0.197 independently from the measurement method.

It was seen from Table 8 that the large average Poisson's ratio values ( $>0.308$ ) were attributed to groups 6, 3, 7, and 5 (placed in order of the average Poisson's ratio ascending), and had no apparent coherence with the bronze-steel balance and the kind of the applied bronze. The same was observed for the lowest values ( $\leq 0.292$ ), which were presented by groups 2, 4, 8, and 1 (placed in order of the average Poisson's ratio descending).

Overall, better mechanical properties of C61800-based alloys may be linked to the closer characteristics of SS 316L & C61800 in comparison to SS 316L & C18400 and SS 316L & CB480K in terms of closer mechanical strength values, lattice types and parameters (see Table 3).

### **5.3 DIC Analysis**

The surface distribution of the principal strains  $\epsilon_1$  of all groups immediately before breaking generated by Vic-3D is demonstrated in Figure 25. The red and orange areas correspond to the large strains and the blue and purple – to the small strains. Black arrows in Figures 25e and 25h indicate strain concentrators and expected locations of defects discussed in the text. The direction of principal strains was observed along the build direction – Y axis in Figure 26.

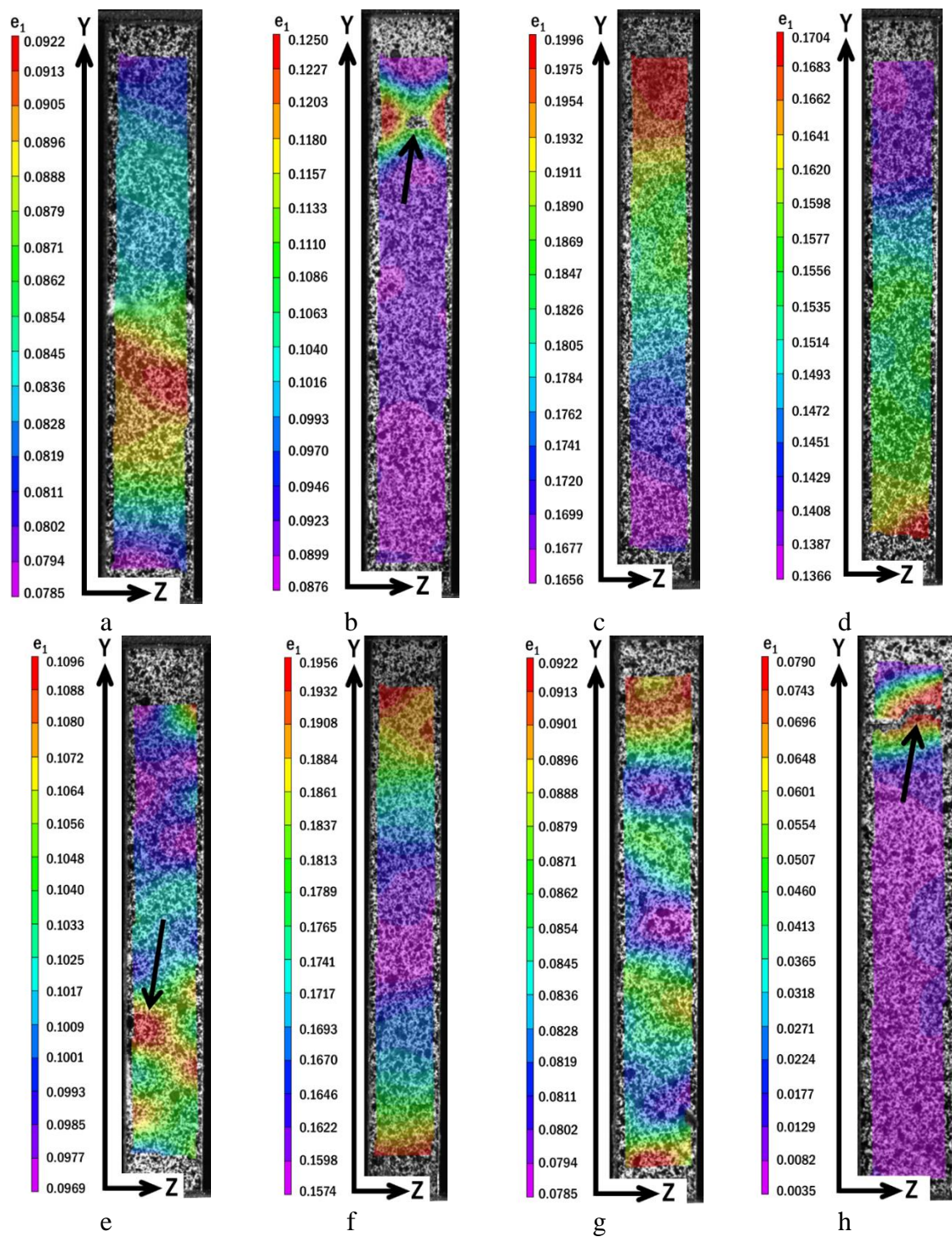


**Figure 25** – Distribution of principal strains in specimens of all groups before breaking. a-h: groups 1-8, respectively.

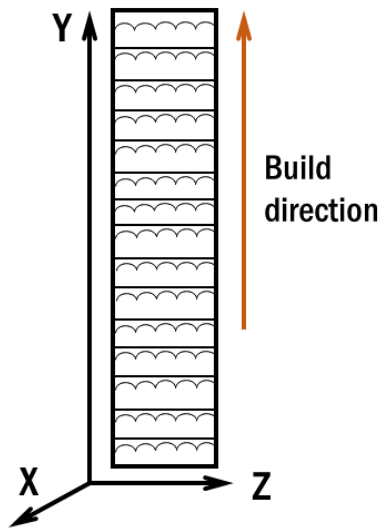


**Figure 26** – The relationship between build direction and axes X, Y and Z.

It is seen from Figure 25g that FG group 7 of the alternating layers' alloy had a double-sided (up and down) increase of a principal strain alongside the vertical axis with evidently alternating strain value and two areas of the strain concentration. The DIC strain maps of the similar alternating layers' structure fabricated from two kinds of SS (420 SS and C300 maraging steel) in [179] also exhibited the strain alternating between different layers of the specimen. Still, the period of this alternative was relatively less. This difference could be associated with higher intermixing of the C61800 and SS compared to 420 SS and C300 maraging steel, which could also be seen from the microstructure patterns provided by C. Tan et al. [179]. Another possible source of this difference was a more significant degree of the epitaxial growth between the layers inherent in the alternating-layered DED-processed multi-material structures [180]. The possible increase of intermixing was also approved by the  $e_{xx}$  strain distribution of an FG structure created from 50 alternating Fe-Cu laminated sheets via the accumulative roll bonding [181]. In this

structure, the evident alternating character of strain distribution was also erased. The high intermixing leading from the layered to the network-like structure was observed with an increase in the number of layers. Another group with alternating layers (group 8) didn't exhibit the alternating strain pattern. Still, it showed an intense ellipsoid-like concentrator in the top area, which probably corresponded to the defect in this specimen. One specimen of this group didn't break entirely but suffered cracking in the area of maximum strain concentration. The same strain distribution, as in group 8, was observed in group 2, also created from SS and C18400 (defect caused a hyperboloid-like shape of major strain distribution near the strain concentrator marked by the arrow in Figure 25b).

Except for group 7, only group 6 also had two areas of ultimate strains. Still, the non-gradient structure of the material didn't provide any alternating internal strain value, as was seen in the FG structure of group 7. It was also visible that no groups created from the chromium bronze C18400 had more than one area of maximum strain.

Additionally, it should be noted that a smooth character of the principal strain variation was inherent to all groups with a 50/50 wt.% ratio of steel and bronze, to group 4 (75/25 wt.% ratio of C61800 and SS), and to group 8 (alternating layers created from C18400 and SS). It indicated the higher homogeneity of these alloys and the absence of significant structural defects that could cause the multilateral strain concentration map.

The stress-strain behavior of the  $e_{xx}$  (Figure 23a) and  $e_{xy}$  (Figure 23b) components of all groups demonstrated that there was no clear correlation between ultimate stress and type of mixing (50/50 alloys; 25/75 alloys; gradient alloys). The dependence between the type of mixing and ultimate values of  $e_{xx}$  and  $e_{xy}$  wasn't also determined. However, such

reliance existed for different types of bronze. It was seen that aluminum-bronze-based groups (1,4,7) are characterized by the biggest stress  $\sigma_{xx}$  corresponding to the minor strain (Figure 23). The same was observed in the case of shear stress  $\sigma_{xy}$  (Figure 23b). The biggest values of stress tensor components pointed to better expected mechanical characteristics of C61800-based materials. The behavior of  $e_{xy}$  (a shear strain component) was almost the same as that of  $e_1$  (see supplementary Figures S.1 – S.17) everywhere except group 8. This group was characterized by the most unusual shape of the  $e_{xy}$  diagram (see Figure 24). As it was mentioned above, this graph was excluded from consideration because of the suggestion of the unstable behavior of the strain-sensor gauges readings.

But it should be noted that such a chaotic oscillation of the  $e_{xy}$  absolute value and sign could also be caused by the existence of the significant strain concentrator in the top area of the specimen (marked by the arrow in Figure 25h), which was presumably provoked by the structural defect in the alloy. The component of a shear strain ( $e_{xy}$ ) had the most significant value (0.0063) in the case of non-gradient 50/50 wt.% alloy of group 3 with the biggest absolute  $e_{xx}$  and  $e_{yy}$  values (0.069 and 0.18, respectively). Contrarily, a non-gradient 25 wt.% CB480K – 75 wt.% SS group 6 alloy with almost the same absolute  $e_{xx}$  and  $e_{yy}$  values (0.066 and 0.17 respectively) had a 1.5-times lower  $e_{xy}$ , which was equal to 0.004. It pointed to the decrease of the shear strain in the alloy with a higher CB480K constituent. Groups 4 and 5 based on C61800 and C18400 respectively, contrarily demonstrated an increase of the shear strain by the growth of their bronze fraction compared with groups 1 and 2. The gradient group 7 alloy also exhibited a low absolute shear strain (0.0029), as observed for groups 1-2 (0.0024–0.0031). The shear strain of

group 8 had the lowest absolute value (as well as  $e_{xx}$  and  $e_{yy}$ ) among all groups (0.00028) and was characterized by a negative sign. It means that the shape change of an elementary 2D-square in the material by an external stretching load had another direction than all other discussed alloys. This unusual behavior could also be attributed to the existence of a strain concentrator, which location was marked by the arrow in Figure 25h. Overall, the biggest absolute values of  $e_{xx}$  were associated with CB480K-based alloys (groups 3 and 6, Figure 23a), which also had comparatively big values of  $e_{xy}$ .

A comparison of  $\sigma_{xx}$  (Figure 23a) and  $\sigma_{xy}$  (Figure 23b) maps showed that they had almost a symmetric shape. This property of a strain tensor is pointed at high homogeneity and isotropy (in the x0z plane) of the fabricated alloys. It was also proved by the results of optical microscopy and SEM with high magnification (see Chapter 4), which showed a low structural irregularity within a single layer of alloy. Further, if we compare two groups with the highest values of  $\sigma_{xx}$  and  $\sigma_{xy}$  according to Figure 23a,b, we will see that higher stress with lower strain was related to material with a more considerable average content of Fe, Cr, Ni, and Mo but lower Cu and Al (Tables 4 and 5). Therefore, there were reasons to expect Fe, Cr, Ni, and Mo to be desirable elements in the C61800-based Fe-Cu transitional zones of DED-fabricated FGMs, whereas Cu and Al – are undesirable. Subsequent research should mainly elaborate on this hypothesis.

In the SEM micrographs with higher magnification (Figure 13b,c), which were taken from the central areas of group 1 specimens, a fine-grained microstructure with the existence of both cellular, dendritic, and cellular-dendritic elements was also demonstrated. The average porosity size visible in Figure 13b,c micrographs was lower than 1  $\mu\text{m}$ , and

cracking wasn't presented in these regions of the deposits. A study of another C61800-based group with high mechanical characteristics (group 7) didn't reveal the same microstructural patterns and elemental composition. Furthermore, the correlation between microstructure and high mechanical properties of the studied DED-fabricated Fe-Cu materials of groups 1 and 7 should be explicitly discussed.

Unlike C61800 + SS (50/50 wt.%), the EDX microanalysis didn't point to the existence of the molybdenum in the alternating-layered C61800-based alloy. It could be explained by the absence of a  $\delta$ -ferrite in contrast to group 1, which was approved by the results of XRD analysis discussed in §4.3. Cellular-shaped element (Figure 13d, point 1) appeared as a Fe-based region with a 15.15 % atomic fraction of copper and almost the same as chromium. The dendritic element had a significantly lower Fe percentage (21.5 at.%), lower Cr (5.01 at.%), and higher Cu and Al amounts (55.05 at.% and 14.65 at.%). The last point, 3, which corresponded to the matrix, was located in a Cu-based area with low fractions of Fe (4.78 at.%) and Cr (0.84 at.%).

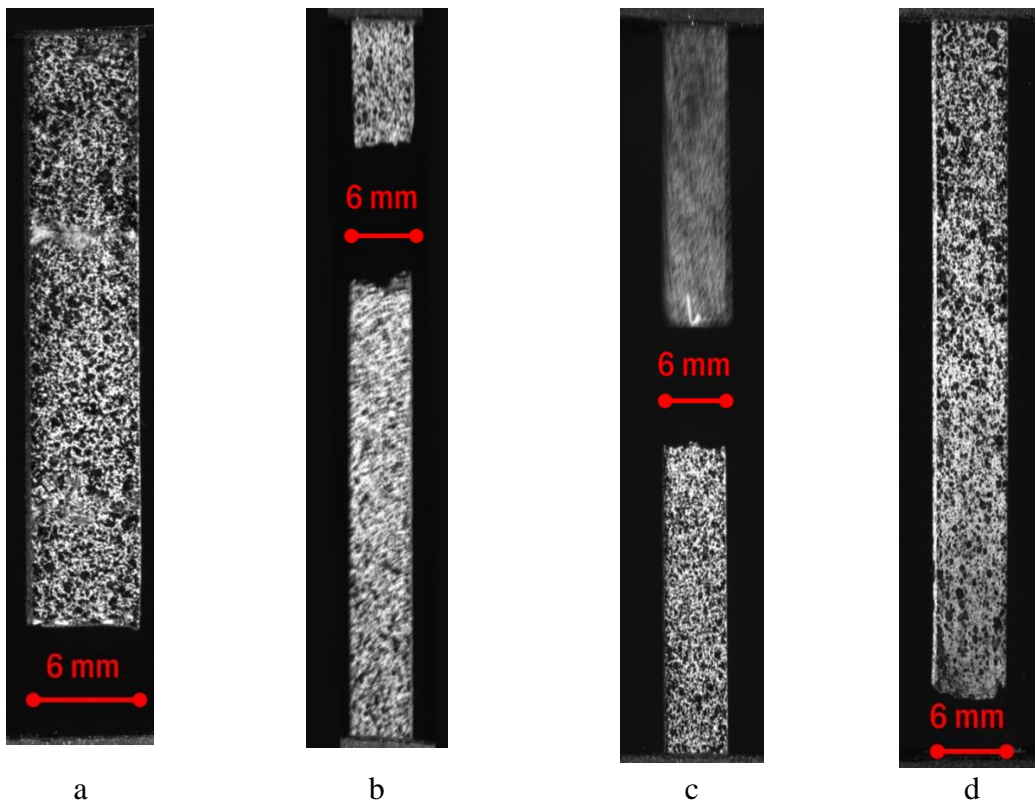
SEM micrographs of group 7 (Figure 13f) and group 1 (Figure 13c), which were taken at x10,000 magnification, showed less grain refinement of C61800+SS (alt.) than that of C61800+SS (50/50 wt.%) resulted in lower UTS and YS (see Table 8). The amount and porosity size of group 1 were approximately equal to group 7. Still, the SEM images of group 1 (Figure 13b,c) revealed the existence of substantial void defects like gas pockets on the left side of the micrographs. The same pockets were observed by F.F. Noecker and J.N. DuPont in the Cu-rich area of the DEDed FG slab in the study [224]. These defects, nevertheless,

didn't lower the mechanical properties of the fabricated parts of group 1 in our case in comparison to other groups.

The {FCC austenitic  $\gamma$ -Fe}  $\rightarrow$  {BCC ferrite  $\alpha$ -Fe} phase transformation could also increase the mechanical strength of fabricated C61800-based Fe-Cu alloys compared to C18400-based and CB480K-based ones (see the results of the XRD analysis in Chapter 4).

#### 5.4 Fracture Analysis

Figure 27 shows the frames taken by the camera at the moment of breaking specimens of all groups. Using these frames, the common failure areas of all groups could be found, and suggestions about the ultimate stress zones could be made. Dimensions (6 mm) are shown for clarification of the scale. Several figures (27b,f) are blurred because of specimen vibration at the moment of its failure.



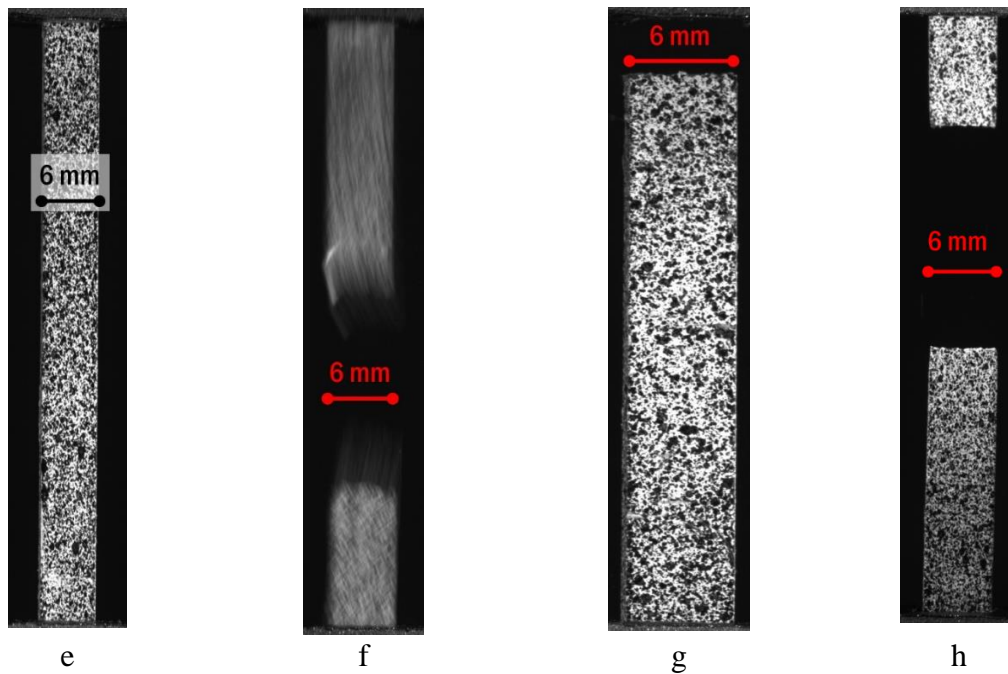


**Figure 27** – Frames of breaking of all groups. a: group 1; b: group 2; c: group 3; d: group 4; e: group 5; f: group 6; g: group 7; h: group 8.

The main dependencies observed from all breaking frames (Figure 27) are discussed below.

- The major part of the 50/50 wt.% specimens (groups 2 and 3), except C61800-based, failed in the middle area. The same happened with groups 6 (75/25 wt.%) and 8 (alt. layers). There were no C61800-based specimens that failed near the middle area.
- Specimens of groups 1, 4, 5, and 7 mainly failed inside the grips. The major part of these groups was fabricated from the C61800. There was no apparent coherence between the steel-bronze proportion (50/50 wt.%, 75/25 wt.%, or alt. layers) and the «near the grips» failure character.
- Specimens of C18400-based groups 2 and 8 with evidently observable strain concentrators (see Figure 25b,h) failed in the location of these concentrators (Figure

27b,h). Besides, these groups showed comparatively poor mechanical characteristics (see Table 8). C18400-based DED-fabricated Fe-Cu alloys had an excellent propensity for lowering mechanical strength due to undetermined issues. The last could refer to microstructural defects of an unclear nature. The fractured surfaces undoubtedly didn't reveal the types and sources of the defects. Therefore, the reasons for such behavior should be studied specifically using an SEM and XRD analysis, which is expected to be done in the upcoming research.

- The location of the ultimate strain of group 1 (colored by red in Figure 25a) didn't correspond to its breaking area (Figure 27a). It could be a result of two possible reasons. The first one – the scope of the ultimate strain could be hidden by the bottom grip and wasn't shown in Figure 27a. The second one is that areas of the ultimate local strain and ultimate local stress were different. The second suggestion points to the possibility of brittle intracrystalline character of the failure (failure during low plastic strain). This suggestion is proved by the plastic-to-elastic strain ratio's low value (0.87) (see Table 8).
- It was seen from Figure 25c that the most prominent strain was observed in the top part of the group 3 specimen. Nevertheless, its breaking occurred in the middle part (Figure 27c). It implies that this group's areas of ultimate strains and ultimate stresses were different. In other words, the failure occurred in the region with a comparatively low tensile strain. But in this group, a high plastic-to-elastic strain ratio was observed (see Table 8). Hence, it means that the failure hadn't an intracrystalline character, unlike group 1. This considerable absolute strain value

also indicated it in the region of failure of group 3 (see Figure 25c). In the case of group 1, this value was 0.0785 or lower (see Figure 25a). Therefore, a mismatch between the areas of ultimate local strains and ultimate local stresses was unclear in the case of group 3.

- The specimen of group 4 failed in the area of maximum strain (Figures 27d and 27d). The specimens of groups 2 and 8 did the same. It ensured the correspondence between areas of ultimate local strains and stresses in the case of group 4.
- The specimen of group 5 suffered cracking inside the grips (Figure 27e). Therefore, it could be concluded that either its ultimate strain area is located inside the grips (see Figure 25e) or the areas with ultimate stress and strain are different. The same was stated above in the case of group 1.
- The group 6 specimen had two zones of the ultimate stresses (Figure 25f) but it failed in its middle area (Figure 27f). As mentioned above, in the case of group 3, the failure occurred in the region with a comparatively low tensile strain. Plastic-to-elastic strain ratio of this group was also high (it was equal to 3.25, see Table 8), and the absolute strain value in the failure region was approximately 0.17. Hence, a conclusion about the intracrystalline failure, in this case, was not obvious.
- The group 7 specimen also had two areas of ultimate strains (see Figure 25g), and it failed near one of these zones (Figure 27g). Hence, this group's stress and strain distribution maps were expected to be similar.

Comparison of our fracture behavior with results of the pure SS specimens deposited using different building schemes [171] with nanoscale porosity showed that all

of them failed in their central areas without clear dependence on the building direction, which was the variable parameter in [171]. Therefore, it could be expected that the addition of the C61800 to the SS matrix led to the transition of the failure region from the central parts of the specimens to their tails.

One prepared C18400 + SS gradient specimen didn't fail after the tensile test but only cracked in its middle area. This macroscopic phenomenon of partial failure had similar behavior with a microscopic crack arrest [182] provided by specific elements in the crystalline structure of the specimen, such as a  $\delta$ -ferrite in the binder jet-printed SS. The existence of the  $\delta$ -ferrite in fabricated specimens, which was discussed above, proved a suggestion that exactly  $\delta$ -ferrite could be responsible for this phenomenon. In Figure 28, the partially-failed specimen demonstrated the external pattern of the crack at the surface. Other fracture surfaces are shown in Figure 29.

The most common type of breaking of all specimens was a brittle fracture. The same result was demonstrated by P. Guo et al. [240] in the case of SS alloy manufactured by the high-power DED. Nevertheless, this kind of fracture was not common for Cu-based AM-fabricated alloys and gradient structures with alternating layers. The roll-bonded alternating structure described by N. Koga et al. [181] showed that an increase in the number of layers mainly suppressed the brittle fracture, presumably due to grain refinement. It was pointed out that the neighboring Cu layers should suppress the brittle fracture of the Fe layers, which was observed on the pure Fe sheets with 20  $\mu\text{m}$  grain size. However, in our case, a shear fracture was exhibited only by group 2 (C18400 + SS 316L (50/50 wt.)) and group 7 (C61800 + SS (alt.)). X. Zhang et al. showed the exact

mechanism of a ductile fracture with many voids and dimples [183]. In that study, the Cu-D22-H13 FG alloy was fabricated from the copper and H13 tool steel through the Deloro 22 interlayer via the DED. The ductile fracture mechanism was also described in the example of a SS-Cu FGM with ~200 MPa UTS [166]. In that study, the FGM was also fabricated via the DED through the interlayers of the same nickel-based alloy. This FGM failed in the Cu zone (contrarily, the D22-SS specimens produced without copper exhibited a brittle fracture surface without dimples but with several micro-cracks). Khalid Imran et al. [184] studied the H13-Cu FG alloy after the DED process and characterized the absolute ductile fracture morphology with dimple fractures observed near the crack nucleus. H. Shi et al. [185] described all kinds of rupture (brittle, shear and ductile plastic, and transcrystalline) in the case of pre-alloyed Fe-Cu-based multi-material composite in dependence from the molten state content. All of them were also presented in the specimens of groups 1-8. They also depended on the wt.% chemical composition of the alloy. The transcrystalline fracture was common primarily for C18400-based groups (such as group 5), and the intracrystalline rupture was observed in the case of specimens based on the C61800 (groups 1 and 7).

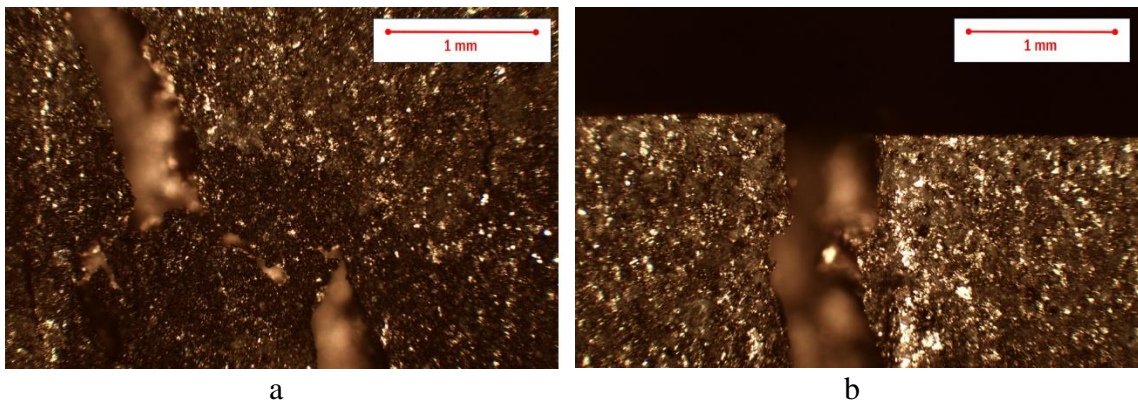


**Figure 28** – Crack at the surface of group 8 specimen (a, b).

Figure 29 (a-h) demonstrates selected macrofractography images of specimens of all groups. White lines in the fractography patterns show borders of the images taken from different areas of the same specimen fragment or with different focal length of the microscope. If the scale of images is different, it is specified for each image separately.

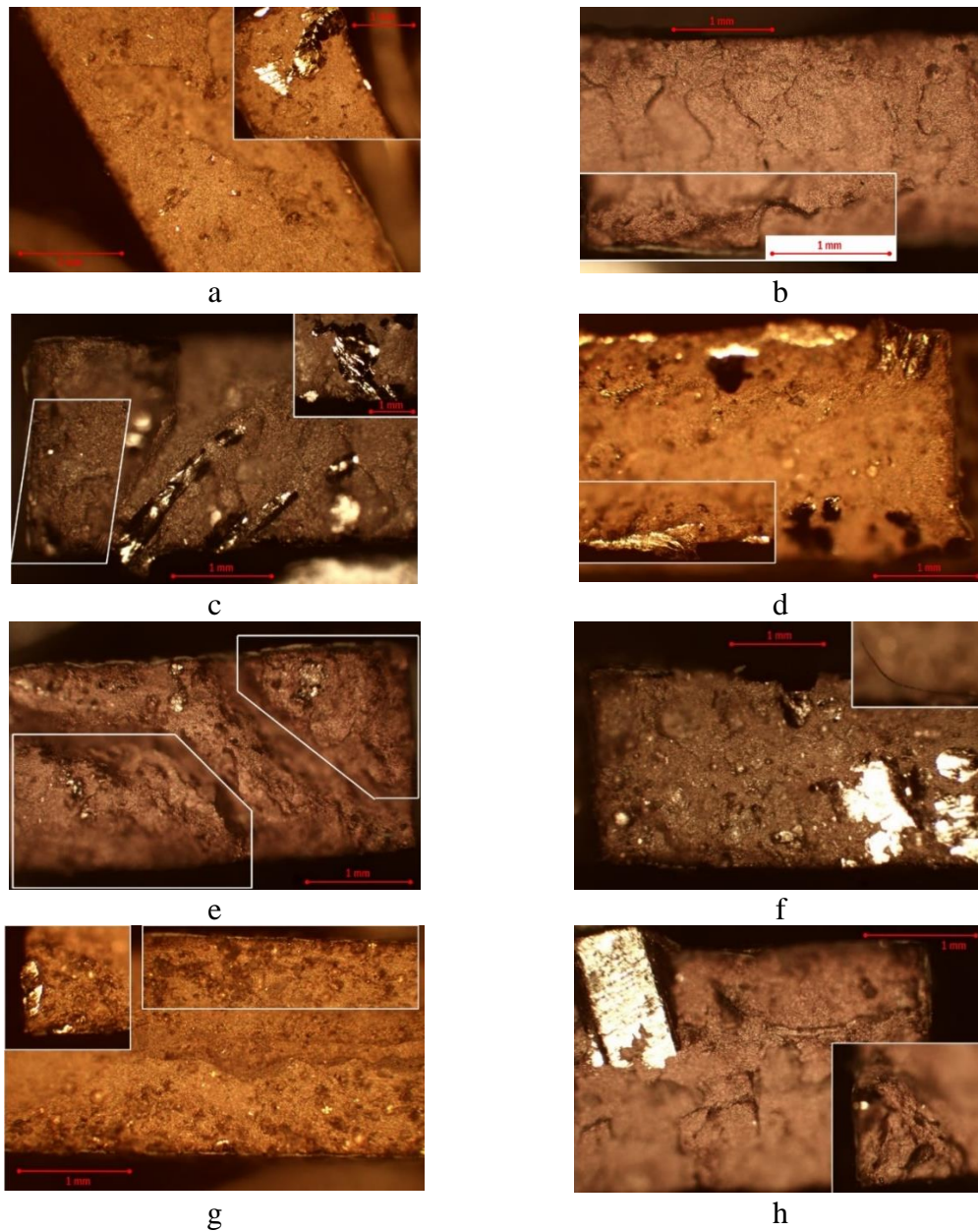


**Figure 29** – Selected fractography images of the specimens of all groups. a-h – groups 1-8, respectively.

## 5.5 Microhardness Analysis

The microhardness and additional elasticity modulus measurements were performed with a purpose to understand how does the DED process exactly influence over microhardness of the part and, as it was said before, to identify if there was local microhardness and brittleness increase in the transitional areas of the samples caused by intermetallics growth. The microhardness and elasticity modulus research were performed on two groups of samples – series №1 and №2 (see section 3 of the current study). Scheme of testing samples of the series №1 is shown in Figure 30. The measurements 1 – 3 and 10 – 21 were performed on the steel areas of the samples' transitional zones, the measurements 4 – 6 – on the bronze areas and the measurements 7 – 9 and 22 – 24 – directly on the SS – aluminium bronze border. The undersides of the samples under discussion are beneath in all three photos demonstrated in Figure 30.

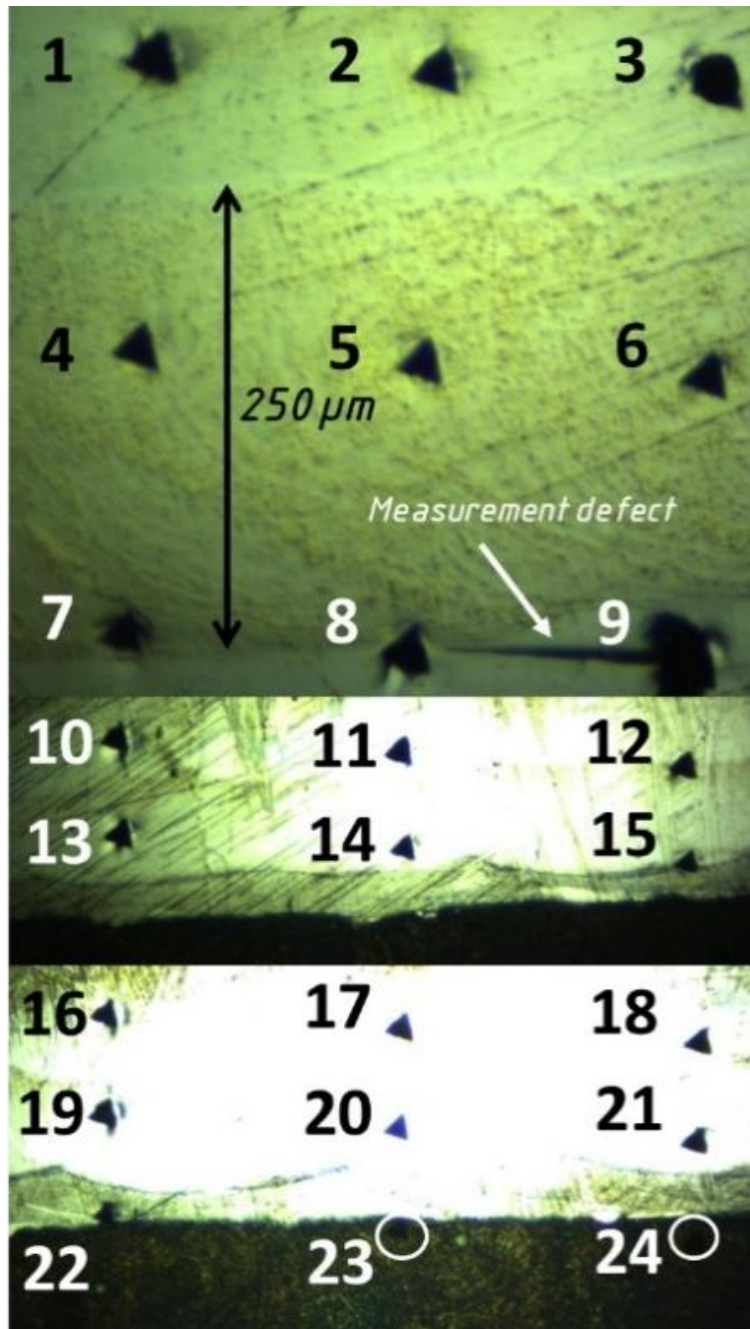


**Figure 30** – A microhardness and elasticity modulus research №1 performed with the different experimental samples' series №1.

The scheme of the second microhardness and elasticity modulus research performed on the samples' series №2, which had a multilayer structure, is shown in Figure 31. The underside of the sample demonstrated in the photo is beneath.

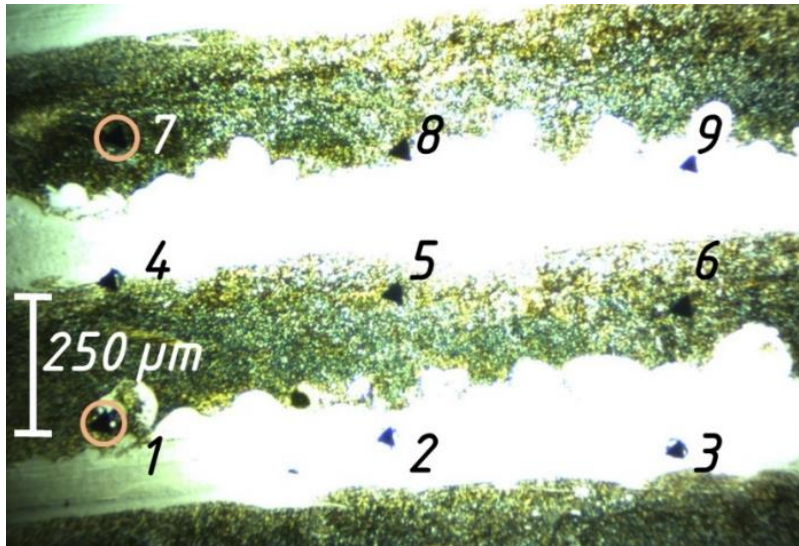


**Figure 31** – A microhardness and elasticity modulus research №2 performed with the experimental samples' series №2.

The results of all measurements performed on the samples series №1 and №2 are demonstrated in the graphs (Figure 32) and in Table 9. As it is seen, the total number of test points for the samples series №2 was less than the total number of test points for the samples series №1. The duration of each measurement cycle was 15 min.

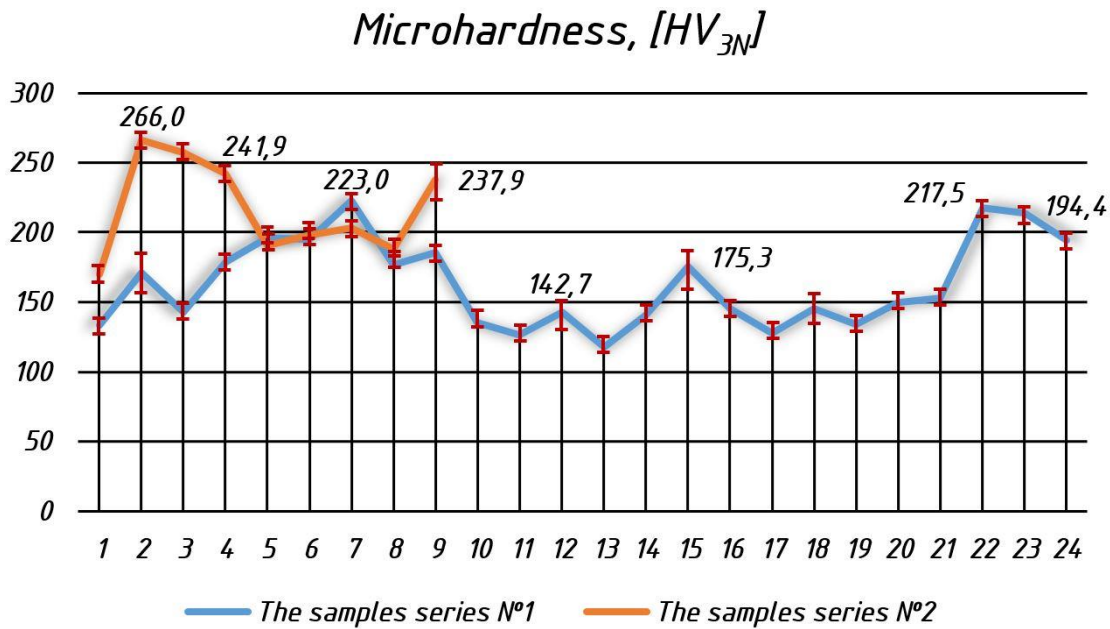


**Figure 32** – The microhardness research results.

**Table 9.** The results of the microhardness and elasticity modulus tests performed with the experimental samples series №1 and №2.

Point №	Microhardness, [HV <sub>3N</sub> ] (samples series №1)	Microhardness, [HV <sub>3N</sub> ] (samples series №2)	Elasticity modulus, [GPa] (samples series №1)	Elasticity modulus, [GPa] (samples series №2)
1	133.1	170.1	32.6	37.8
2	171.1	266.0	34.9	43.2
3	142.5	257.3	29.8	42.1
4	<b>178.8</b>	241.9	<b>34.2</b>	40.3
5	<b>196.1</b>	190.7	<b>33.8</b>	35.6
6	<b>194.7</b>	198.2	<b>33.7</b>	36.2
7	<b>223.0</b>	203.0	<b>36.7</b>	37.1
8	<b>177.0</b>	188.0	<b>33.5</b>	36.6
9	<b>185.8</b>	237.9	<b>34.4</b>	40.6
10	135.4		19.7	
11	126.3		19.2	
12	142.7		20.2	
13	118.0		20.1	
14	140.7		21.4	
15	175.3		23.0	
16	145.2		20.1	
17	127.4		18.7	
18	145.2		19.6	
19	134.0		19.5	
20	149.9		20.6	
21	152.6		20.1	
22	<b>217.5</b>		<b>24.1</b>	
23	<b>214.0</b>		<b>23.6</b>	
24	<b>194.4</b>		<b>21.7</b>	

It can be observed from the first research (the samples series №1) that the measurements 1 – 3 and 10 – 21 performed on the steel zones showed the lower values of microhardness than the measurements of the bronze zone (4 – 6). The results of the border measurements (7 – 9 and 22 – 24) demonstrated the highest average value of microhardness and elasticity modulus simultaneously. The reason of increase of microhardness and decrease of plasticity was growth of the brittle intermetallic structures such as FeAl. Internal stresses and deformations in the transitional zones of the samples caused by difference between the temperature expansion coefficients of materials (up to  $19.6 \times 10^{-6} \text{ K}^{-1}$

for SS 316L and at the most  $17.5 \times 10^{-6} \text{ K}^{-1}$  for aluminium bronze) were the reason of crack nucleus occurring on the grains of intermetallics.

The results of the second research demonstrated that the average value of microhardness of the samples series №2 is higher than microhardness of the samples series №1 and microhardness distribution within the volume of the samples is more regular for the samples series №2 than for the series №1.

In summary, the multilayer structures can have even a higher level of microhardness (up to  $266 \text{ HV}_{3\text{N}}$ ) and elasticity modulus (up to  $43.2 \text{ GPa}$ ) but, nevertheless, cracking of them can be entirely excluded because of reassignment of internal stresses and deformations in volume of a part as it was mentioned in Chapter 3.

## **5.6 Interim Conclusion**

This part of the research successfully evaluated and compared the essential mechanical characteristics of different groups of DED-fabricated Fe-Cu alloys. The UTS, yield stress, strain-to-fracture, modulus of resilience, plastic-to-elastic strain ratio, elasticity modulus, and Poisson's ratio were experimentally investigated for the first time for the laser-deposited alloys usable as transitional zones of Fe-Cu FGMs: quasi-homogeneous (50%–50% and 75%–25%) and gradient alternating layer's alloys based on C61800, C18400, and CB480K with SS. The best mechanical properties were shown by C61800-based alloys due to their microstructural advantages and close characteristics to SS 316L (mechanical strength, lattice types and parameters).

With a complex of microstructural testing, the DIC method showed the alternating character of the principal strain distribution in the gradient specimens. Significant strain concentrators caused by microstructural defects were observed in both gradient and non-gradient C18400-based specimens. The existence of  $\delta$ -ferrite in UNS C61800-based non-gradient alloys slowed grain growth, increased mechanical strength, and reduced fatigue properties. Precipitations of  $\text{Cr}_2\text{O}_3$  and MnO were reasons for the yield strength increase of these structures. The absence of  $\delta$ -ferrite in the alternating-layered C61800 + SS materials and their lack of grain refinement diminished the mechanical characteristics of these materials. Nevertheless, they remained high in comparison to C18400- and CB480K-based alloys.

Adding 50 wt.% and more bronze in the SS powder significantly decreased the resulting alloy's elasticity modulus. The Fe-Cu laser-deposited alloys with the highest elasticity modulus demonstrated the lowest UTS and yield stress. The C61800-based materials showed remarkable notch toughness due to the high modulus of resilience up to 1.51 MJ/m<sup>3</sup>. Overall mechanical properties of quasi-homogeneous alloys (with a 50/50 wt.% bronze-to-steel ratio) showed higher mechanical characteristics than the gradient alloys and significantly better mechanical properties than the 75/25 wt.% ratio cases. Transitional areas with 75% bronze showed lower elasticity and higher mechanical rupture than gradient and quasi-homogeneous zones with a 50/50 wt.% ratio. Nevertheless, these two cases of the Fe-Cu transitional zones are preferable for future applications where the external stretching forces in the DEDed FG tools could be planned.

High-temperature mechanical testing could also be recommended to clarify this complex situation. Furthermore, an application of thermal post-treatment and/or ultrasonic influence during the DED process would be interesting for resolving the abovementioned problems.

Microhardness and elasticity modulus increase at the transitional areas of the FG materials pointed to the existence of the brittle intermetallic phases in this area, which was proved earlier by the results of XRD analysis and optical microscopy (the last demonstrated cracking specifically in the areas of the gradient transition). Nevertheless, structures fabricated by the alternating layers' strategy exhibited even higher microhardness and elasticity modulus values, but no cracking was observed in them during optical and scanning electronic microscopy. The phase composition of such structures was discussed in Chapter 4, «Microstructural Characteristics of SS 316L – Bronze FGMs».

## Chapter 6. Thermal Properties of SS 316L – Bronze FGMs

After studying evolution of the microstructural and mechanical characteristics of Fe-Cu FGMs and quasi-homogeneous alloys, it is necessary to research their thermal parameters as they are strongly important in the light of practical application of these materials.

### 6.1 Materials, Methods, and Design of Experiment

The materials, set of specimens, and methods of making Fe-Cu structures were the same as presented in Chapter 5. All additional methods and equipment are described below.

### 6.2 Coefficient of Linear Thermal Expansion of SS 316L – Bronze FGMs

#### 6.2.1 Experimental Measurement of CLTE

CLTE was experimentally estimated using a heating plate and a hand caliper with 0.01 mm of uncertainty. Each part underwent 10 measurements of its length and width on a separate pair of prepared surfaces. A CP DED-fabricated SS 316L part was analyzed by this method too. The heating cycle was from +21 °C (the initial temperature was equal to the room temperature) to +220 °C, respectively. The maximum temperature was lower than that of low-temperature bronze annealing. It was also significantly lower than the Curie temperature  $T_c$  of the SS 316L alloy. Heating over the Curie temperature significantly changes the trend of CLTE due to changes in the material's magnetic properties [186]. The accuracy of a single CLTE calculation was estimated to be no worse than  $\pm 3 \cdot 10^{-6} \text{ K}^{-1}$ . Therefore, the uncertainty of the arithmetic mean is

$$\alpha_{\text{Br-SS}} = \pm 3 \cdot 10^{-6} / \sqrt{10} \cong \pm 9.5 \cdot 10^{-7}, \quad (51)$$

where «10» was a number of calculations. Subsequent research can optimize this uncertainty via more precise measurement methods and equipment.

Figure 33 demonstrates the experimentally obtained CLTE of all groups. The experimental CLTE for CP SS 316L was equal to  $1.82 \cdot 10^{-5} \pm 9.5 \cdot 10^{-7} \text{ K}^{-1}$ .

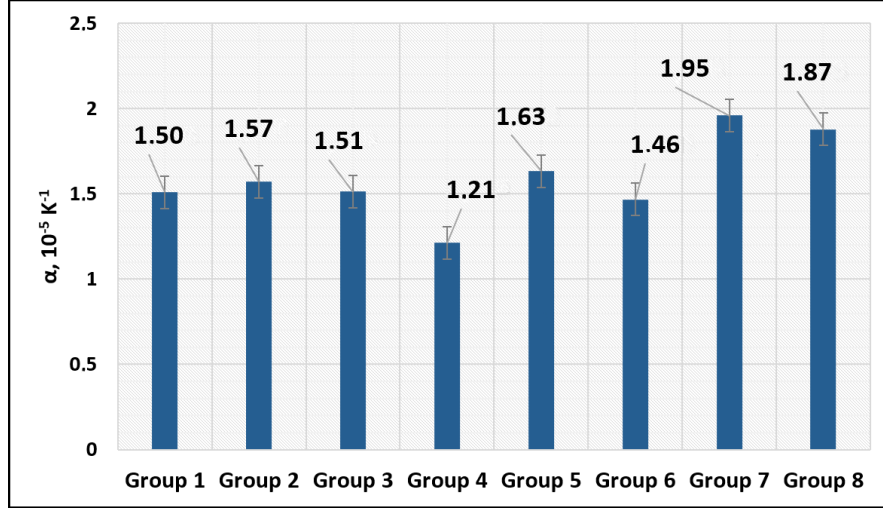


**Figure 33.** CLTE of groups 1–8 in the range 21–220 °C (measured both in longitudinal and transverse directions).

### 6.2.2 Analytical Estimation of CLTE

A simple rule-of-mixtures Equation (52) [187,188] analytically estimated the 1<sup>st</sup>-approximation-dependence between CLTE and concentration of bronze and steel in the alloy:

$$\alpha_{Br-SS} = \sum_i \alpha_i \cdot V_i = \frac{N_{Br}}{N} \cdot \alpha_{Br} + \frac{N_{SS}}{N} \cdot \alpha_{SS}, \quad (52)$$

where  $V_i$  denoted a volume fraction of each binary alloy component;  $N_{Br}$ , % was a wt. percentage of the bronze,  $N_{SS}$  – of SS,  $N = 100\%$ ,  $\alpha_{Br}$  and  $\alpha_{SS}$  were the CLTE of CP bronze and CP SS, respectively. This formula did not account for the appearance of new phases following 3D printing, which had CLTE that was different from the initial materials. It also did not consider a variation in the porosity in the parts. These parameters, if necessary, can be taken into account for more precise calculations.

In the temperature range of 0–100 °C,  $\alpha_{ss} \cong 1.60 \cdot 10^{-5} \text{ K}^{-1}$  [189];  $\alpha_{Br}^{Al} \cong 1.68 \cdot 10^{-5} \text{ K}^{-1}$  [189] (aluminum bronze);  $\alpha_{Br}^{Cr} \cong 1.65 \cdot 10^{-5} \text{ K}^{-1}$  [189] (chromium bronze);  $\alpha_{Br}^{Sn} \cong 1.80 \cdot 10^{-5} \text{ K}^{-1}$  [190] (tin bronze). Here,  $\alpha_{ss}$ ,  $\alpha_{Br}^{Sn}$ ,  $\alpha_{Br}^{Al}$ , and  $\alpha_{Br}^{Cr}$  were relevant to these materials created via traditional manufacturing methods. The analytical estimation method for the 3D-printed material is provided below. The calculations considered that CLTE in the whole range from 21 °C to 220 °C did not depend on the temperature. In general, this dependence existed and had a substantially complex form. Each binary intermetallic compound of the laser-deposited alloy could be expressed as a sum of  $\alpha_{lat} + \alpha_{el} + \alpha_{mag}$  [191], and  $\alpha_{lat} \sim T^3$  was a lattice contribution.  $\alpha_{lat}$  could be described in terms of the Debye theory. It became temperature independent at a level approximately above the Debye temperature.  $\alpha_{el} \sim T$  was an electronic contribution.  $\alpha_{mag}$  was a magnetic contribution.  $\alpha_{mag}$  was temperature-independent in the paramagnetic range and tended to zero above the Curie temperature.

For 50/50 alloys (groups 1–3)  $N_{Br} = N_{SS} = 50 \text{ wt.}\%$ ; for 75/25 alloys (groups 4–6)  $N_{Br} \cong 75 \text{ wt.}\%$ ;  $N_{SS} \cong 25 \text{ wt.}\%$ . In the case of alternating layer gradient structures (groups 7–8), CLTE was also gradient. The dependence between  $\alpha$  and the vertical coordinate  $z$ ,  $\mu\text{m}$  was defined using the modified form of the rule of mixture [188,192]:

$$\alpha(z) = V(z) \cdot \alpha_1 + (1 - V(z)) \cdot \alpha_2, \quad (53)$$

where  $V(z)$  was a volume fraction of constituents (SS, bronze), which obeyed a piecewise-defined function (54) [23]:

$$V(z) = \begin{cases} 1, & \text{if } 500 \cdot n < z < 250 \cdot (2 \cdot n + 1), \\ 0, & \text{if } 250 \cdot (2 \cdot n + 1) < z < 500 \cdot (n + 1), \\ n = 0, 1, 2, 3, \dots, 149. \end{cases} \quad (54)$$

Within the certain neighborhoods of the irregular points  $z = 250 \cdot n$ , the behavior of the function depended on the phase composition at the interface areas between steel and bronze. Most of all, it depended on the formation of intermetallic phases. If the shrinkage caused by the permeation of each sequential layer into the previous one and their partial intermixing were also considered, the  $V(z)$  equation would take on a more complicated form. However, the volume-mean average CLTE of FGMs in groups 7 and 8 could still be estimated using equation (52) under the assumption of  $N_{Br} = N_{SS} = 50\%$  (same as for groups 1–3).

Table 10 demonstrates estimated values of CLTE for all groups based on the CLTE of pure metals fabricated via traditional methods.

**Table 10.** Analytically estimated CLTE of all groups based on the CLTE of pure metals.

Group №	1	2	3	4	5	6	7	8
CLTE, $K^{-1} \times 10^{-5}$	1.65	1.63	1.70	1.66	1.64	1.75	1.64 <sup>1</sup>	1.63 <sup>1</sup>

<sup>1</sup> A weight-mean average.

Parts of groups 4 and 6 had the lowest experimental CLTE. Both of them had the highest bronze percentage (75%). Within these two groups, a non-gradient alloy based on aluminum bronze and SS in the ratio of 75/25 wt.% (group 4) had the lowest CLTE:  $(1.21 \pm \pm 0.10) \cdot 10^{-5} K^{-1}$ . It indicated that this material had the best resistance to linear thermal deformation under the influence of high temperatures. Part of group №5 (Cr bronze + SS 316L) also had the same bronze percentage (75%). Still, it did not show such a low CLTE. The reason for it might be the formation of additional Fe-Cr phases in this alloy, and the absence of Fe-Zn, Fe-Sn, and Fe-Al.

All groups created via the alternating layers' technique (№№ 7–8) had the highest CLTE ( $[(1.88–1.96) \pm 0.10] \cdot 10^{-5} \text{ K}^{-1}$ ). It meant that they suffered the highest deformations at high temperatures. It was considered an undesirable property in many practical applications. Groups with a 50/50 steel-to-bronze ratio (№№ 1–3) had intermediate (and approximately similar) CLTE, from  $(1.51 \pm 0.10) \cdot 10^{-5}$  to  $(1.58 \pm 0.10) \cdot 10^{-5} \text{ K}^{-1}$ .

It was known that there was a difference between the CLTEs on the basis of a manufacturing method (traditional technologies *vs.* AM). It was provided by chemical, phase, and structural composition distinctions. The resulting CLTE was compared with the characteristics of CP materials created via traditional methods. The experimental results were: for SS 316L  $\alpha \cong (1.65–1.75) \times 10^{-5} \text{ K}^{-1}$ ; for tin bronze:  $(1.85–1.92) \times 10^{-5} \text{ K}^{-1}$ ; for aluminum bronze:  $(1.62–1.70) \times 10^{-5} \text{ K}^{-1}$ ; for chromium bronze:  $(1.64–1.70) \times 10^{-5} \text{ K}^{-1}$ . Table 10 displays theoretically estimated results. It was seen that the experimental values were lower in the case of groups 1–6 (50/50 wt.% and 75/25 wt.% alloys) and higher in the case of groups 7–8 (gradient materials). Additionally, it was seen that the CLTE of groups 1–2 significantly differed from groups 7–8. Still, according to Equation (52), they were expected to be equal to each other. Epitaxial growth and the formation of new phases, i.e., intermetallics (see [118] and [226]) in the interface areas between different metals, are primarily responsible for this phenomenon. These intermetallics might have thermal characteristics (i.e., CLTE) different from the pure initial materials — steel and bronze.

### 6.2.3 Numerical Analysis of the Dependence between Thermal Expansion, Temperature, and Laser Treatment Parameters

Minitab software (Minitab Ltd., Coventry, UK) was used for the analysis of the dependence between CLTE and temperature. Parameters of PC: CPU—Intel® Core™ i7-7700HQ 2.81 GHz. RAM: 16,0 GB. OS: Windows x64. M. Yakout et al. [186] previously discussed the dependence between the CLTE, temperature, and parameters of the laser treatment regarding the pure 3D-printed SS 316L. The authors developed a three-way interaction regression model using the Minitab and applied it to the SLM. This model provided accurate results for the DED process, too. According to it, the relative thermal expansion  $\varepsilon_T$  for  $T \leq 552$  K [186] was calculated for SS 316L using the following equations (55)–(58):

$$\varepsilon_T = a \cdot T^2 + b \cdot T + c; \quad (55)$$

$$a = 0.009714 \left[ \frac{1}{K^2} \right]; \quad (56)$$

$$b = 16.954 \left[ \frac{1}{K} \right] - 0.00577 \cdot P \left[ \frac{1}{K \cdot W} \right] - 14.98 \cdot h \left[ \frac{1}{K \cdot m} \right] + 0.0599 \cdot P \cdot h \left[ \frac{1}{K \cdot m \cdot W} \right]; \quad (57)$$

$$\begin{aligned} c = & 452 - 3.557 \cdot P \left[ \frac{1}{W} \right] - 1.350 \cdot v \left[ \frac{s}{m} \right] - 6925 \cdot h \left[ \frac{1}{m} \right] - 0.001838 \cdot P^2 \left[ \frac{1}{W^2} \right] \\ & - 10\,399 \times h^2 \left[ \frac{1}{m^2} \right] + 0.05893 \cdot P \cdot v \left[ \frac{s}{W \cdot m} \right] + \\ & + 40.28 \cdot P \cdot h \left[ \frac{1}{W \cdot m} \right] + 11.47 \cdot v \cdot h \left[ \frac{s}{m^2} \right] - 0.05238 \cdot P \cdot v \cdot h \left[ \frac{s}{W \cdot m^2} \right] \end{aligned} \quad (58)$$

Here,  $P$ ,  $v$ , and  $h$  were processing parameters.  $P$  was laser power, W;  $v$  was scanning speed, mm/s;  $h$  was hatch spacing, mm. In our case,  $h = 0.3$  mm,  $P_{average} = 308$  W, and  $v = 0.85$  m/min  $\cong 16.67$  mm/s.  $P$ ,  $v$ , and  $h$  were independent variables,  $P^2$ ,  $v^2$ , and  $h^2$  were two-way interactions,  $T$  and  $T^2$  were the temperature variables, and  $P \cdot T$ ,  $v \cdot T$ ,  $h \cdot T$ ,

$P \cdot v \cdot T$ ,  $P \cdot h \cdot T$  were the interaction terms. According to [186], this model was accepted as statistically significant and had a standard deviation of  $S = 9.64627$ , coefficient of determination  $R^2=99.99\%$ , and the predicted residual error sum of squares PRESS = 11785.3.

Equations (59) and (60) could be used to calculate CLTE from relative thermal expansion  $\varepsilon_T$ :

$$\alpha(T) = \frac{1}{L} \cdot \frac{dL}{dT}, \quad (59)$$

$$d\varepsilon_T = \frac{dL}{L}. \quad (60)$$

The resulting expression (61) provided the desired relation between CLTE and temperature:

$$\alpha(T) = \frac{d\varepsilon_T}{dT}. \quad (61)$$

Calculations based on the three-way interaction regression model gave the following results for SS 316L:  $b = 16.217600 \text{ K}^{-1}$ ,  $c \cong -125.021612$ , and  $\varepsilon_T = 0.009714 \cdot T^2 + 16.217600 \cdot T - 125.021612$ . They provided values of  $\varepsilon_T$  of SS 316L at specific temperature points, particularly,  $\varepsilon_T \cong 2.20 \cdot 10^{-4}$  at room temperature (294 K),  $\varepsilon_T \cong 3.91 \cdot 10^{-3}$  at 493 K,  $\varepsilon_T \cong 1.32 \cdot 10^{-3}$  at 358 K, and  $\varepsilon_T \cong 3.77 \cdot 10^{-3}$  at 486 K.

The resulting dependence  $\alpha(T)$  derived from equation (61) was as follows:

$$\alpha(T) = (2 \cdot a \cdot T + b) \cdot 10^{-6}. \quad (62)$$

It was valid for  $T \leq 552 \text{ K}$ . From (62), the CLTE of SS 316L at 358 K was  $1.787 \cdot 10^{-5} \text{ K}^{-1}$ ; CLTE at 486 K –  $2.036 \cdot 10^{-5} \text{ K}^{-1}$ .

The results provided by the three-way interaction regression model for SS 316L were close to the results given by SLM at the critical laser energy density in the study [186]. This study reported about  $\varepsilon_T \cong 3.90 \cdot 10^{-3}$  at 493 K. Our results were also higher than thermal expansion for SLM at the same laser power and scanning speed but lower hatch spacing ( $h = 120 \mu\text{m}$ ,  $\varepsilon_T \cong \{3.10\text{--}3.20\} \cdot 10^{-3}$  [186]). The CLTE of SS 316L also correlated well with the dilatometer experimental results of [123] (in that study, the measured CLTE of SS 316L was approximately  $\{1.7\text{--}2.0\} \cdot 10^{-5} \text{ K}^{-1}$  in the range 373–573 K).

### **6.3 Heat Capacity of SS 316L – Bronze FGMs and Its Correlation with CLTE**

Netzsch DSC 214 Polyma (NETZSCH Group, Selb, Bavaria, Germany) measured the specific heat capacity of fabricated materials (8 groups + CP SS 316L). They were prepared as metal shavings and pressurized with a load rate of  $700 \text{ kg} \times \text{s}$ . A single metal «tablet» had 25 mg mass and 4 mm diameter. The mass of the specimens did not change after the experiments. Each tablet was heated from 40 °C to 300 °C at a speed of 10 °C/min. The measuring chamber was purged by nitrogen. Aluminum pans were used for the experiments. The precision of heat capacity measurements according to the instrument's datasheet was  $\pm 2.5\%$ .

Figure 34a shows the experimental dependencies between specific heat capacity and temperature measured during a heating cycle, and Figure 34b – during a cooling cycle. All dotted curves showed 50/50 wt.% alloys. All solid curves showed 75/25 wt.% alloys. All dashed curves showed alternating-layers gradient alloys. Bright black curves showed C61800-based alloys. Pale orange curves showed C18400-based alloys. Blue curves of medium brightness showed CB480K-based alloys. Measurement precision was  $\pm 2.5\%$ .

Figure 35 demonstrates the specific heat capacity of CP SS 316L measured over two heating and two cooling cycles. Blue and light-blue curves refer to heating cycles, and green and orange refer to cooling. All the cycles were conducted sequentially in the order as follows: heating cycle №1, cooling cycle №1, heating cycle №2, and cooling cycle №2. Delay between cooling cycle №1 and heating cycle №2 was more than 12 h.

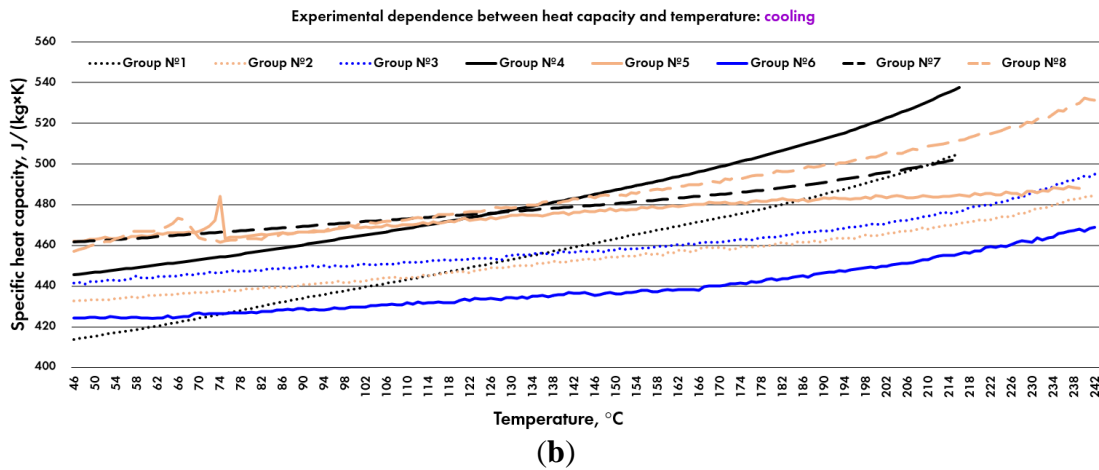
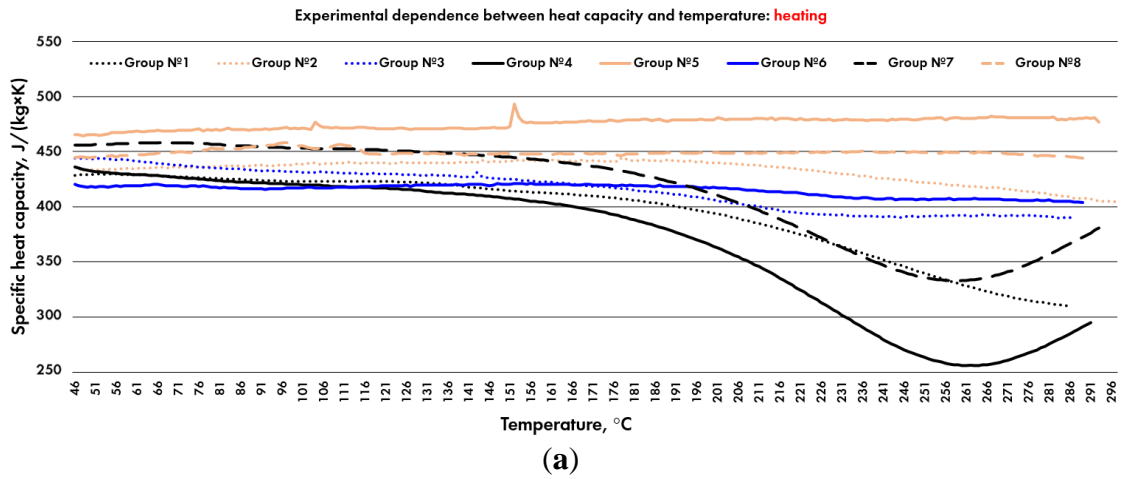
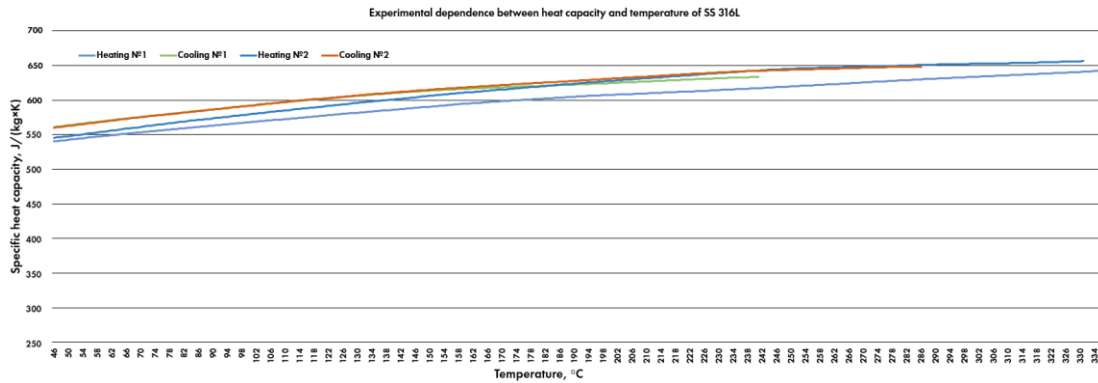


Figure 34 – DSC curves of materials from groups 1-8.



**Figure 35** – DSC curves of CP SS 316L measured during 4 cycles (measurement precision was  $\pm 2.5\%$ ).

Figure 34a demonstrates the unusual behavior of specific heat capacity. Most of the time (groups 1-4, 7, and — unclearly — group 6), it decreased as the temperature rose. Because precise mass measurements proved that there was no mass loss during the experiments, the reason for such behavior could be long-term phase transitions, which started in the range 46–136 °C. The end of these phase transitions was a local extremum of specific heat capacity near 254–266 °C in the case of groups 4 and 7. Both of them were C61800-based. The third C61800-based group (№1) had a similar shape but its expected local extremum was outside the temperature range investigated (46–286 °C). It is needed to check the existence of this extremum during subsequent research. We associated these transitions with the formation of lower bainite after the decay of previously undercooled austenite. Because of high cooling rates during DED, the liquid phase was undercooled below the metastable miscibility gap [121], and undercooled austenitic  $\gamma$ -Fe appeared. The existence of  $\gamma$ -Fe in these C61800-SS 316L alloys was proved in Chapter 4 by the results of XRD analysis. During reheating under DSC analysis, undercooled austenite decayed within approximately the 200–300 °C range, and lower bainite appeared. After this phase

transition, the specific heat capacity began to increase with temperature. It should be noted that these transitions were observed only in the C61800-based alloys, which showed a {paramagnetic FCC} → {ferromagnetic BCC} transformation [194]. This transformation provided the fabrication of soft magnetic materials from paramagnetic components [194]. C18400- and CB480K-based alloys demonstrated neither this FCC→BCC transformation nor an evident specific capacity decrease.

Only groups 5 and 8 based on C18400 did not have the mentioned heat capacity decrease. Because another C18400-based group (group 2) had this decrease, it could be suggested that there was a transient concentration of elements in the alloy, which provoked the phase transition. Nevertheless, today's literature did not report on the transient behavior of the Cu-Fe-Cr system in the low-temperature area [195-198]. Therefore, the reason for such an effect is not clear and needs to be studied in more detail.

It was seen that C61800-based curves had the lowest average value of specific heat capacity. C18400-based curves had the highest value, CB480K—intermediate. The experimental curve of group №5 had two small exothermic peaks: the first one — near 102–106 °C, the second one — near 154–158 °C. They could be associated with polymorphic transformations [199-201], which appeared during heating. They changed the crystalline structure, its characteristic dimensions, and its shape. Another C18400-based group (№8) also showed very small exothermic peaks in the area between 78 and 118 °C. CB480K-based group №3 had a small exothermic peak near 144 °C.

Figure 34b demonstrates another behavior of specific heat capacity. All the curves were monotonous. It pointed to the absence of long-term phase transitions, which were

observed during the heating cycle. Nevertheless, two C18400-based groups (№5 and №8) had clearly observable exothermic peaks near 66 °C and 74 °C. These two curves also had exothermic peaks during a heating cycle, but the corresponding temperature values were different.

A comparison of the obtained results of SS 316L specific heat capacity with DSC data of other studies [125,202-206] showed that SS 316L had 15–20%-higher heat capacity if it was fabricated by DED in comparison to traditional methods. Its reason could be rapid solidification, which leads to grain refinement and the changing of the thermal properties of the material.

DSC curves of the specific heat capacity of CP SS 316L did not show phase transitions in the range of 50–330 °C. It pointed at the absence of undercooled austenite and the formation of lower bainite. It was expected in the presence of bronze only. Earlier studies [125,202-206] also did not display phase transitions of SS 316L in this temperature range.

#### **6.4 Interim Conclusion**

This part of the research investigated CLTE and the specific heat capacity of Al/Cr/Sn-bronze and SS-316L binary alloys (50/50 and 75/25 wt.%) and FGMs fabricated via DED were investigated. These thermal characteristics of such structures were experimentally studied for the first time and compared with theoretically predicted values.

The lowest CLTE was shown by the 75/25 wt.% Al-bronze-based alloy:  $(1.212 \pm \pm 0.095) \cdot 10^{-5} \text{ K}^{-1}$ . This material was characterized by the best resistance to thermal deformations under high-temperature influence.

According to the numerical model, the relative thermal expansion  $\varepsilon_T$  of the DED-fabricated SS 316L ( $\varepsilon_T \cong 3.91 \cdot 10^{-3}$  at 493 K) was close to the results predicted for SLM. It also matched the dilatometer experimental results of SLM-fabricated SS 316L. Decreased hatch spacing was considered a reliable method of changing the CLTE of Fe-Cu parts fabricated by AM methods.

The specific heat capacity of the DED-fabricated Fe-Cu alloys demonstrated uncommon behavior during the heating cycle. A decreased specific heat capacity and its subsequent increase after  $\sim 260$  °C in the Cu-Fe-Al system were associated with long-term phase transitions and the formation of lower bainite. The small exothermic peaks in the DSC curves of Cu-Fe-Cr alloys were attributed to rapid polymorphic transformations. The specific heat capacity of DED-fabricated CP SS 316L was 15–20% higher than traditional methods. Its reason was rapid solidification, which led to grain refinement and changed the material's thermal properties.

These findings can be applied to the DED of Fe-Cu system homogeneous alloys and FGMs (primarily based on UNS C61800 and SS 316L), which can be used in the NPP, STP, aerospace, and electronic components industries. The future direction of the study in this field may include:

1. The analysis of the specific heat capacity of the Fe-Cu materials in a broader temperature range (up to  $\sim 900$  °C);
2. The study of the phase transitions of the Cu-Fe-Cr system in the low-temperature area.

## Chapter 7. Summary and Conclusion

The study successfully demonstrated the possibility of joining dissimilar immiscible materials in the Fe-Cu system via direct energy deposition. The microstructural, mechanical, and thermal properties of the laser-deposited Fe-Cu FGMs and quasi-homogeneous materials were successfully investigated for the first time in such a measure. The difference in microstructural parameters caused by varying operation conditions, chemical composition, and deposition strategies led to significant scatter in the physical properties of the resulting alloys. The main findings of this study are described below.

- The potential transition zones and strategies for compositional grading between austenitic stainless steel and bronze were investigated. The gradient transitions and alternating layers between Fe-based and Cu-based sections of the gradient alloy lead to flawless fabrication and allow combining materials with rather different physical characteristics (including elasticity modulus, CLTE, laser radiation absorption coefficient). These approaches also allowed printing tension coupons with respectable strain levels in these FGMs. The resulting mechanical properties of UTS and strain to fracture appear decent, indicative of a fully dense build.

- The microstructural characteristics strongly influence on the mechanical properties of DED-fabricated Fe-Cu materials (including FGMs). The optical microscopy was used for the microstructural analysis, and the tensile behavior was correlated with microstructural features and printing parameters. In particular, the mechanisms of increasing mechanical strength of SS 316L – Al bronze quasi-homogeneous structures and FGMs by varying microstructural parameters were revealed. They included increasing the

fraction of  $\delta$ -ferrite, raising the amount of  $\text{Cr}_2\text{O}_3$  and  $\text{MnO}$  precipitations, and reducing the dimensions of dendrites leading to grain refinement. The discussion of phases was supplemented with the results of the XRD phase analysis technique. The DIC method showed the alternating character of principal strain distribution in the gradient specimens and revealed significant strain concentrators caused by microstructural defects in specimens. Several surface defects were observed and linked to internal defects, which have influence on mechanical properties of the resulting parts as well as grain size, compositional changes, and other microstructural parameters. Fracture surfaces' cross-sections provided extra information on deformation/failure mechanisms, showed the predominantly brittle character of failure, and revealed the distribution of porosity inside the tension coupons.

- 50/50 wt.% Fe-Cu quasi-homogeneous materials based on Al bronze and SS 316L are the most prospective for practical applications, which are associated with prominent external loads and extreme heat conditions, compared to Cr-bronze-based and Sn-bronze-based quasi-homogeneous and sandwich structures. In specific, they exhibited great UTS (838.6 MPa), yield stress (665 MPa), modulus of resilience ( $1.03 \text{ MJ/m}^3$ ), strain-to-fracture (0.035), and low CLTE ( $1.212 \times 10^{-5} \text{ K}^{-1}$ ). The significance of these results was essentially approved by the comparison to the literature data.

- The thermal properties (including CLTE and specific heat capacity) of the immiscible DEDed materials of the Fe-Cu system were also substantially studied for the first time. The specific heat capacity of the DED-fabricated Fe-Cu alloys demonstrated the uncommon behavior during the heating cycle in the range from  $45 \text{ }^\circ\text{C}$  to  $300 \text{ }^\circ\text{C}$ . It presented

long-term phase transitions and small exothermic peaks in the DSC curves of Fe-Cu-Cr alloys attributed to the formation of lower bainite and rapid polymorphic transformations.

The results of the conducted research can be applied in the aerospace, electronics, NPP, STP, milling, tooling, medicine, defense, and electronic industries. The findings have a significant importance for achieving porosity-free transition zones with no or small volume fraction of brittle phases for compositionally graded materials and fabricating structures with dissimilar materials.

## Chapter 8. Future Research Direction

This thesis research describes the mechanical and thermal characteristics, which are the most important in the light of practical applications of Fe-Cu DED-fabricated heterogeneous materials, and find the correlation between them and the microstructural phenomena of these materials. However, a lot of significant aspects were left without a proper discussion in this work. Some of them were not within the front of interest because they didn't comply the overall vector of this study; some – were not investigated in a sufficient measure. Nevertheless, the author finds necessary to additionally describe three subtopics in the last «outlook» section of the thesis:

- magnetic properties and induced magnetic response of Fe-Cu energy-deposited parts, which are interesting because of detected magnetic induction of material fabricated from non-magnetic constituents and due to the overall wide area of applications of the soft magnetic 3D printed materials;
- ultrasonic-assisted DED of heterogeneous Fe-Cu materials, which allows a removal of many defects of these alloys and provides an improvement of their microstructural and mechanical characteristics as it was stated in the text of this thesis many times over;
- DED of a real FG part from materials of Fe-Cu system, which gives the best approval of the relevance of the gained results and appropriability of the elaborated technological methods, combinations of materials, operation conditions, and deposition schemes.

These subtopics were described for two purposes: the first one – to emphasize future directions of the research; the second – to describe what was already done in this field. The findings about magnetic properties of SS 316L – bronze FGMs were presented in 2021 the ASTM International Conference on Additive Manufacturing (ASTM ICAM 2021). The ultrasonic-assisted-DEDed materials were described in 2022 in the chapter «Direct Energy Deposition of Cu-Fe System Functionally Graded Materials – Miscibility Aspects, Cracking Sources, and Methods of Assisted Manufacturing» of the book «Advanced Additive Manufacturing» ([doi.org/10.5772/intechopen.102562](https://doi.org/10.5772/intechopen.102562)). The real FG Fe-Cu part was designed and printed from SS 316L and three kinds of bronze in the Additive Manufacturing Lab of Skoltech in 2023.

### **8.1 Magnetic Properties of SS 316L – Bronze FGMs**

The third block of physical characteristics' research of Fe-Cu FGMs and quasi-homogeneous structures has to include the study of their magnetic properties. This topic is interesting due to prospective applications of the magnetic hard and soft DEDed materials discussed below. As it was found during experiments, aluminium bronze – SS specimens gain magnetic properties after printing while they didn't have them before it. This subject needs to be studied in more detail. The area of practical application of ferromagnetic 3D-printed components is quite large. It includes manufacturing of the transformer cores, components of turbine engines, electric generators, elements of unmanned aircrafts, microwave absorbing materials, high performance motors, etc. [207-211]. Industrially used materials with ferromagnetic properties could be formally divided into the two broad groups – magnetic hard and magnetic soft materials. Magnetic soft materials are

characterized by the high magnetic permeability, high saturation magnetization and low coercivity, providing their simple magnetization and demagnetization [211], which makes them appropriate for using as parts of various equipment ranging from the power transformers to novel sensors and actuators [212]. Magnetic hard materials, contrarily, have a high coercivity and are commonly used in electrical machines and vehicles, elevators, TVs and phones, wind turbines, and so on [211]. Hard magnetic materials could be also used in combination with soft magnetic ones in many of electrical machines applications [213].

The attractive possibilities of hard and soft magnetic materials fabrication by the AM techniques are followed by the certain difficulties. A lot of efforts are to be focused on the process optimization leading to acquisition of superior magnetic properties of the resulted alloys [211]. Beyond that, the DED of ferromagnetic hard and soft components is often associated with using of ferromagnetic consumable materials. However, the utilization of ferromagnetic metal powders in the DED may lead to clogging a powder feeding system on some machines due to magnetization of this system and/or metal parts magnetization by the powder [214]. Some 3D-printing techniques also require demagnetization of a build substrate and metal parts inside a build chamber to avoid uneven ferromagnetic powder layering. An in-situ fabrication of ferromagnetic parts from paramagnetic powders, such as SS 316L and Al, is a potential way to address these issues. Therefore, the main purpose of the current research is a study of dependence between elemental concentration of Al in a binary alloy and its resulted saturation magnetization after the DED, and relationship between magnetic and microhardness properties.

It is known that the ultrasonic-assisted DED process has a strong influence on parameters of resulted parts: it refines the grain structure, increases wear resistivity and microhardness, tensile strength and elasticity modulus, improves a fracture toughness, and has a possibility to dispose cracking [216-220,231]. Hence, this technology has a significant importance for manufacturing of FGMs, including graded soft magnetic alloys (Fe-Si, Fe-Al, Fe-Cu, Fe-Co, Fe-Ni,  $\text{AlCo}_{1-x}\text{Cr}_x\text{FeNi}$  and  $\text{Al}_x\text{CrCuFeNi}$  high entropy alloys, Ni-Mn-Ga magnetic shape memory alloys, etc) [211]. Nevertheless, the poor amount of data related to the influence of ultrasonic assistance on the magnetic properties of DED-fabricated parts could be found. This part of the current study is aimed, among other things, to investigation of this problem particularly in case of Fe-Cu system materials. This system has prospective applications for the soft magnetic parts producing because of local magnetic properties (high values of the local magnetic moment and contact hyperfine magnetic field) in BCC Fe-Cu lattice phase [221] along with precipitation of ferromagnetic Fe-Al phases, if the aluminium bronze is applied [214].

In this research, two binary systems were studied: Fe-Cu and Fe-Al. Three powder materials were applied: SS 316L (fraction 50-150  $\mu\text{m}$ ), aluminium bronze similar to UNS C61800 (fraction 45-125  $\mu\text{m}$ ), and CP aluminium powder (fraction 75-175  $\mu\text{m}$ ). Chemical composition of SS 316L is given in [118] as it was mentioned before. Chemical composition of aluminium bronze was the same as that in chapter 4. The SS powder was manufactured in Höganäs Belgium SA, aluminium bronze – in joint stock company Polema (Tula, Russia), CP aluminium – in «Volgograd aluminium company powder metallurgy» Ltd (Volgograd, Russia).

Totally 5 groups of specimens (Table 11), consisted of 4 different mixtures of stainless steel and aluminium, taken at various ratios, and one aluminium bronze – SS binary alloy, were manufactured for the research of their magnetic properties and microhardness characteristics. All specimens were fabricated the same technological installation as discussed before. The values of the output laser radiation power for each group of specimens are listed in Table 12. All other operation conditions were listed in Chapter 4.

**Table 11** – Experimental groups of laser deposited Fe-Al and Fe-Cu specimens.

Material	Group 1	Group 2	Group 3	Group 4	Group 5
SS 316L, wt. %	80	90	95	97	50
Al, wt. %	20	10	5	3	–
Al bronze, wt. %	–	–	–	–	50

**Table 12** – Values of output laser power of all groups.

Parameter	Group 1	Group 2	Group 3	Group 4	Group 5
Laser power, W	120	150	250	320	300...450*

\* Specimens of group 5 were fabricated using a direct tooling mode [6,118].

Specimens for optical microscopy were prepared by the same technique as it was discussed in Chapter 4. The magnetization was measured via the vibrating-coil magnetometer LakeShore 7410 [222].

The examples of specimens, fabricated from SS 316L and CP Al for the specific magnetization analysis, are shown in Figure 36.

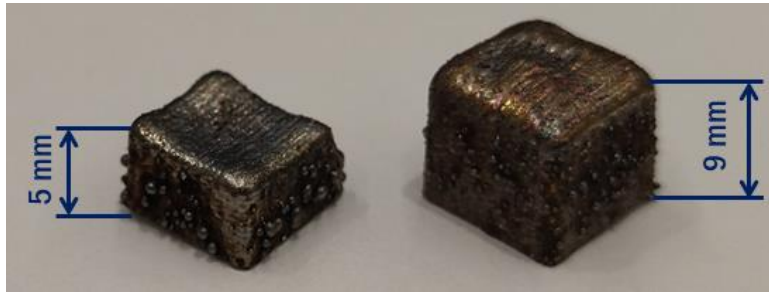


**Figure 36** – As-deposited specimens of the Fe-Al system.

The left specimen (consisted of 1% Al and 99% SS) and right specimen (2% Al and 98% SS) show the similar defect – a high surface roughness, which could be associated with spatter [223], surface deformation due to concentrated high heat input, or excessive hatch spacing [74]. Another authors [225], contrarily, associate such high roughness with low heat input along with large size of powder particles and excrescent scanning speed. The next type of defect is, contrariwise, different for both specimens shown in Figure 36: it is blobs and zits of the left specimen, which could be attributed to the extra deposited material at the start/end points of the concrete layer and inappropriate dwell time, and lowering of the edges of the right specimen that could occur because of an unsuitable nozzle path and discontinuity of the powder deposition [74].

Figure 37 demonstrates the representative examples of the Fe-Al system microstructural patterns taken at different magnifications.

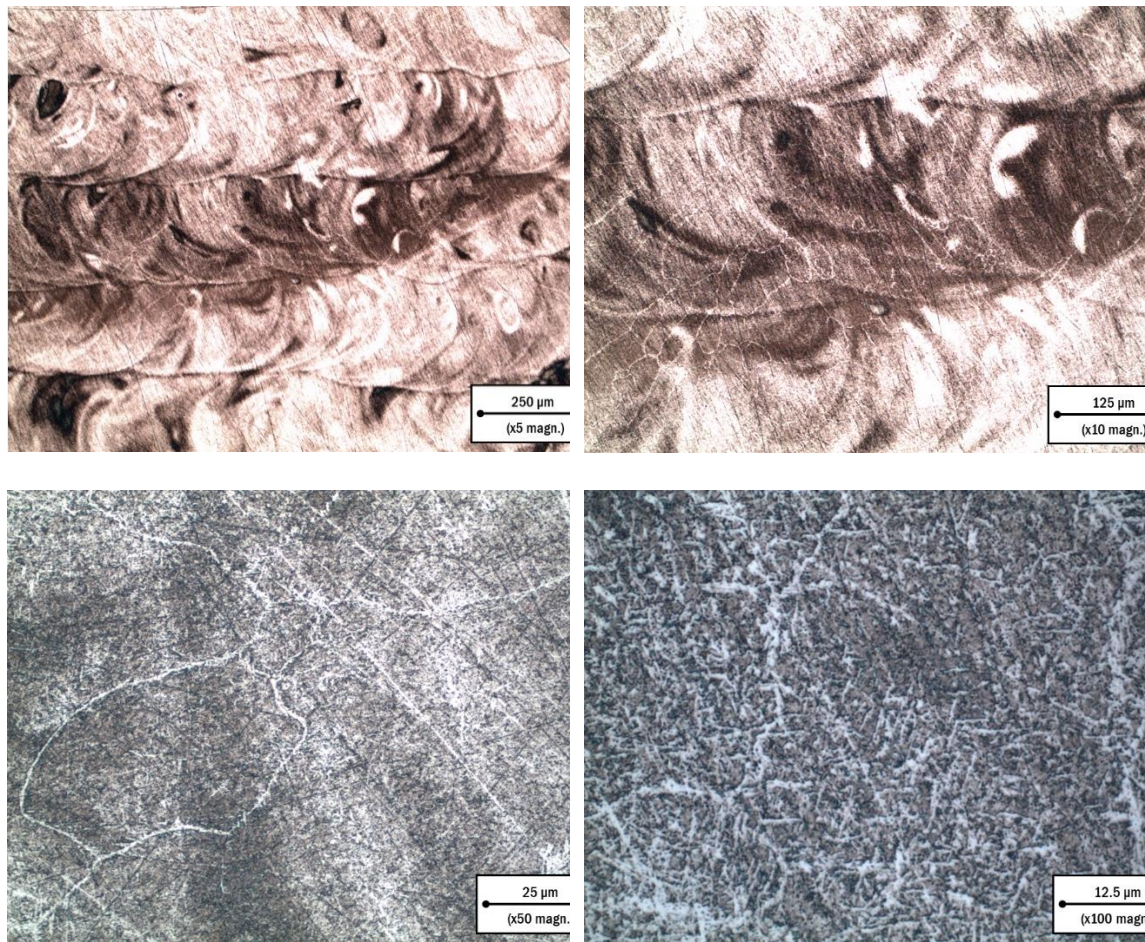


**Figure 37** – Microstructure images of the Fe-Al specimens fabricated via the DED.

The left-top picture of Figure 37 evidently demonstrates a pattern of oppositely directed horizontal tracks, deposited within a single layer of a specimen. The picture with a higher magnification (right-top) allows seeing a thin white network running through the inspected surface. This network could be explained as Al-based precipitates along the boundaries of Fe-based intermetallic grains. The left bottom picture taken at x50 magnification demonstrates the mentioned network more clearly, and the right bottom picture with the highest magnification (x100) shows a fine needle-shaped microstructure. These needle-shaped phases have the same view as the  $\theta$ - $\text{Al}_{13}\text{Fe}_4$ , presented in the study

[226] that was also devoted to characterization of AM-fabricated Fe-Al binary alloy. Neither cracking nor huge porosity in the fabricated specimens were observed during the optical microstructure analysis.

Results of measurement of the specific magnetization of all experimental groups are provided in Figure 38. There the black curve (3%) is associated with Al (3%) – SS 316L (97%) alloy; red (5%) – with Al (5%) – SS 316L (95%); green (10%) – with Al (10%) – SS 316L (90%); blue (20%) – with Al (20%) – SS 316L (80%); turquoise – with aluminium bronze (50%) – SS 316L (50%), fabricated via the ultrasonic-assisted DED. Among other groups, a binary Fe-Al alloy of group 3 demonstrated the highest value of specific magnetization – 117 emu/g.

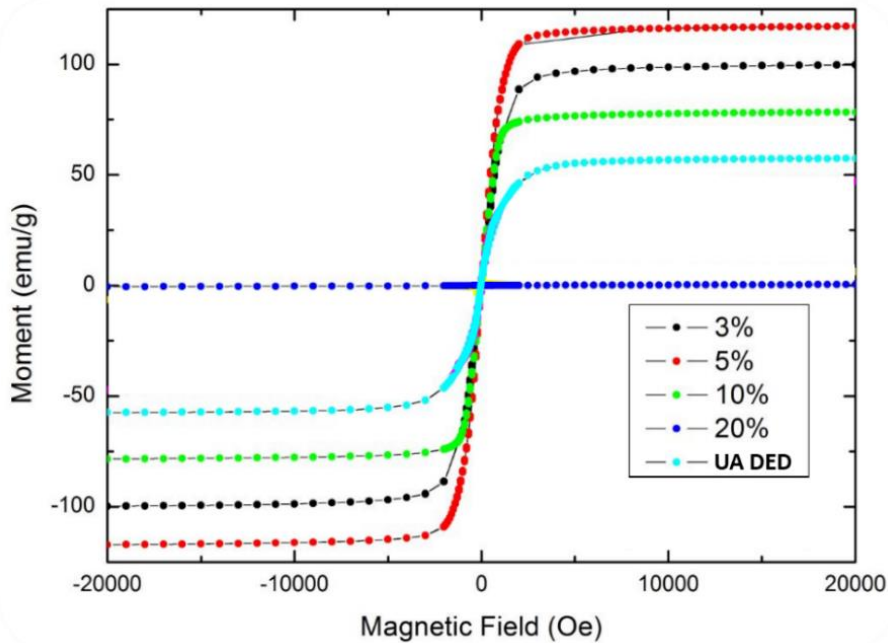


**Figure 38** – Saturation curves of laser deposited SS-Al and SS-bronze specimens at room temperature.

To estimate the measure of the resulted saturation magnetization, it is necessary to compare it with currently known values of that for different materials, produced using AM

and traditional techniques. For classical AM-fabricated soft magnetic materials, such as Fe-Co (Hiperco) alloys, this value approximately equals from 192 emu/g to 257 emu/g [227], which is 1.64–2.25 times more than 117 emu/g, attributed to Al (5%) – SS 316L (95%) alloy (Figure 38). Saturation magnetization of SLM-fabricated soft magnetic FeSiBCrC alloy was found to be about 162 emu/g [228], which was 1.38 times more than that of our specimens of group 3. The resulting value of saturation magnetization of SS 316L – aluminium bronze alloy fabricated by the ultrasonic-assisted DED is approximately equal to magnetization of the ferromagnetic  $\text{La}_{0.67}\text{Sr}_{0.33}\text{MnO}_3$  and  $\text{La}_{0.67}\text{Ca}_{0.33}\text{MnO}_3$  manganite nanotubes at 5 K and 12 kOe magnetic field: ~50 emu/g; the Al (3%) – SS 316L (97%) alloy magnetization (117 emu/g) is higher than the bulk expected magnetization values of mentioned nanotubes [229]. If we compare our results with SS + aluminium bronze specimens, analyzed in the study [214], we'll see that SS-Al specimens have approximately two times lower saturation magnetization – about 50 emu/g. This difference could be associated with another amount and type of ferromagnetic Fe-Al phases, precipitated in the DED-fabricated binary alloy.

The experimental dependence between aluminium percentage in the deposited Fe-Al alloys and their magnetic moments is shown in Figure 39.

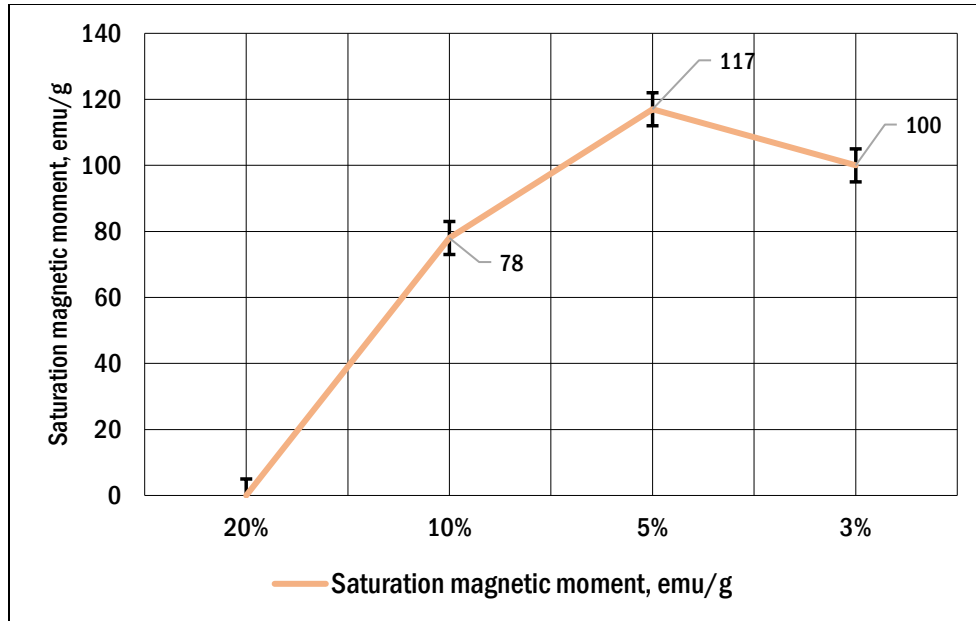


**Figure 39** – Saturation magnetization values for different concentrations of aluminium in the DED-fabricated SS 316L-Al alloy.

It is seen from the Figure 39 that the saturation magnetization increases from zero value attributed to 20% Al concentration to the maximum point of 5% (117 emu/g). After that, the value of magnetic moment decreases and amounts 100 emu/g for 3% Al fraction in the binary alloy. Precipitation of FeAl phase could be suggested as a reason of such magnetic properties' behavior.

It was seen that implementation of the ultrasonic assistance provided 16% increase of specific magnetization in case of aluminium bronze (50%) – SS 316L (50%) binary alloy fabricated at the same operation conditions in comparison to the study [214]. This difference could be explained as changing phase composition due to increase of a solidification rate influenced by the ultrasonic vibration effects. It was said earlier that Fe-Cu system is characterized by existence of a metastable liquid miscibility gap [7,101-103,136]: an increase of the solidification rate provides the more intensive undercooling of

a liquid phase followed by the liquid separation of immiscible Cu and Fe. Further coagulation and separated dendritic crystallization of the  $\gamma$ -Fe phase, which transforms to a ferromagnetic  $\alpha$ -Fe during further cooling, could be suggested as a factor of a slight increase of specific magnetization of a resulting Fe-Cu binary alloy.

Additionally, it should be mentioned that the presented study of Fe-Cu and Fe-Al DED-fabricated alloys magnetic properties could be significantly extended, when the area of extremely low temperatures will be also taken into consideration: the materials of these systems are expected to reveal micromagnetic properties [230] at temperatures near the absolute zero (about 5–10 K), and investigation of this phenomenon could appear as a prospective topic for the upgoing research. Another prospective topic in this field is the study of the thermal annealing influence on the magnetic properties of Fe-Cu and Fe-Al DED-fabricated parts.

The conducted experiments demonstrated a possibility of a soft-magnetic binary alloy fabrication from two different couples of initial paramagnetic components (SS + CP aluminium and SS + aluminium bronze) via the DED. The highest value of specific magnetization (117 emu/g) was observed in specimens with 19:1 steel-to-aluminium ratio. The magnetic properties lower when Al fraction deviates from 5%, and fully disappear when concentration of Al in SS equals 20%. The existence of the intermetallic ferromagnetic FeAl phase in the binary alloy could be responsible for this behavior.

The influence of the ultrasonic assistance on magnetic properties of DED-fabricated alloy was studied for the first time. It was shown that implementation of the ultrasonic vibration source during the DED provides a 16% increase of saturation

magnetization of Fe-Cu alloy, which could be associated with enhanced undercooling and liquid separation followed by precipitation of  $\gamma$ -Fe dendrites later transformed to the ferromagnetic  $\alpha$ -Fe phase.

This topic has to be continued with:

- Phase composition analysis of Fe-Al and Fe-Cu DED-fabricated alloys with a purpose to determine ferromagnetic phases responsible for varying magnetic properties of these materials depending on elemental concentrations in the initial powder mixtures.
- Research of the influence of thermal annealing on the magnetic properties of Fe-Cu gradient parts.
- Conducting X-ray fluorescence (XRF) and electron backscatter diffraction (EBSD) analyses of Fe-Cu and Fe-Al parts to analyze the nature of their induced magnetic properties in a deeper measure.
- Study of the micromagnetic properties of Fe-Cu gradient materials at temperatures near the absolute zero (about 5–10 K).

After finishing, the results of this section of the research will be practically implemented in the AM of soft-magnetic materials for electrical industry components, such as magnetic cores, rotors, magnetic amplifiers, shieldings, novel sensors and actuators.

## 8.2 Ultrasonic-assisted DED of SS 316L – Bronze FGMs

It was shown above that mechanical and other characteristics of Fe-Cu DED-fabricated alloys (including FGMs) strongly depend on its microstructure properties. One of the prospective techniques for improving the microstructure quality is the laser-assisted DED [231-238]. Our scheme of the ultrasonic-assisted DED is presented in Figure 40. The source of the ultrasonic frequency (~21 kHz) current signal (master oscillator in the scheme) was used for generation of the mechanical wave inside the magnetostrictor (magnetostrictive transducer – a device which converts an ultrasonic frequency alternating current energy to the mechanical energy of ultrasonic frequency vibration) located in the SS cooling reservoir. The wave was conducted to the waveguide, which was placed under the surface of substrate with a rigid fixation. In Figure 41, our practical implementation of this scheme (left picture) and the resulted microstructure (right picture) can be seen. Left picture, positions: 1 – the laser head; 2 – cooling vessel of the magnetostrictive transducer (see the description above); 3 – cameras; 4 – waveguide. Right picture: example of fine-grained intermixed microstructure of ultrasonic-assisted DED-fabricated part of 50% aluminium bronze with 9.5% Al and 1.0% Fe content (chemical composition similar to UNS C61800) and 50% SS 316L. Light areas: islands of stainless steel, dark areas: the copper-based regions. The ultrasonic frequency generator UZG-2M (isn't shown in picture) with 2 kW ultimate output power, 1.8–1.9 kW magnetostrictor PMS2-20 (pos. 2, placed in the Ø150x335 mm cylindrical stainless steel cooling vessel) with 21.5–22 kHz frequency range, and the titanium alloy waveguide (pos. 4) with rectangular base surface 120x18 mm were manufactured by OOO “Ultra-Rezonans” (Yekaterinburg, the Russian

Federation). Water at the room temperature was applied as a cooling liquid (2 L/min flow). The DED process was performed again using InssTek MX-1000 3D-printer (pos. 1) in a DMT [6,118] realized by two cameras (pos. 3). The methods of the microstructure preparing and imaging were the same as discussed in §3.1.

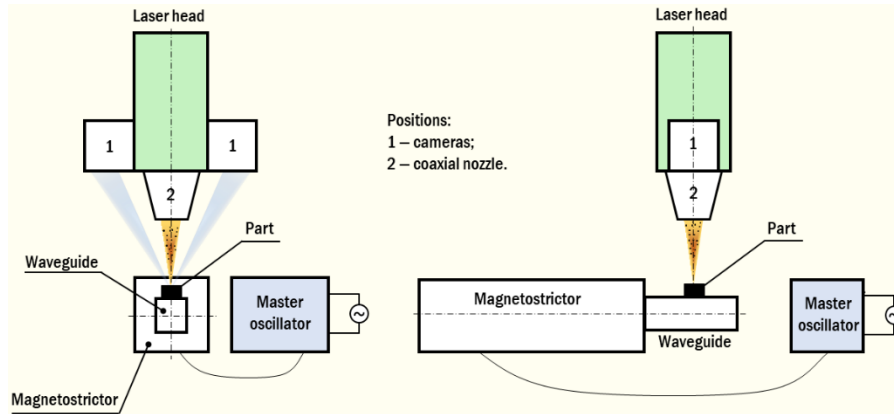


**Figure 40** – The ultrasonic-assisted DED process scheme.

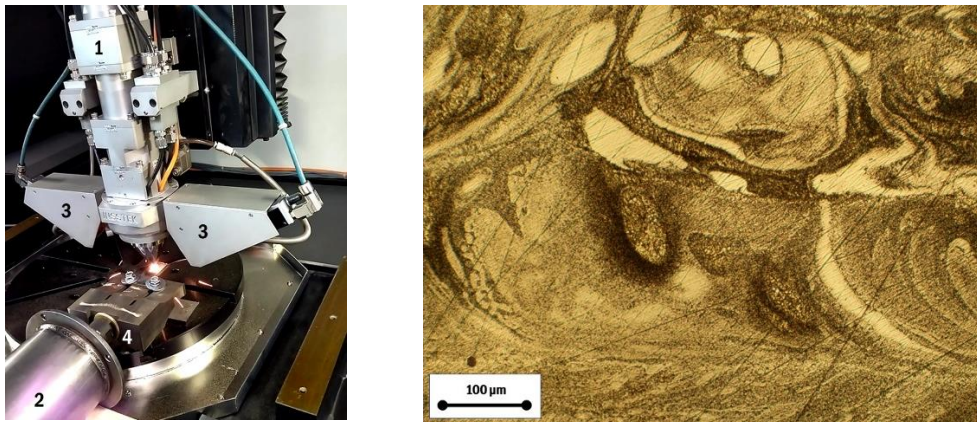


**Figure 41** – The ultrasonic-assisted DED process.

The ultrasonic-assisted DED process was suggested to achieve the following advantages:

- 1) Refinement of the grain structure: X.H. Wang et al. [231] demonstrated the refinement of Fe-based composite coating after ultrasonic-assisted DED, disappearance of

the columnar dendrites with 200 W ultrasonic power and appearance of the equiaxed dendrites with 400 W; C.J. Torado et al. [232] also observed the grain refinement 3D-printed Inconel 625 using the ultrasonic assistance, decrease of the epitaxial growth and improvement of homogeneity.

2) Increase of microhardness and wear resistance: X.H. Wang et al. [231] showed that the ultrasonic assistance increases the wear resistance of coating up to 2.4 times in comparison with a coating without ultrasonic assistance in the context of Fe-based composite DED-fabricated coating deposited on the 5CrNiMo substrate; D. Zhang et al. [233] observed the increase of microhardness from ~380–450 HV1.0 to ~435...515 HV1.0 at all levels of laser output power due to grain refinement and reduction of the porosity. Method of strengthening of a part surface, increase of an average impact energy, hardness, decrease of a wear mass loss, and redistribution of the reinforcement particles leading to their uniform dispersion, provided by the ultrasonic assistance, was also shown by the authors of patent [234].

3) Increase of elasticity modulus: D. Zhang et al. [233] showed that the ultrasonic vibration improves the elasticity modulus of the DED-fabricated parts from ~45–55 GPa to ~50–65 GPa.

4) Increase of the tensile strength: C.J. Torado et al [232] pointed at increase of tensile properties mostly due to the  $\beta$ -grain refinement: UTS with ultrasonic assistance of equal to ~1160 MPa (YS ~1100 MPa) while the results without ultrasonic assistance was: UTS ~1020 MPa, YS ~990 MPa (about 12% improvement of both parameters) of 3D-printed Ti-6Al-4V alloy. Y. Zhang et al. [235] achieved 1.4–1.6 times increase of tensile

strength of Al 4047 parts due to grain refinement using the ultrasonic-assisted DED instead of a traditional casting technology, and observed the microstructure consisted of the columnar Al dendrites with equiaxed Si particles at boundaries of the layers along with equiaxed Al crystals surrounded by fine Si phases in the middle zone of the alloy.

5) Reduction of the eutectic spacing: S. Yan et al. [236] reported about the decrease of this parameter in the carbon fiber toughening nanoscale Al<sub>2</sub>O<sub>3</sub>-ZrO<sub>2</sub> laser-deposited eutectic fabricated with the ultrasonic assistance. The resulted value reached  $50 \pm 5$  nm.

6) Improvement of the fracture toughness: S. Yan et al. [236] reported about 2.5-4 times increase of it the carbon fiber toughening nanoscale Al<sub>2</sub>O<sub>3</sub>-ZrO<sub>2</sub> eutectic due to the grain refinement and the whisker toughening of the carbon fiber.

7) Removal of cracking: the authors of the patent [237] described the laser deposition of Al-12Si eutectic alloy and found out that cracking in the deposited structure, that was seen after the common DED, wasn't observed when the ultrasonic-assisted DED was implemented, and the microstructure of the sedimentary layer was changed.

Because of a serious lack of experimental studies related to the topic of ultrasonic-assisted DED of Fe-Cu system materials, it is struggling to predict indisputably that all the mentioned changes, described above, will be seen in the materials of this system too. Nevertheless, our first tensile tests of the binary Cu(50%)-Fe(50%) alloy (see Figure 41 and its description) conducted in accordance with ASTM E8/E8M-16a [116] at a 2.7 mm/min rate using INSTRON 5969 dual column machine showed that the average ultimate tensile strength of common DED-fabricated parts equaled 848.3 MPa while this result in case of the ultrasonic-assisted DED reached 952.7 MPa, which was 1.12 times higher. Cu-

based parts created from the tin bronze powder without any Fe-based constituents also demonstrated the responsiveness to the agitation of a melt pool by the ultrasonic frequency waves during the DED: A. Gorunov [238] observed the intermixing between the tin bronze clads and a material of a substrate along with a substrate cracks bridging, and claimed that it is possible to variate size, shape, and intermixing rate of the deposited material by changing the ultrasonic-related parameters of the process.

It is known that there is a dependence between a mechanical performance and build orientation of parts fabricated via the traditional DED process. For instance, K. Zhang et al. [239] showed the difference of fracture morphology and anisotropic mechanical performance in specimens stretched parallel and perpendicular to the build direction; P. Guo et al. [240] reported that the higher elongation at failure was seen at  $0^\circ$  build direction rather than at  $90^\circ$ , what was an unexpected result, because in the second case the direction of external load was parallel to the dendritic grains; E. Azinpour et al. [241] observed the lower UTS and yield stress values of parts fabricated at  $0^\circ$  building direction in respect to direction of load, in comparison with that of  $90^\circ$ . The build orientation of the part during the ultrasonic-assisted DED plays even a more important role in further mechanical characteristics, microstructure and morphology parameters because of significance of the mutual disposition between the ultrasonic wave front and the axes of the solidified grains of the material. Besides, the absorption of mechanical ultrasonic wave energy during its propagation within the volume of the part points at influence of a part's size and geometry on the ultrasonic-affected changes of its microstructural and mechanical properties. It was expected to observe a lower ultrasonic influence at the highest layers of

a tall part, if it was built in a vertical direction. Contrarily, if the part was built in horizontal direction, the ultrasonic influence was more uniform and was expected to have a more regular distribution. The evaluation of ultrasonic attenuation in polycrystalline metals occurring mostly because of scattering from grains was conducted by T. Stepinski and P. Wu [242] for the pure copper specimens. A frequency-dependent attenuation coefficient  $\zeta(f)$  was determined by the spectral shift method (based on the measurement of a signal reflected from the front and backs surfaces of the metal plate) using the following equation:

$$\zeta(f) = \left(\frac{2 \cdot \pi}{B}\right)^2 \cdot \frac{f_i - f_0}{2 \cdot D} \cdot f, \quad (63)$$

where  $B$  is a bandwidth of the input signal,  $f_i$  and  $f_0$  are the central frequencies of the input and output signal respectively, and  $2 \cdot D$  is a full path length of an ultrasonic signal ( $D$  – a thickness of the plate). The resulting measured attenuation amounted from  $0.3684^{+0.0398}_{-0.0469}$  to  $0.4613^{+0.0489}_{-0.0645}$  for 5.35 MHz central frequency in dependence from the specimen thickness (from 36 to 41.5 mm) and nominal grain size (from 125–175 to 250–350  $\mu\text{m}$ ). These results showed that at the high frequencies the intensity of an ultrasonic wave in Cu polycrystal decreased by approximately 1.09–1.11 times per each mm propagated. Therefore, the Cu specimen even of a 40 mm height will suffer more than 30 times decrease of the ultrasonic wave intensity at its top surface at this frequency (5.35 MHz).

Except mentioned above, we observed during the experiments that parts fabricated with ultrasonic assistance in a vertical build direction showed the defects increasing from the bottom to the top side (see left picture in Figure 42). Nevertheless, the similar parts fabricated at the same operation conditions in a horizontal orientation had a regular shape and normal roughness (Figure 42, middle picture). The same was shown by parts deposited

in a vertical direction without ultrasonic assistance (Figure 42, right picture). The increase of a surface roughness of the first part could be caused by a spatter due to significant vibration, or by difference of cooling rate of the lowest and the highest layers [74]. This difference comes from the fact that layers, larger affected by ultrasonic vibration, undergo more intense stirring provided by cavitation and acoustic flow effects [243] in a melt pool. The cavitation effect is associated with nonlinearly expanding, contracting, oscillating, shrinking, and collapsing cavitation bubbles in liquid under alternating negative and positive pressure. The collapses of the bubbles produce instantaneous high temperature and pressure [244] in the surrounding area followed by generation of high-speed liquid microjets and new bubbles nuclei keeping the ultrasonic cavitation process and promoting the liquid flow in the melt pool. The acoustic flow effect is a result of a sound pressure gradient caused by attenuation of the ultrasonic wave during its propagation in the melt. The sound flow slows down by reaching the bottom of the cavity, spreads upward along its side wall, and forms the circulation. The induced acoustic flow effect effectively promotes the flow in the molten pool, amplifying the effect of convection and diffusion.



**Figure 42** – Parts fabricated: a) with ultrasonic assistance (built in a vertical direction) (left picture); b) with ultrasonic assistance (built in a horizontal direction) (middle picture); c) without ultrasonic assistance (built in a vertical direction) (right picture).

The changes of the part's shape in its top section could appear because of a disproportional distribution of the powder due to vibration of the mounting layers and substrate. These defects were partially observed not only in parts fabricated via the ultrasonic-assisted DED, but the presence of ultrasonic vibration increased them. Columnar-shaped vertical tall deposit is seen only on the left side of the specimen because of specificity of the track pattern: the path of the nozzle within each layer is finished near this area, therefore the last fallen powder particles are sintered to the hot surface even if the laser is already turned off. The mentioned defects could be reduced or eliminated by changing of a part build direction, as it shown in Figure 42, or decrease of an ultrasonic generator output power.

This topic has to be continued with the deeper study of the ultrasonic-assisted DED, specifically its influence on the surface parameters, microhardness, and elasticity modulus of as-fabricated parts.

### 8.3 Laser Deposition of a Real SS 316L – Bronze Gradient Part

The final result of all the experimental and theoretical investigations of the DED of Fe-Cu system FGMs have to be the fabrication and testing of the real part. In this study, a cooling stave was selected as this part. A cooling stave is the key element of the blast furnace. It is a region of the biggest heat load with intensified smelting [245].

The blast furnace is mostly used in steel industries and produces molten iron [246]. Its scheme is shown in Figure 43.

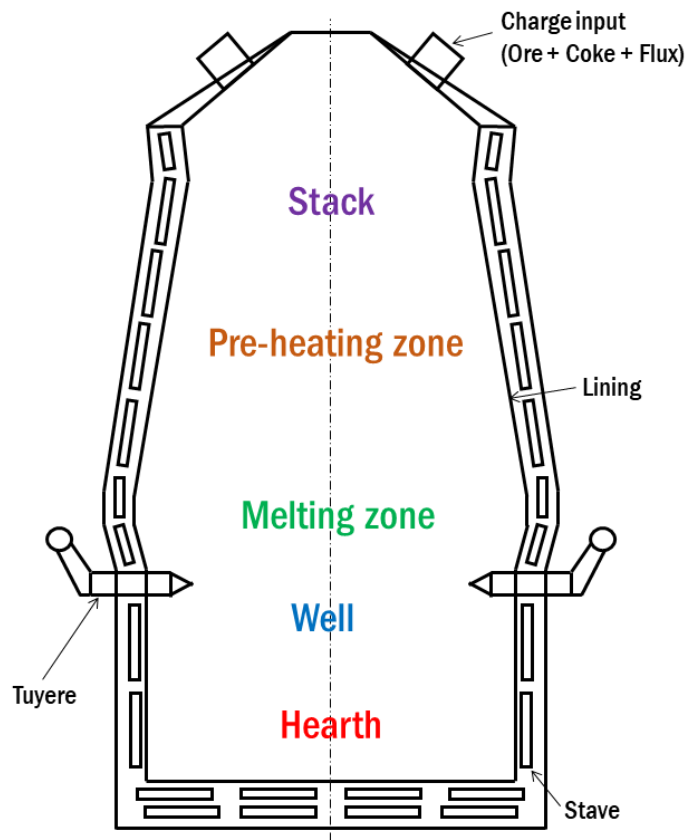


**Figure 43** – The scheme of the blast furnace [246,247].

Lining of the cooling stave is the most important factor for determining the blast furnace's campaign life. Lining cooling by stave is one of the most leading factors in this

field [246]. A stave is a cooling gadget, which has one or several internal channels. Staves are placed on the inward surface of a blast furnace. Conventionally, they were produced from cast iron but further it was suggested to fabricate them from copper to achieve better thermal conductivity [246]. Nevertheless, cost of copper staves is higher, and steel staves have better mechanical properties like specific elongation and tensile strength [246]. It was suggested further [13] to combine properties of copper and steel within the cooling stave. Therefore, modern cooling staves are FG tools, which are placed along the periphery of the blast furnace wall [247]. After our experiments, the sample of the FG cooling stave was fabricated (Figure 44). It was produced both from steel (body) and bronze (ribs or bricks). The dimensions were ten-times decreased in comparison to real ones.

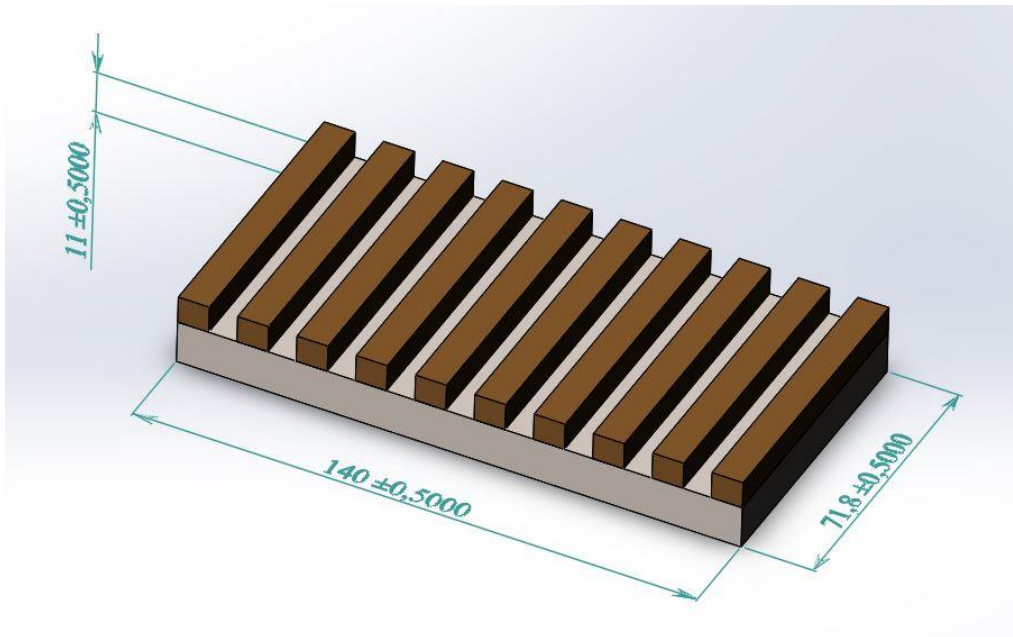


**Figure 44** – The sketch of the cooling stave.

In our experiment, the cooling stave's body was fabricated from SS 316L, and the bricks were produced from three kinds of bronze: aluminum bronze (similar to UNS

C61800 aluminum bronze, fraction 45–125  $\mu\text{m}$ ), tin bronze (similar to copper-tin alloy CuSn10-B (CB480K), fraction 100–140  $\mu\text{m}$ ), and chromium bronze (similar to UNS C18400 chromium copper, fraction 63–125  $\mu\text{m}$ ). First three ribs realized direct joining method; three next – gradient path; the last three bricks – alternating layers' technique. All the ribs were fabricated with acceptable metallurgical bonding between bronze and steel and without visible defects such as cracks and gas pockets. This experiment demonstrated that direct joining can be applied for manufacturing of small-size parts from Fe-Cu FGMs; nevertheless, it is unsuitable for the huge parts (with >15 mm dimension in the direction of chemical composition changing). The experiment proved practical significance of previous research results and demonstrated their applicability for manufacturing real FG parts based on Fe-Cu system.

The resulting cooling stove after mechanical treatment (electrical discharge machining, grinding, polishing) is shown in Figure 45.

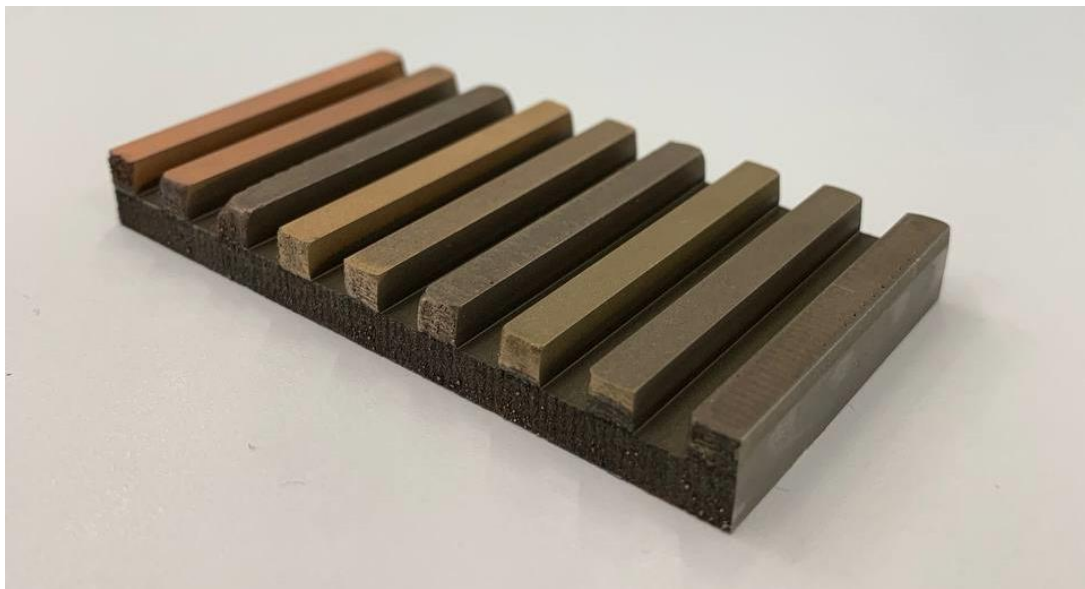


**Figure 45** – The resulting cooling stove after processing.

Future research has to include thermo-mechanical testing of this part and fabrication of an FG part with more complicated geometry such as the prototype of the rocket engine's combustion chamber.

#### **8.4 Additional Directions of the Research**

Additionally, the following topics may be suggested for the further investigation:

- The expected positive influence of the Fe, Cr, Ni, and Mo content's increase and the negative influence of that of Cu and Al on mechanical properties of the C61800-based Fe-Cu transitional zones of the DED-fabricated FGMs.
- Conducting the SEM and XRD analyses of the Cr-bronze-based DEDed alloys to define the nature of microstructural defects responsible for lowering UTS.
- Study of the reasons of the mismatch between strain and stress concentrators in the tin-bronze-based quasi-homogeneous Fe-Cu system DED-fabricated alloys.
- Performing high-temperature mechanical testing of various Fe-Cu system DED-fabricated quasi-homogeneous alloys and FGMs.
- Finding the size of the hugest dendrites and the corresponding distance between their location and the position of the crystallization front in Fe-Cu system FGMs.
- Proving the proposition about the absence of the dendrites in Fe-Cu system FGMs after the specific critical point far from the center of the laser heat spot.
- The determination of the temperature gradient in the volume of the DEDed Fe-Cu alloys.

- The admixture mass concentration evaluation of laser-deposited FGMs of Fe-Cu system.
- The estimation of the vertex angles of the dendrites growing in the Fe-Cu FGMs and comparison of the analytical values with the angles measured during experiments.
- Research of the essence of the Cu-Fe-Cr system's transient behavior, which may provoke low-temperature (100–300 °C) phase transitions in Cr bronze – steel quasi-homogeneous and FG alloys leading to their heat capacity decrease during heating.
- The analysis of the specific heat capacity behavior of the Fe-Cu materials in the 300 – 900 °C temperature range.
- Study of microstructural, mechanical, thermal, and magnetic characteristics of Be-, Pb-, and Si-bronze-based Fe-Cu system DED-fabricated FGMs.
- Study of the oscillating laser DED technology for producing Fe-Cu FGMs.

## Bibliography

- 1 Watanabe Y, and Sato H. Review fabrication of functionally graded materials under a centrifugal force. In *Nanocomposites with Unique Properties and Applications in Medicine and Industry*; IntechOpen: London, UK, **2011**; pp. 133–50. DOI: 10.5772/20988
- 2 Singh R, Bhavar V, Kattire P, Thakare S, Patil S, and Singh RKP. *Mater. Sci. Eng.* **2017**, 229, 012021. DOI: 10.1088/1757-899X/229/1/012021
- 3 Shishkovsky IV. *Rapid Prototyp. J.* **2001**, 7(4), pp. 207–11. DOI: 10.1108/13552540110402908
- 4 Saleh B, Jiang J, Fathi R, Al-hababi T, Xu Q, Wang L, Song D, and Ma A. *Compos. Part. B* **2020**, 201, 108376. DOI: 10.1016/j.compositesb.2020.108376
- 5 Mahamood MR, Akinlabi ET, Shukla M, and Pityana S. *Proc. World Congr. Eng.* **2012**, 3, 1593–7.
- 6 Makarenko K, Dubinin O, and Shishkovsky I. *Materials.* **2020**, 13, 5665. DOI: 10.3390/ma13245665
- 7 Sun X, Hao W, Geng G, Ma T, and Li Y. *Adv. Mater. Sci. Eng.*, **2018**, 2018, 6304518. DOI: 10.1155/2018/6304518
- 8 Cao MM, Zhou ZM, Tang LW et al. *Mater. Guide: Nano New Mater. Alb.* **2011**, 25, 2, in Chinese.
- 9 Imada R, Fujiwara Y, and Tsunashima S. *J. Appl. Phys.* **1997**, 81, 8. DOI: 10.1063/1.364462
- 10 Monchesky TL, Heinrich B, Urban R, Myrtle K, Klaua M, and Kirschner J. *Phys. Rev. B.* **1999**, 60, 10242. DOI: 10.1103/PhysRevB.60.10242

- 11 Monchesky TL, Urban R, Heinrich B, Klaua M, Kirschner J. *J. Appl. Phys.* **2000**, 87(9), pp. 5167–9. DOI: 10.1063/1.373283
- 12 Hedgcock FT, Muir WB, Raudorf TW, Szmidt R. *Phys. Rev. Lett.* **1968**, 20, 457. DOI: 10.1103/PhysRevLett.20.457
- 13 Y. Wang, Y. Gao, Y. Li, W. Zhai, L. Sun, C. Zhang. *Emerging Materials Research.* **2019**, 8(4), pp. 538–51. DOI: 10.1680/jemmr.17.00008
- 14 Kiyoshi Ichikawa. Functionally graded materials in the XXI century. A Workshop on Trends and Forecasts, **2001**. DOI: 10.1007/978-1-4615-4373-2
- 15 Makarenko K, and Shishkovsky I. *IOP Conf. Ser. Mater. Sci. Eng.* **2020**, 969, 012104. DOI: 10.1088/1757-899X/969/1/012104
- 16 Wołosz P, Baran A, and Polański M. *J. Alloys Compd.* **2020**, 823(7), 153840. DOI: 10.1016/j.jallcom.2020.153840
- 17 Sahasrabudhe H, Harrison R, Carpenter C, and Bandyopadhyay A. *Addit. Manuf.* **2015**, 5, 1–8. DOI: 10.1016/j.addma.2014.10.002
- 18 Doubenskaia M, Kulish A, Sova A, Petrovskiy P, and Smurov I. *Surf. Coat. Technol.* **2020**, 126672, DOI: 10.1016/j.surfcoat.2020.126672
- 19 Xiaodong He, Jiecai Han, Xinghong Zhang. Preparation and Ablating Behavior of FGM used in a Heat Flux Rocket Engine. IAF abstracts, 34th COSPAR Scientific Assembly, The Second World Space Congress, held 10-19 October, **2002** in Houston, TX, USA, I-4-03, meeting abstract id.463
- 20 Hofmann DC, Roberts S, Otis R, Kolodziejska J, Dillon RP, Suh J-o, Shapiro AA, Liu K-Z, and Borgonia J-P. *Sci. Rep.* **2014**, 4, 5357. DOI: 2010.1038/srep05357

- 21 Udupa G, Shrikantha Rao S, and Gangadharan KV. *Proc. Mater. Sci.* **2014**, *5*, pp. 1291–9. DOI: 10.1016/j.mspro.2014.07.442
- 22 Richter V. FGM'94. In Proceedings of the 3rd International Symposium on Structural and Functional Gradient Mater, Lausanne, Switzerland, 10–12 October **1994**, pp. 587–92.
- 23 Makarenko K, Dubinin O, and Shishkovsky I. *Metals.* **2023**, *13(3)*, 451. DOI: 10.3390/met13030451
- 24 Articek U, Milfelner M, and Anzel I **2013** Synthesis of functionally graded material H13/Cu by LENS technology *Adv. Prod. Eng. Manag.* **8**, *3*, pp. 169–76. DOI: 10.14743/apem2013.3.164
- 25 Moharana BR, Sahu SK, Maiti A, Sahoo SK, and Moharana TK. *Mater. Today: Proc.* **2020**. (Preprint 2214-7853)
- 26 Tan C, Zhou K, Ma W, and Min L. *Mater. Des.* **2018**, *155*, pp. 77–85. DOI: 10.1016/j.matdes.2018.05.064
- 27 Onuiké B, Heer B, and Bandyopadhyay A. *Addit. Manuf.* **2018**, *21*, pp. 133–40. DOI: 10.1016/j.addma.2018.02.007
- 28 Karnati S, Sparks TE, Liou F, Newkirk JW, Tamingir KMB, and Seufzer WJ. Laser metal deposition of functionally gradient materials from elemental copper and nickel powders. In Proceedings of the 26th Solid Freeform Fabrication Symposium, 10–12 August 2015; Bourell, D.L., Ed.; The University of Texas: Austin, TX, USA, **2015**, pp. 789–802.
- 29 Shakerin S, Sanjari M, Amirkhiz BS, and Mohammadi M. *Mater. Charact.* **2020**, *170*, 110728. DOI: 10.1016/j.matchar.2020.110728

- 30 Oropeza D, Firdosy S, and Hofmann DC. *Addit. Manuf. Lett.* **2022**, 3, 100078. DOI: 10.1016/j.addlet.2022.100078
- 31 Shishkovsky I, Kakovkina N, and Missemmer F *Laser Eng.* **2016**, 33, pp. 1–15.
- 32 Vilar R et al *Acta Mater.* **2009**, 57(18), pp. 5292–302. DOI: 10.1016/j.actamat.2009.06.049
- 33 Balla VK, DeVasConCellos PD, Xue W, Bose S, and Bandyopadhyay A *Acta Biomater.* **2009**, 5, pp. 1831–7. DOI: 10.1016/j.actbio.2009.01.011
- 34 Shishkovsky I, Missemmer F, and Smurov I. *Phys. Proc.* **2012**, 39, pp. 382–91. DOI: 10.1016/j.phpro.2012.10.052
- 35 Srivastava D, Chang I T H, and Loretto M H. *Intermetallics* **2001**, 9(12), pp. 1003–13. DOI: 10.1016/S0966-9795(01)00063-2
- 36 Liu W and DuPont J N *Metallurg. Mater. Transact. A* **2004**, 35(13), pp. 1133–40. DOI: 10.1007/s11661-004-0039-2
- 37 Pimenova N V, and Starr T L *Electromech. Acta* **2006**, 51, pp. 2042–49. DOI: 10.1016/j.electacta.2005.07.024
- 38 He X, Han J, and Zhang X. Preparation and ablating behaviour of FGM used in a heat flux rocket engine. In Proceedings of the 34th COSPAR Scientific Assembly of the 2nd World Space Congress, Houston, TX, USA, 10–19 October 2002; NASA Astrophysics Data System: Cambridge, MA, USA, **2002**.
- 39 Moussa AA, and Yadav R *J. Medic. Eng.* **2017**, 3069351. DOI: 10.1155/2017/3069351
- 40 Pei YT, and De Hosson J TH M *Acta Mater.* **2000**, 48, pp. 2617–24. DOI: 10.1016/S1359-6454(00)00065-3

- 41 Peška M, Karczewski K, Rzeszotarska M, and Polański M *Mater.* **2020**, *13*, 531. DOI: 10.3390/ma13030531
- 42 Łyszkowski R *Mater.* **2015**, *8*, pp. 1499–512. DOI: 10.3390/ma8041499
- 43 Novák P, Zelinková M, Šerák J, Michalcová A, Novák M, and Vojtěch D *Intermetallics* **2011**, *19*, pp. 1306–12. DOI: 10.1016/j.intermet.2011.04.011
- 44 Morris DG, Gutierrez-Urrutia I, and Muñoz-Morris M A *Int. J. Plast* **2008**, *24*, pp. 1205–23. DOI: 10.1016/j.ijplas.2007.09.001
- 45 Schmitt A, Kumar KS, Kauffmann A, Li X, Stein F, and Heilmaier M *Intermetallics* **2017**, *90*, pp. 180–7. DOI: 10.1016/j.intermet.2019.01.015
- 46 Liu Y, Chong X, Jiang Y, Zhou R, and Feng J *Phys. B* **2017**, *506*, pp. 1-11. DOI: 10.1016/j.physb.2016.10.032
- 47 Shen C, Liss K, Pan Z, Wang Z, Li X, and Li H *Intermetallics* **2018**, *92*, pp. 101–7. DOI: 10.1016/j.intermet.2017.09.024
- 48 Ruan Y, Zan N, Zhu HZ, Zhou K, and Wei B *J. Alloys Compd.* **2017**, *701*, pp. 676–81. DOI: 10.1016/j.jallcom.2017.01.131
- 49 Sahasrabudhe H, Bose S, and Bandyopadhyay A *Acta Biomater.* **2018**, *66*, pp. 118–28. DOI: 10.1016/j.actbio.2017.11.022
- 50 Banait SM, Paul CP, Jinoop AN, Kumar H, Pawade RS, and Bindra K S *Opt. Las. Technol.* **2020**, *121*, 105787. DOI: 10.1016/j.optlastec.2019.105787
- 51 Amado JM, Montero J, Tobar MJ, and Yáñez A *Phys. Proc.* **2012**, *39*, pp. 362–67. DOI: 10.1016/j.phpro.2012.10.049

- 52 Li W, Karnati S, Kriewall C, Liou F, Newkirk J, Taminger KMB, and Seufzer WJ *Addit. Manuf.* **2017**, *14*, pp. 95–104. DOI: 10.1016/j.addma.2016.12.006
- 53 Reichardt A, Dillon RP, Borgonia JP, Shapiro AA, McEnerney BW, Momose T, and Hosemann P. *Mater. Des.* **2016**, *104*, pp. 404–13. DOI: 10.1016/J.MATDES.2016.05.016.
- 54 Onuike B, Heer B, and Bandyopadhyay A. *Addit. Manuf.* **2018**, *21*, pp. 133–40. DOI: 10.1016/j.addma.2018.02.007
- 55 Islam M, Thakur MSH, Mojumer S, Amin A, and Islam MM. *Comp. Part B.* **2020**, *198*, 108212. DOI: 10.1016/j.compositesb.2020.108212
- 56 Kim CS **1975** Thermophysical properties of stainless steels. Argonne National Laboratory, Argonne, Illinois, USA. Prepared for the U.S. Energy Research and Development Administration.
- 57 Esmeralda AG, Rodríguez AF, Talamantes-Silva J, Torres R, Garza-Montes-de-Oca NF, Benavides-Treviño JR, and Colás R. *Thermochim. Acta*, **2020**, *683*, 178444. DOI: 10.1016/j.tca.2019.178444
- 58 Boukhriss M, Zhani K, and Ghribi R. *Desalin. Water Treat.*, **2013**, *51*, pp. 1290–5. DOI: 10.1080/19443994.2012.714925
- 59 Zhang C, Du Y, Liu S, Liu Y, and Sundman B. *Thermochim. Acta*, **2016**, *635*, pp. 8–16. DOI: 10.1016/j.tca.2016.04.019
- 60 Stepanova NV, Bataev IA, Youn-Bae Kang et al. *Mater. Charact.* **2017**, *130*, pp. 260–9. DOI: 10.1016/j.matchar.2017.06.025
- 61 Surinder Singh, Parminder Singh, Harpreet Singh, Ramesh Kumar Buddu. *Mater. Today: Proc.* **2019**, *18(3)*, pp. 830–40. DOI: 10.1016/j.matpr.2019.06.509

- 62 Jendrzewski R, Śliwiński G, Krawczuk M, and Ostachowicz W. *Computers & Structures* **2004**, 82, pp. 653–8. DOI: 10.1016/j.compstruc.2003.11.005
- 63 Fatoba OS, Akinlabi ET, and Makahtha ME. *Int. J. Adv. Manuf. Technol.* **2018**, 94, pp. 773–87. DOI: 10.1016/j.matpr.2018.06.176
- 64 Svetlizky D, Das M, Zheng B, Vyatskikh AL, Bose S, Bandyopadhyay A, Schoenung JM, Lavernia EJ, and Eliaz N. *Mater. Today* **2021**, 49, pp. 271–95. DOI: 10.1016/j.mattod.2021.03.020
- 65 Ghosal P, Chandra Majumder M, Chattopadhyay A. *Mater. Today: Proc.* **2018**, 5, pp. 12509–18. DOI: 10.1016/j.matpr.2018.02.232
- 66 Ahn D.-G. *Int. J. Precis. Eng. Manuf. Green Technol.* **2021**, 8, pp. 703–42. DOI: 10.1007/s40684-020-00302-7
- 67 Dutta B. *Encyclopedia of Materials: Metals and Alloys.* **2022**, 3, pp. 66–84. DOI: 10.1016/B978-0-12-819726-4.00035-1
- 68 Feenstra DR, Banerjee R, Fraser HL, Huang A, Molotnikov A, and Birbilis N. *Curr. Opin. Solid State Mater. Sci.* **2021**, 25, 100924. DOI: 10.1016/j.cossms.2021.100924.
- 69 Ansari M, Jabari E, Toyserkani E. *J. Mater. Process. Technol.* **2021**, 294, 117117. DOI: 10.1016/j.jmatprotec.2021.117117.
- 70 Farzaneh A, Khorasani M, Farabi E, Gibson I, Leary M, Ghasemi A, and Rolfe B. *Virtual Phys. Prototyp.* **2022**, 17, 1006–30. DOI: 10.1080/17452759.2022.2096647
- 71 Lei Yan, Yitao Chen, Frank Liou. *Addit. Manuf.* **2020**, 31, 100901. DOI: 10.1016/j.addma.2019.100901

- 72 Chen B, Wang T, Xi X, Tan C, and Song X. *Rapid Prototyp. J.* **2022**, ahead-of-print. DOI: 10.1108/RPJ-04-2022-0117
- 73 Tudu N, Baruah M, Prasad SB. *Rapid Prototyp. J.* **2022**. DOI: 10.1108/RPJ-08-2021-0219
- 74 Liu M, Kumar A, Bukkapatnam S, and Kuttolamadom M. *Procedia Manuf.* **2021**, 53, pp. 507–18. DOI: 10.1016/j.promfg.2021.06.093
- 75 Bedenko D, Kovalev O, Smurov IY, Zaitsev AV. *Int. J. Heat Mass Transfer.* **2016**, 95, pp. 902–12 (2016). DOI: 10.1016/j.ijheatmasstransfer.2015.12.046
- 76 Miedzinski M. **2017**, «Materials for Additive Manufacturing by Direct Energy Deposition», Department of Materials and Manufacturing Technology, Chalmers University of Technology.
- 77 Qi H, Mazumder J, Ki H. *J. Appl. Phys.* **2006**, 100(2), 024903. DOI: 10.1063/1.2209807
- 78 Laeng J, Stewart J, Liou FW. *Int. J. Prod. Res.* **2000**, 38(16), pp. 3973–96. DOI: 10.1080/00207540050176111
- 79 Grigoryants AG. *The Fundamentals of a Laser Treatment of Materials*. Moscow: Mashinostroenie Publishing; **1989**. 301 p. ISBN: 5-217-00432-0.
- 80 Yan L, Chen Y, and Liou F. *J. Mater. Res. Technol.* **2021**, 13, pp. 1628–64. DOI: 10.1016/j.jmrt.2021.05.022
- 81 Vedenov AA, and Gladush GG. *Physical processes during laser treatment of materials*. Moscow: Energoatomisdat; **1985**. 208 p.
- 82 Thompson SM, Bian L, Shamsaei N, and Yadollahi A. *Addit. Manuf.* **2015**, 8, pp. 36–62. DOI: 10.1016/j.addma.2015.07.001

- 83 Zhang X, Pan T, Flood A, Chen Y, Zhang Y, and Liou F. *Mater. Sci. Eng. A* **2021**, *811*, 141071. DOI: 10.1016/j.msea.2021.141071
- 84 Zhang H, Chen Y, Pan T, Cui W, Li L, and Liou F. Joining of copper and stainless steel 304L using direct metal deposition. In: Proceedings of the 30th Annual International Solid Freeform Fabrication Symposium; 12-14 August **2019**; Austin, TX. pp. 388–403
- 85 Prasad HS, Brueckner F, Volpp J, Kaplan AFH. *Int. J. Adv. Manuf. Technol.* **2020**, *107*, pp. 1559–68. DOI: 10.1007/s00170-020-05117-z
- 86 Shishkovsky IV, Missemer F, and Smurov IY. *Comp. Struct.* **2018**, *39*, pp. 382–91. DOI: 10.1016/j.phpro.2012.10.052
- 87 Bai Y, Zhang J, Zhao C, Li C, and Wang H. *Mater. Charact.* **2020**, *167*, 110489. DOI: 10.1016/j.matchar.2020.110489
- 88 Osipovich KS, Gurianov DA, and Chumaevsky AV. *IOP Conf. Ser.: Mater. Sci. Eng.* **2021**, *1079*, 042089. DOI: 10.1088/1757-899X/1079/4/042089
- 89 Arias-González F, del Val J, Comesaña R et al. *Surf. Coat. Technol.* **2017**, *313*, pp. 248–54. DOI: 10.1016/j.surfcoat.2017.01.097
- 90 Borges B, Quintino L, Miranda RM, and Carr P. *Int. J. Adv. Manuf. Technol.* **2010**, *50*, pp. 175–83. DOI: 10.1007/s00170-009-2480-2
- 91 Ocelík V, de Oliveira U, de Boer M, and de Hosson JTM. *Surf. Coat. Technol.* **2007**, *201*, pp. 5875–83. DOI: 10.1016/j.surfcoat.2006.10.044
- 92 Steen WM, Weerasinghe VM, and Monson P. *Proc. SPIE - Int. Soc. Opt. Eng.* **1986**, *650*. DOI: 10.1117/12.938104

- 93 De Oliveira U, Ocelík V, and De Hosson JTM. *Surf. Coat. Technol.* **2005**, *197*, pp. 127–36. DOI: 10.1016/j.surfcoat.2004.06.029
- 94 Surinder Singh, Manoj Kumar, Gurvinder Pal Singh Sodhi et al. *Fusion Eng. Des.* **2018**, *128*, pp. 126–37. DOI: 10.1016/j.fusengdes.2018.01.076
- 95 Gedda H, Kaplan A, and Powell J. *J. Metall. Mater. Trans. B* **2005**, *36(5)*, pp. 683–9. DOI: 10.1007/s11663-005-0059-3
- 96 Tanigawa D, Abe N, Tsukamoto M et al. Proceedings of ICALEO 2015, Atlanta – Georgia; USA, 2015. pp. 18-22.
- 97 Tanigawa D, Abe N, Tsukamoto M et al. *Opt. Lasers Eng.* **2018**, *101*, pp. 23–7. DOI: 10.1016/j.optlaseng.2017.09.021
- 98 Prasad HS, Brueckner F, Volpp J, and Kaplan AFH. *Int. J. Adv. Manuf. Technol.* **2020**, *107*, pp. 1559–68. DOI: 10.1007/s00170-020-05117-z
- 99 Prasad HS, Brueckner F, and Kaplan A. *Lasers in Manufacturing Conference München*, Germany, June 24–7, **2019**.
- 100 Wang CP, Liu XJ, Ohnuma I, Kainuma R, and Ishida K. *J. Ph. Equilibria Diffus.* **2004**, *25*, pp. 320–8. DOI: 10.1007/s11669-004-0150-5
- 101 Curiotto S, Greco R, Pryds NH, Johnson E, and Battezzati L. *Fluid Ph. Equilibria.* **2007**, *256*, pp. 132–136. DOI: 10.1016/j.fluid.2006.10.003
- 102 Chuang Y, Schmid R, Chang Y. *Metall. Trans. A.* **1984**, *15*, pp. 1921–30. DOI: 10.1007/BF02664905
- 103 Ma E, Atzmon M, and Pinkerton FE. *J. Appl. Phys.* **1993**, *74*, 955. DOI: 10.1063/1.354837

- 104 Raghavan V. Al-Cu-Fe (Aluminum-Copper-Iron). *J. Ph. Equilibria Diffus.* **2005**, *26(1)*, pp. 59–64. DOI: 10.1361/15477030522509
- 105 Raghavan V. Al-Cu-Fe (Aluminum-Copper-Iron). *Jour J. Ph. Equilibria Diffus.* **2010**, *31(5)*, pp. 449–52. DOI: 10.1361/15477030522509
- 106 Chen HL, Du Y, Xu H, and Xiong W. *J. Mater. Research.* **2009**, *24(10)*, pp. 3154–64. DOI: 10.1557/jmr.2009.0376
- 107 Soffel F, Papis K, Bambach M, and Wegener K. *Metals* **2022**, *12(4)*, 614. DOI: 10.3390/met12040614
- 108 Svetlizky D, Das M, Zheng B, Vyatskikh AL, Bose S, Bandyopadhyay A, Schoenung JM, Lavernia EJ, and Eliaz N. *Mater. Today.* **2021**. DOI: 10.1016/j.mattod.2021.03.020
- 109 Kou S. *JOM.* **2003**, *55*, pp. 37–42. DOI: 10.1007/s11837-003-0137-4
- 110 Wei HL, Mukherjee T, Zhang W, Zuback JS, Knapp GL, De A, and DebRoy T. *Progress Mater. Sci.* **2021**, *116*, 100703. DOI: 10.1016/j.pmatsci.2020.100703
- 111 Attalah MM, Jennings R, Wang X, and Carter LN. Additive manufacturing of Ni-based superalloys: The outstanding issues. *MRS Bulletin.* **2016**, *41*, pp. 758–64. DOI: 10.1557/mrs.2016.211
- 112 Bi G, and Gasser A. *Phys. Procedia.* **2011**, *12*, pp. 402–9. DOI: 10.1016/j.phpro.2011.03.051
- 113 Ramirez AJ, and Lippold JC. *Mater. Sci. Eng. A.* **2004**, *380*, pp. 259–71. DOI: 10.1016/j.msea.2004.03.074
- 114 Noecker FF, and DuPont JN. *Welding J.* **2009**, *88(1)*, pp. 7s–20s.

- 115 Bahl S, Plotkowski A, Sisco K, Leonard DN, Allard LF, Michi RA, Poplawsky JD, Dehoff R, and Shyam A. *Acta Mater.* **2021**, *220*, 117285. DOI: 10.1016/j.actamat.2021.117285
- 116 ASTM International: ASTM E8/E8M-16a, Standard Test Methods for Tension Testing of Metallic Materials, <https://www.astm.org/DATABASE.CART/HISTORICAL/E8E8M-16A.htm>. Accessed 28 Aug 2021
- 117 Gao N, Starink MJ, and Langdon TG. *Mater. Sci. Technol.* **2013**, *25*, pp. 687–98. DOI: 10.1179/174328409X408901
- 118 Makarenko K, Dubinin O, Shornikov P, and Shishkovsky I. *Procedia CIRP* **2020**, *94*, pp. 346–51. DOI: 10.1016/j.procir.2020.09.143
- 119 InssTek MX-1000 Technical Data. Electronic source. URL: <http://www.insstek.com/content/standard/mx1000>. Accessed March 15, 2020.
- 120 Lei Yan, Yitao Chen, and Frank Liou. *Addit. Manuf.* **2020**, *31*, 100901. DOI: 10.1016/j.addma.2019.100901
- 121 Makarenko K., Dubinin O, and Shishkovsky I. Direct Energy Deposition of Cu-Fe System Functionally Graded Materials: Miscibility Aspects, Cracking Sources, and Methods of Assisted Manufacturing. In *Advanced Additive Manufacturing*; Shishkovsky, I.V., Ed.; IntechOpen: London, UK, **2022**. DOI: 10.5772/intechopen.102562
- 122 Chen N, Ali Khan H, Wan Z, Lippert J, Sun H, Shang S-L, Liu Z-K, and Li J. *Addit. Manuf.* **2020**, *32*, 101037. DOI: 10.1016/j.addma.2020.101037
- 123 Koga N, Tomono S, and Umezawa O. *Mater. Sci. Eng. A* **2021**, *811*, 141066. DOI: 10.1016/j.msea.2021.141066

- 124 Koga N, Zhang W, Umezawa O, Tschan V, Sas J, and Weiss KP. *IOP Conf. Ser. Mater. Sci. Eng.* **2017**, 279, 012004. DOI: 10.1088/1757-899X/279/1/012004
- 125 Makarenko KI, Konev SD, Dubinin ON, and Shishkovsky IV. *Mater. Des.* **2022**, 224, 111313. DOI: 10.1016/j.matdes.2022.111313
- 126 3D Laser Printers. Direct Metal Tooling. Electronic source. URL: <https://www.tlm-laser.com/laser-products/3d-laser-printing>. Accessed Jun 27, 2023.
- 127 ASTM International: ASTM E3-11(2017), Standard Guide for Preparation of Metallographic Specimens. URL: <https://www.astm.org/e0003-11r17.html>. Accessed Feb 20, 2022.
- 128 ASTM International: ASTM E340-13, Standard Test Method for Macroetching Metals and Alloys. URL: <https://www.astm.org/e0340-13.html>. Accessed Feb 20, 2022.
- 129 ASTM International: ASTM E2014-17, Standard Guide on Metallographic Laboratory Safety. URL: <https://www.astm.org/e2014-17.html>. Accessed Feb 20, 2022.
- 130 ASTM International: ASTM E766-14(2019), Standard Practice for Calibrating the Magnification of a Scanning Electron Microscope. URL: <https://www.astm.org/e0766-14r19.html>. Accessed Feb 20, 2022.
- 131 ASTM E1508-12A(2019), Standard Guide for Quantitative Analysis by Energy-Dispersive Spectroscopy. URL: [https://www.techstreet.com/standards/astm-e1508-12a-2019?product\\_id=2091917](https://www.techstreet.com/standards/astm-e1508-12a-2019?product_id=2091917). Accessed Feb 20, 2022.
- 132 Seki I, and Nagata K. *ISIJ International*, **2005**, 45(12), pp. 1789–94. DOI: 10.2355/isijinternational.45.1789

- 133 Soulairol R, Fu C-C, and Barreteau C. *J. Phys. Condens. Matter*, **2010**, 22, 295502. DOI: 10.1088/0953-8984/22/29/295502
- 134 Match! Phase Analysis using Powder Diffraction. URL: <https://www.crystalimpact.com/match/>. Accessed Jun 27, 2023.
- 135 Lindqvist P-A, and Uhrenius B. *Calphad*, **1980**, 4(3), pp. 193–200. DOI: 10.1016/0364-5916(80)90023-1
- 136 Chen YZ, Liu F, Yang GC, Xu XQ, and Zhou YH. *J. Alloys Compd.*, **2007**, 427, pp. L1–5. DOI: 10.1016/j.jallcom.2006.03.012
- 137 Chuang Y, Schmid R, and Chang Y. *Metall. Trans. A.*, **1984**, 15, pp. 1921–30. DOI: 10.1007/BF02664905
- 138 Wang CP, Liu XJ, Ohnuma I, Kainuma R, and Ishida K. *J. Phase Equilibria Diffus.*, **2004**, 25, pp. 320–8. DOI: 10.1007/s11669-004-0150-5
- 139 Curiotto S, Greco R, Pryds NH, Johnson E, and Battezzati L. *Fluid Phase Equilibria*, **2007**, 256, pp. 132–6. DOI: 10.1016/j.fluid.2006.10.003
- 140 Okamoto H: Binary Alloy Phase Diagrams. 2nd ed. **1990**: ASM International.
- 141 Xiong W, Selleby M, Chen Q, Odqvist J, and Du Y. *Crit. Rev. Solid State Mater. Sci.*, **2010**, 35(2), pp. 125–52. DOI: 10.1080/10408431003788472
- 142 Prokhorov NN. Elements of the metal physics and crystallization process. In *Physical Processes in Metals in Welding*, 1st ed.; Metallurgy: Moscow, Russia, **1968**; vol. 1, p. 695.
- 143 Tiller WA, and Rutter JW. *Canad. J. Phys.* **1956**, 31, 96.
- 144 Pfann WG. *Trans. AIME* **1952**, 194, 747.
- 145 Tiller WA. *J. Appl. Phys.* **1958**, 29, 611.

- 146 Grigoryants AG. The fundamentals of a laser treatment of materials. *Mosc. Mech. Eng.* **1989**, pp. 80–4. ISBN: 5-217-00432-0
- 147 Rykalin NN. The Calculation of the Heat Process for Welding; The State Scientific-Technical Publishing of the Mechanical Engineering Literature: Moscow, Russia, **1951**, p. 296.
- 148 Prokoshkina D, Rodin A, and Esin V. *Defect Diffus. Forum* **2012**, *323*, 171–76. DOI: 10.4028/www.scientific.net/DDF.323-325.171
- 149 Samuel M, Tetenov A, and Vaulin D. **2017** *Siberian Electronic Mathematical Reports* *14*, pp. 737–51. DOI: 10.17377/semi.2017.14.063
- 150 Nani K, Kumar N, Sharma A, and Bhargava MK. *Indian Foundry J.* **2014**, *60*, 23–7.
- 151 Goulart PR, Osório WR, Spinelli JE, and Garcia A. *Mater. Manuf. Process.* **2007**, *22*, 328–32. DOI: 10.1080/10426910701190345
- 152 Osório WR, and Garcia A. *Mater. Sci. Eng. A* **2002**, *325(1-2)*, 103–11. DOI: 10.1016/S0921-5093(01)01455-1
- 153 Sun J, and Lu S. *Scr. Mater.* **2020**, *186*, 174–9. DOI: 10.1016/j.scriptamat.2020.05.021
- 154 Wang Y, Li S, Yang B, Liu Z, Zhong H, Xing H, and Wang H. *Mater. Sci. Eng. A* **2020**, *771*, 138665. DOI: 10.1016/j.msea.2019.138665
- 155 Liao H, Sun Y, and Sun G. *Mater. Sci. Eng. A* **2002**, *335*, 62–6. DOI: 10.1016/S0921-5093(01)01949-9
- 156 Mudassar AA, and Butt S. *Opt. Lasers Eng.*, **2016**, *87*, pp. 156–67. DOI: 10.1016/j.optlaseng.2015.10.002
- 157 Bartlett JL, Croom BP, Burdick J, Henkel D, and Li X. *Addit. Manuf.*, **2018**, vol. 22, pp. 1-12. DOI: 10.1016/j.addma.2018.04.025

- 158 Blaysat B, Hoefnagels JPM, Lubineau G, Alfano M, and Geers MGD. *Int. J. Solids Struct.*, **2015**, 55, pp. 79–91. DOI: 10.1016/j.ijsolstr.2014.06.012
- 159 Hoult NA, Andy Take W, Lee C, and Dutton M. *Eng. Struct.*, **2013**, 46, pp. 718–26. DOI: 10.1016/j.engstruct.2012.08.018
- 160 Thäsler T, Holtmannspötter J, and Gudladt H-J. *J. Adhes.*, **2013**, 95(5-7), pp. 595–613. DOI: 10.1080/00218464.2018.1562923
- 161 Reiner J, Torres JP, and Veidt M. *Eng. Fract. Mech.*, **2017**, 173, pp. 107–17. DOI: 10.1016/j.engfracmech.2016.12.022
- 162 International Association of Classification Societies (IACS). Test specimens and mechanical testing procedures for materials. Electronic source. URL: <https://iacs.org.uk/download/13539>. Accessed Jun 27, 2022.
- 163 Toupin RA. On St. Venant's principle. In: Görtler H. (eds) *Applied Mechanics*. Springer, Berlin, Heidelberg, **1966**, pp. 151-2.
- 164 INSTRON 5900 Series Universal Testing Systems up to 50 kN. 5900 Series Premier Testing Systems Brochure. URL: <https://www.instron.com/-/media/literature-library/products/2012/12/5900-series-general-brochure.pdf?la=en>. Accessed 22 Aug 2021
- 165 I. Sen, E. Amankwah, N.S. Kumar, E. Fleury, K. Oh-ishi, K. Hono, and U. Ramamurty. *Mater. Sci. Eng. A*, **2011**, 528, pp. 4491–9. DOI: 10.1016/j.msea.2011.02.019
- 166 Zhang X, Pan T, Flood A, Chen Y, Zhang Y, and Liou F. *Mater. Sci. Eng., A*, **2021**, 811, 141071. DOI: 10.1016/j.msea.2021.141071
- 167 Liu ZH, Zhang DQ, Sing SL, Chua CK, and Loh LE. *Mater. Charact.*, **2014**, vol. 94, pp. 116–25. DOI: 10.1016/j.matchar.2014.05.001

- 168 Popovich A, Sufiiarov V, Polozov I, Borisov E, Masaylo D, and Orlov A. *Mater. Lett.*, **2016**, vol. 179, pp. 38–41. DOI: 10.1016/j.matlet.2016.05.064
- 169 Yang K, Li W, Guo X, Yang X, and Xu Y. *J. Mater. Sci. Technol.*, **2018**, 34, pp. 1570–9. DOI: 10.1016/j.jmst.2018.01.002
- 170 Tan C, Zhou K, Ma W, and Min L. *Mater. Des.*, **2018**, vol. 155, pp. 77–85. DOI: 10.1016/j.matdes.2018.05.064
- 171 Azinpour E, Darabi R, De Sa JC, Santos A, Hodek J, and Dzugan J. *Finite Elements Anal. Des.*, **2020**, 177, 103417. DOI: 10.1016/j.finel.2020.103417
- 172 Kersten S, Praniewicz M, Kurfess T, and Saldana C. *Procedia Manuf.*, **2020**, 48, pp. 730–6. DOI: 10.1016/j.promfg.2020.05.106
- 173 Sprague E. Characterization of Direct Metal Deposition Printed Copper-Iron Alloys. A dissertation. University of Michigan, 2022.
- 174 Zhang K, Wang S, Liu W, and Shang X. *Mater. Des.*, **2014**, 55, pp. 104–19. DOI: 10.1016/j.matdes.2013.09.006
- 175 Park S-H, Liu P, Yi K, Choi G, Jhang K-Y, and Sohn H. *Int. J. Machine Tools Manuf.*, **2021**, 166, 103745. DOI: 10.1016/j.ijmachtools.2021.103745
- 176 Yin YJ, Sun JQ, Guo J, Kan XF, and Yang DC. *Mater. Sci. Eng. A*, **2019**, 744, pp. 773–7. DOI: 10.1016/j.msea.2018.12.092
- 177 Al Mangour B, Kim Y-K, Grzesiak D, and Lee K-A. *Comp. Part B*, **2019**, 156, pp. 51–63. DOI: 10.1016/j.compositesb.2018.07.050
- 178 Zafari A, and Xia K. *Mater. Res. Lett.*, **2021**, 9(6), pp. 247–54. DOI: 10.1080/21663831.2021.1884620

- 179 Tan C, Chew Y, Duan R, Weng F, Sui S, Lan Ng F, Du Z, and Bi G. *Mater. Res. Lett.*, **2021**, 9, pp. 291–9. DOI: 10.1080/21663831.2021.1904299
- 180 Chen M, Khan HA, Wan Z, Lippert J, Sun H, Shang S-L, Liu Z-K, and Li J. *Addit. Manuf.*, **2020**, 32, 101037. DOI: 10.1016/j.addma.2020.101037
- 181 Koga N, Tomono S, and Umezawa O. *Mater. Sci. Eng. A*, **2021**, 811, 141066. DOI: 10.1016/j.msea.2021.141066
- 182 Becker TH, Kumar P, and Ramamurty U. *Acta Mater.*, **2021**, 219, 117240. DOI: 10.1016/j.actamat.2021.117240
- 183 Zhang X, Sun C, Pan T, Flood A, Zhang Y, Li L, and Liou F. *Addit. Manuf.*, **2020**, 36, 101474. DOI: 10.1016/j.addma.2020.101474
- 184 Khalid Imran M, Masood SH, Brandt M, Bhattacharya S, and Mazumder J. *Mater. Sci. Eng. A*, **2011**, 528, pp. 3342–9. DOI: 10.1016/j.msea.2010.12.099
- 185 Shi H, Duan L, Tan S, and Fang X. *J. Alloys Compd.*, **2021**, 868, 159134. DOI: 10.1016/j.jallcom.2021.159134
- 186 Yakout M, Elbestawi MA, Veldhuis SC. A study of thermal expansion coefficients and microstructure during selective laser melting of Invar 36 and stainless steel 316L. *Addit. Manuf.* **2018**, 24, 405–18. DOI: 10.1016/j.addma.2018.09.035
- 187 Pavlovic AS, Suresh Babu V, and Seehra MS. *J. Phys. Condens. Matter* **1996**, 8, 3139–49. DOI: 10.1088/0953-8984/8/18/007
- 188 Ferreira AJM, Batra RC, Roque CMC, Qian LF, and Martins PALS. *Compos. Struct.* **2005**, 69, pp. 449–57. DOI: 10.1016/j.compstruct.2004.08.003

- 189 Large-Area Picosecond Photo-Detectors Project Database. Chapter 17. Material Expansion Coefficients. Linear Thermal Expansion Coefficients of Metals and Alloys//The University of Chicago, Argonne, Fermilab and Berkeley. Electronic source. URL: [https://psec.uchicago.edu/thermal\\_coefficients/cte\\_metals\\_05517-0143.pdf](https://psec.uchicago.edu/thermal_coefficients/cte_metals_05517-0143.pdf). Accessed March 14, 2022.
- 190 AZo Materials. High-Leaded Tin Bronze UNS C93200. Electronic source. URL: <http://www.azom.com/article.aspx?ArticleID=6552>. Accessed May 26, 2022.
- 191 Dubenko IS, Gaidukova IYu, Granovsky SA, Gratz E, Gurjazkas D, Markosyan AS, and Müller H. *Solid State Commun.* **1997**, *103*, 495–9. DOI: 10.1016/S0038-1098(97)00215-9.
- 192 Chung Y-L, and Chang H-X. *J. Therm. Stress.* **2008**, *31*, pp. 368–88. DOI: 10.1080/01495730801912397
- 193 Cheng L, Zhou S, and Gao M. *Mater. Sci. Eng. A* **2023**, *886*, 145637. DOI: 10.1016/j.msea.2023.145637
- 194 Dubinin ON, Chernodubov DA, Kuzminova YO, Shaysultanov DG, Akhatov IS, Stepanov ND, and Evlashin SA. *J. Mater. Process. Technol.* **2022**, *300*, 117393. DOI: 10.1016/j.jmatprotec.2021.117393
- 195 Cui S, and Jung I.-H. *Calphad* **2017**, *56*, pp. 241–59. DOI: 10.1016/j.calphad.2017.01.004.
- 196 Raghavan V. Cr-Cu-Fe (Chromium-Copper-Iron). *J. Phase Equilibria* **2004**, *25*, 544. DOI: 10.1007/s11669-004-0072-2

- 197 Fernee H, Nairn J, and Atrens A. *J. Mater. Sci. Lett.* **2011**, *20*, pp. 2213–5. DOI: 10.1023/A:1017989118686
- 198 Dreval LA, Turchanin MA, Abdulov AR, and Bondar AA. *Chem. Met. Alloys* **2010**, *3*, 132–9. DOI: 10.30970/cma3.0132.
- 199 Sato K. *J. Phys. D Appl. Phys.* **1993**, *26*, B77–84. DOI: 10.1088/0022-3727/26/8B/011
- 200 Tsymburskaya AT. *Izv. Vyss. Uchebnykh Zaved. Fizika* **1971**, *9*, pp. 141–144.
- 201 Semenov My, Kraposhin VS, Talis AL, and Simich-Lafitskii ND. *Metalloved. I Termicheskaya Obrab. Metalloved.* **2020**, *2*, pp. 8–17. DOI: 10.1007/s11041-020-00522-3
- 202 Wilthan B, Reschab H, Tanzer R, Schuetzenhoefer W, and Pottlacher G. *Int. J. Thermophys.* **2008**, *29*, pp. 434–44. DOI: 10.1007/s10765-007-0300-1
- 203 Kaschnitz E, Kaschnitz H, Schleutker T, Guelhan A, and Bonvoisin B. *High Temp. High Press.* **2017**, *40*, 27. DOI: 10.1007/s10765-019-2490-8
- 204 Fetni S, Enrici TM, Niccolini T, Tran HS, Dedry O, Duchêne L, Mertens A, Habraken AM. *Mater. Des.* **2021**, *204*, 109661. DOI: 10.1016/j.matdes.2021.109661
- 205 Kumar KS. *Mater. Today Proceed.* **2015**, *2*, pp. 2256–66. DOI: 10.1016/j.matpr.2015.07.246
- 206 Sayman O, Sen F, Celik E, and Arman Y. *Mater. Des.* **2009**, *30*, pp. 770–4. DOI: 10.1016/j.matdes.2008.06.004
- 207 Sun K, Li F, Rong C, and Zuo L. *J. Manuf. Process.* **2022**, *84*, pp. 162–73. DOI: 10.1016/j.jmapro.2022.10.004

- 208 Goll D, Schuller D, Martinek G, Kunert T, Schurr J, Sinz C, Schubert T, Bernthaler T, Riegel H, and Schneider G. *Addit. Manuf.* **2019**, 27, pp. 428–39. DOI: 10.1016/j.addma.2019.02.021
- 209 Nartu MSKKY, Jagetia A, Chaudhary V, Mantri SA, Ivanov E, Dahotre NB, Ramanujan RV, and Banerjee R *Scripta Mater.* **2020**, 187, pp. 30–6. DOI: 10.1016/j.scriptamat.2020.05.063
- 210 Hilzinger H-R, Tenbrink J. in: Buschow KHJ, Cahn RW, Flemings MC, Ilschner B, Kramer EJ, Mahajan SPBT-E of MS, Veysière T (Eds.). **2001** Elsevier, Oxford: 8679-8684.
- 211 Chaudhary V, Mantri SA, Ramanujan RV, and Banerjee R *Progress in Mater. Sci.* **2020**, 114, 100688. DOI: 10.1016/j.pmatsci.2020.100688
- 212 Henderson L, Zamora S, Ahmed TN, Belduque C, Tate J, Chen MY, and Geerts WJ. *J. Magnetism Magnetic Mater.* **2021**, 538, 168320. DOI: 10.1016/j.jmmm.2021.168320
- 213 Bernier F, Ibrahim M, Mihai M, Thomas Y, and Lammare J-M. *Metal Powder Report.* **2020**, 75(6), pp. 334–43. DOI: 10.1016/j.mprp.2019.12.002
- 214 Dubinin ON, Chernodubov DA, Kuzminova YO, Shaysultanov DG, Akhatov IS, Stepanov ND, and Evlashin SA. *J. Mater. Process. Technol.* **2022**, 300, 117393. DOI: 10.1016/j.jmatprotec.2021.117393
- 215 Yadav S, Paul CP, Rai AK, Jinoop AN, Nayak SK, Singh R, and Bindra KS *J. Micromanuf.* **2022**, 5(1), pp. 21–8. DOI: 10.1177/25165984211047525
- 216 Todaro CJ, Easton MA, Qui D, Zhang D, Bermingham MJ, Lui EW, Brandt M, StJohn DH, and Qian M *Nature Comm.* **2020**, 11, 142. DOI: 10.1038/s41467-019-13874-z

- 217 Zhang D, Li Y, Wang H, and Cong W *J. Manuf. Process.* **2020**, *60*, pp. 328–39. DOI: 10.1016/j.jmapro.2020.10.058
- 218 Yan S, Wu D, Huang Y, Liu N, Zhang Y, Niu F, and Ma G *Mater. Lett.* **2019**, *235*, pp. 228–31. DOI: 10.1016/j.matlet.2018.10.047
- 219 Espacenet Patent search. KR101820719B1 DED Metal Reinforcement Method of Direct Energy Deposition Using Ultrasonic Wave Excitation [Internet]. 2018. URL: <https://worldwide.espacenet.com/patent/search/family/058742114/publication/KR101820719B1?q=pn%3DKR101820719B1>. Accessed Nov 12, 2021.
- 220 Espacenet Patent search. CN109604603A Ultrasonic-assisted laser-deposition additive manufacturing method and device [Internet]. 2020. URL: <https://worldwide.espacenet.com/patent/search/family/066021766/publication/CN109604603A?q=pn%3DCN109604603A>. Accessed Nov 12, 2021.
- 221 Paduani C, and Fonseca RE. *J. Magnetism Magnetic Mater.* **2003**, *263(1–2)*, pp. 93–100. DOI: 10.1016/S0304-8853(02)01541-X
- 222 Lake Shore Cryotronics. 7400 Series VSM. Electronic source. URL: <https://www.lakeshore.com/products/categories/overview/discontinued-products/discontinued-products/7400-series-vsm>. Accessed Jun 27, 2023.
- 223 Iquebal AS, Yadav A, Botcha B, Gorthi RS, and Bukkapatnam S. *Manuf. Lett.* **2022**, *33*, pp. 692–700. DOI: 10.1016/j.mfglet.2022.07.086
- 224 Noecker FF, and DuPont JN. International Congress on Applications of Lasers & Electro-Optics, **2002**. DOI:10.2351/1.5066217

- 225 Svetlizky D, Das M, Zheng B, Vyatskikh AL, Bose S, Bandyopadhyay A, Schoenung JM, Lavernia EJ, and Eliaz N. *Mater. Today*. **2021**, *49*, pp. 271–95. DOI: 10.1016/j.mattod.2021.03.020
- 226 Wang W, Takata N, Suzuki A, Kobashi M, and Kato M. *Intermetallics* **2020**, *125*, 106892. DOI: 10.1016/j.intermet.2020.106892
- 227 Nartu MSKKY, Dasari S, Sharma A, Chaudhary V, Varahabhatla SM, Mantri SA, Ivanov E, Ramanujan RV, Dahotre NB, and Banerjee R. *J. Alloys Compd.* **2021**, 861, 157998. DOI: 10.1016/j.jallcom.2020.157998
- 228 Gao S, Yan X, Chang C, Aubry E, He P, Liu M, Liao H, and Fenineche N. *Mater. Lett.* **2021**, *290*, 129469. DOI: 10.1016/j.matlet.2021.129469
- 229 Curiale J, Granada M, Troiani HE, Sanchez RD, Leyva AG, Levy P, and Samwer K *Appl. Phys. Lett.* **2009**, *95*, 043106. DOI: 10.1063/1.3187538
- 230 Shull RD, Okamoto H, and Beck PA *Solid State Comm* **1976**, *20*, pp. 863–68.
- 231 Wang XH, Liu SS, Zhao GL, Zhang M, and Ying WL. *Opt. Las. Technol.* **2021**, *136*, 106746. DOI: 10.1016/j.optlastec.2020.106746
- 232 Todaro CJ, Easton MA, Qui D, Zhang D, Birmingham MJ, Lui EW, Brandt M, StJohn DH, and Qian M. *Nature Comm.* **2020**, *11*, 142. DOI: 10.1038/s41467-019-13874-z
- 233 Zhang D, Li Y, Wang H, and Cong W. *J. Manuf. Processes* **2020**, *60*, pp. 328–39. DOI: 10.1016/j.jmapro.2020.10.058
- 234 Espacenet Patent search. KR101820719B1 DED Metal Reinforcement Method of Direct Energy Deposition Using Ultrasonic Wave Excitation. 2018. Electronic source.

- URL:<https://worldwide.espacenet.com/patent/search/family/058742114/publication/KR101820719B1?q=pn%3DKR101820719B1>. Accessed Nov 12, 2021.
- 235 Zhang Y, Guo Y, Chen Y, Kang L, Cao Y, Qi H, and Yang S. *Metals*. **2019**, 9, 1111. DOI: 10.3390/met9101111
- 236 Yan S, Wu D, Huang Y, Liu N, Zhang Y, Niu F, and Ma G. *Mater. Lett.* **2019**, 235, 228–31. DOI: 10.1016/j.matlet.2018.10.047
- 237 Espacenet Patent search. CN109604603A Ultrasonic-assisted laser-deposition additive manufacturing method and device. 2020. Electronic source. URL: <https://worldwide.espacenet.com/patent/search/family/066021766/publication/CN109604603A?q=pn%3DCN109604603A>. Accessed Nov 12, 2021.
- 238 Gorunov AI. Development of the science and technological basics of creating materials with enhanced physicomechanical and exploitational properties via the DED [thesis]. Saint Petersburg: Peter the Great St. Petersburg Polytechnic University; **2021**.
- 239 Zhang K, Wang S, Liu W, and Shang X. *Mater. Des.* **2014**, 55, pp. 104–19. DOI: 10.1016/j.matdes.2013.09.006
- 240 Guo P, Zou B, Huang C, and Gao H. *J. Mater. Process. Technol.* **2017**, 240, pp. 12–22. DOI: 10.1016/j.jmatprotec.2016.09.005
- 241 Azinpour E, Darabi R, Cesar de Sa J, Santos A, Hodek J, and Dzugan J. *Finite Elements in Analysis and Design*. **2020**, 177, 103417. DOI: 10.1016/j.finel.2020.103417
- 242 Stepinski T, and Wu P. *AIP Conf. Proc.* **1999**, 497, 431. DOI: 10.1063/1.1303084
- 243 Riedel E, Liepe M, and Scharf S. *Metals*. **2020**, 10, 476. DOI: 10.3390/met10040476
- 244 Suslick KS, and Neis U. *Scientific American*. **1989**, 260, pp. 80–6.

245 Lijun W, Weiguo Z, Huier C, Yunlong S, and Xiaojing L. *Appl. Mathem. Modelling*, **2007**, *31*, pp. 1249–62. DOI: 10.1016/j.apm.2006.04.016

246 Mohanty TR, Sahoo SK, and Moharana MK. *Proc. Eng.* **2015**, *127*, pp. 940–6. DOI: 10.1016/j.proeng.2015.11.440

247 Kumar A, Bansal SN, and Chandraker R. *Mater. Phys. Mechan.* **2012**, *15*, pp. 46–65.

## Appendix

The appendix includes Figures S.1–S.17, which demonstrate engineering stress-strain curves of all the specimens tested by the mechanical analysis. They also contain the hatched triangles, which areas refer to the specific energy of the proportional strain.

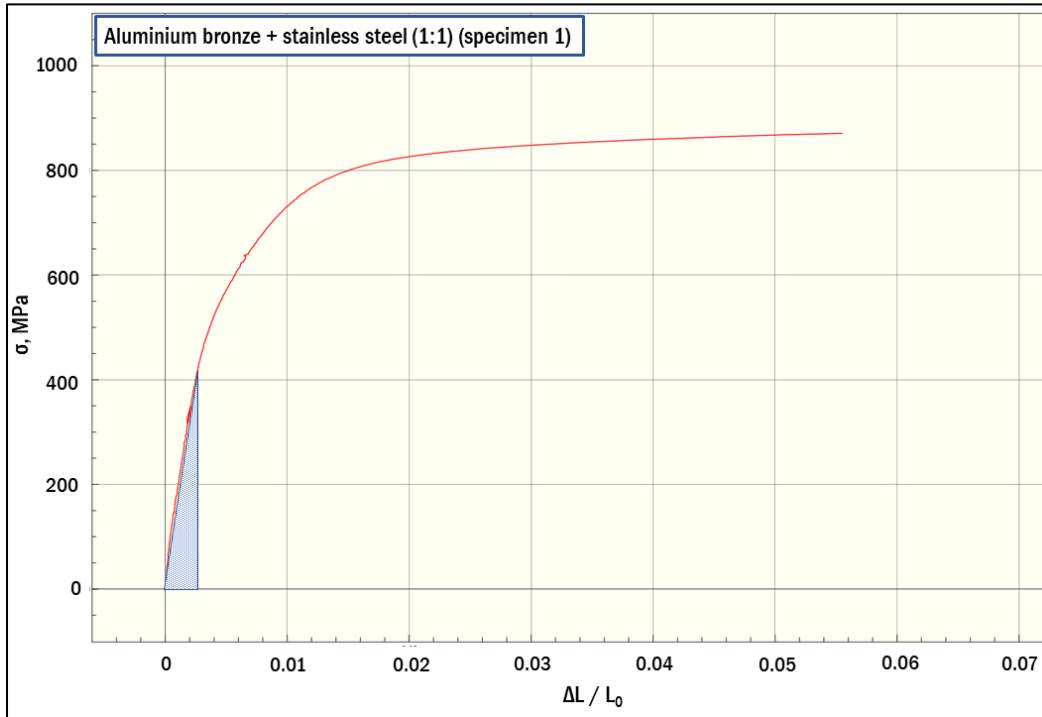


**Figure S.1** – Engineering stress-strain curve of C61800 + SS 316L (50/50 wt.%) (group 1, specimen 1).

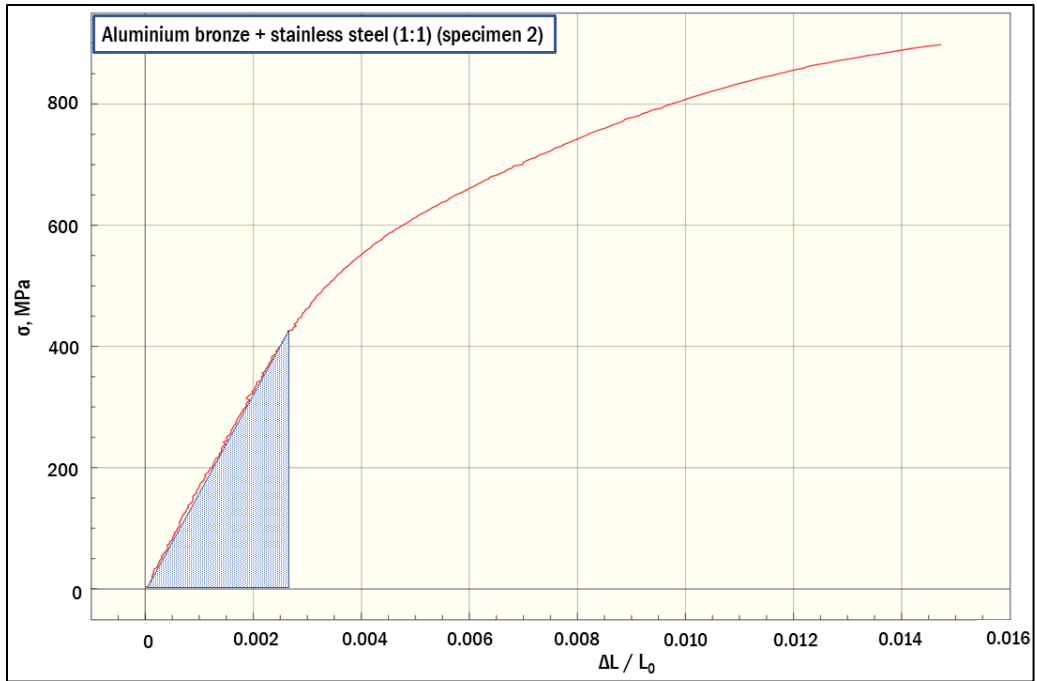


**Figure S.2** – Engineering stress-strain curve of C61800 + SS 316L (50/50 wt.%) (group 1, specimen 2).

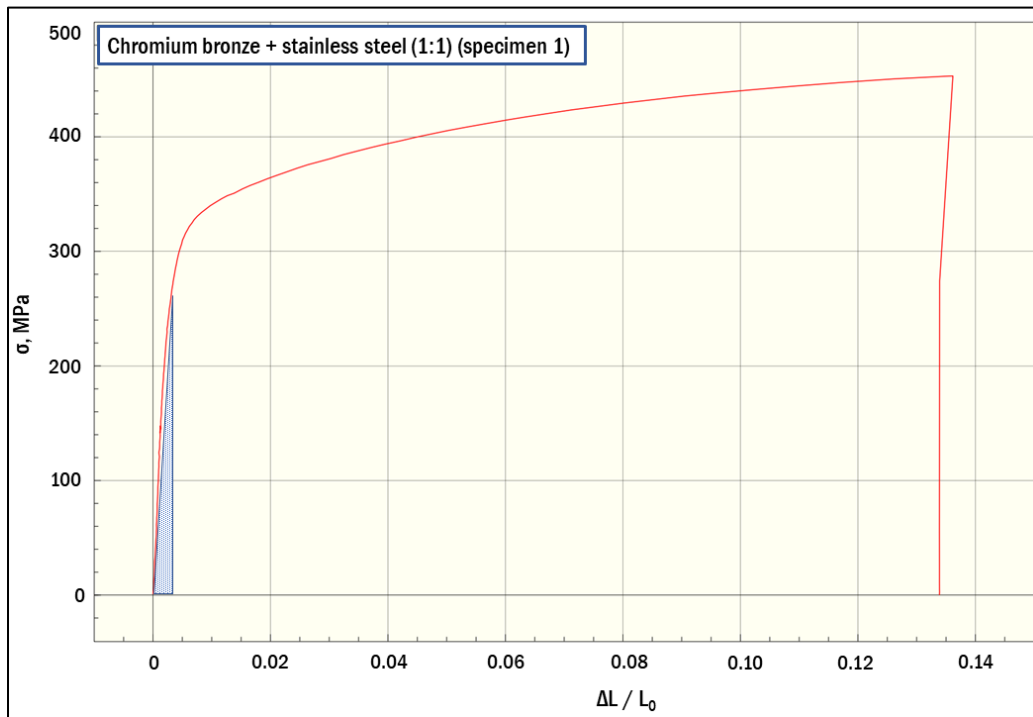


**Figure S.3** – Engineering stress-strain curve of C18400 + SS 316L (50/50 wt.%) (group 2, specimen 1).

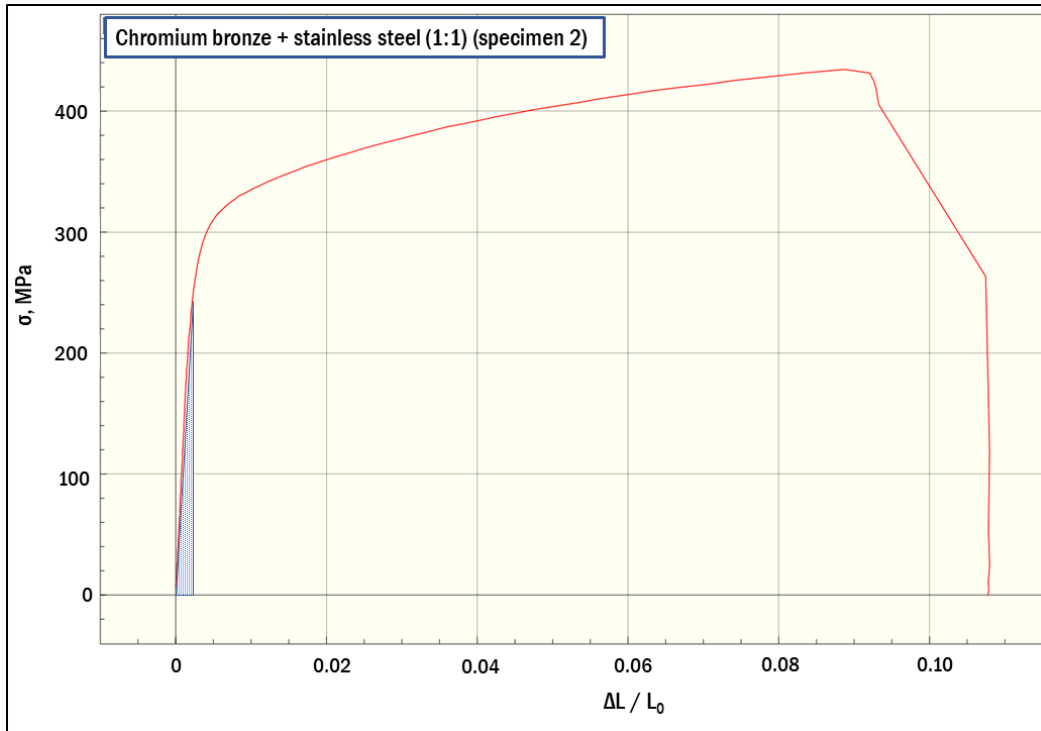


**Figure S.4** – Engineering stress-strain curve of C18400 + SS 316L (50/50 wt.%) (group 2, specimen 2).

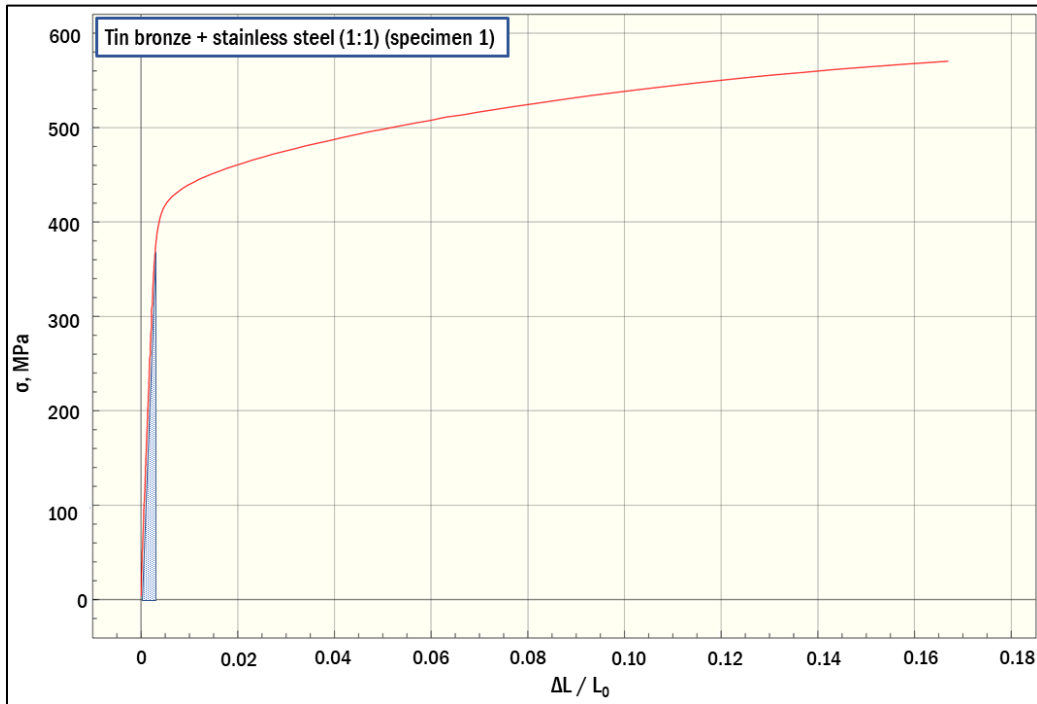


**Figure S.5** – Engineering stress-strain curve of CB480K + SS 316L (50/50 wt.%) (group 3, specimen 1).

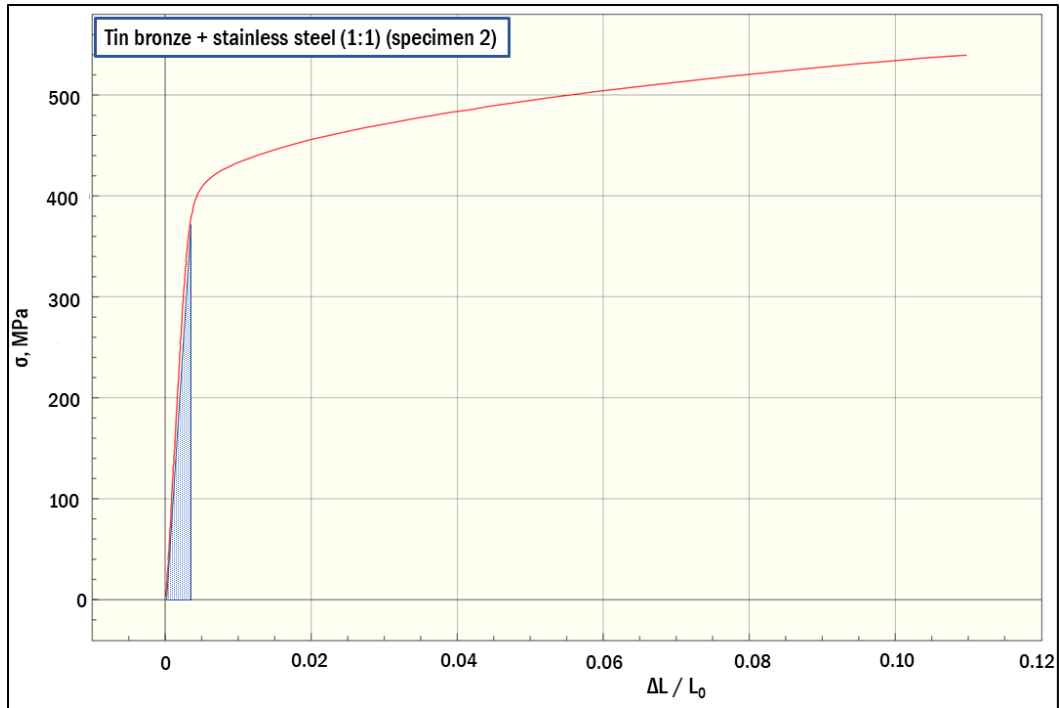


Figure S.6 – Engineering stress-strain curve of CB480K + SS 316L (50/50 wt.%) (group 3, specimen 2).

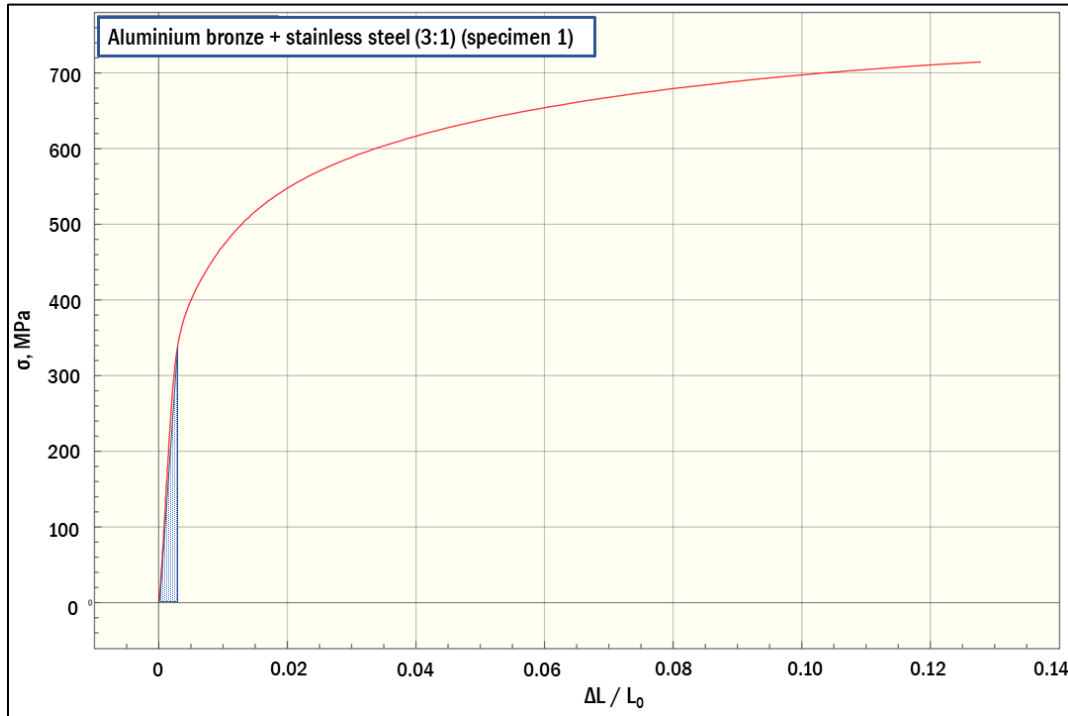


Figure S.7 – Engineering stress-strain curve of C61800 + SS 316L (75/25 wt.%) (group 4, specimen 1).

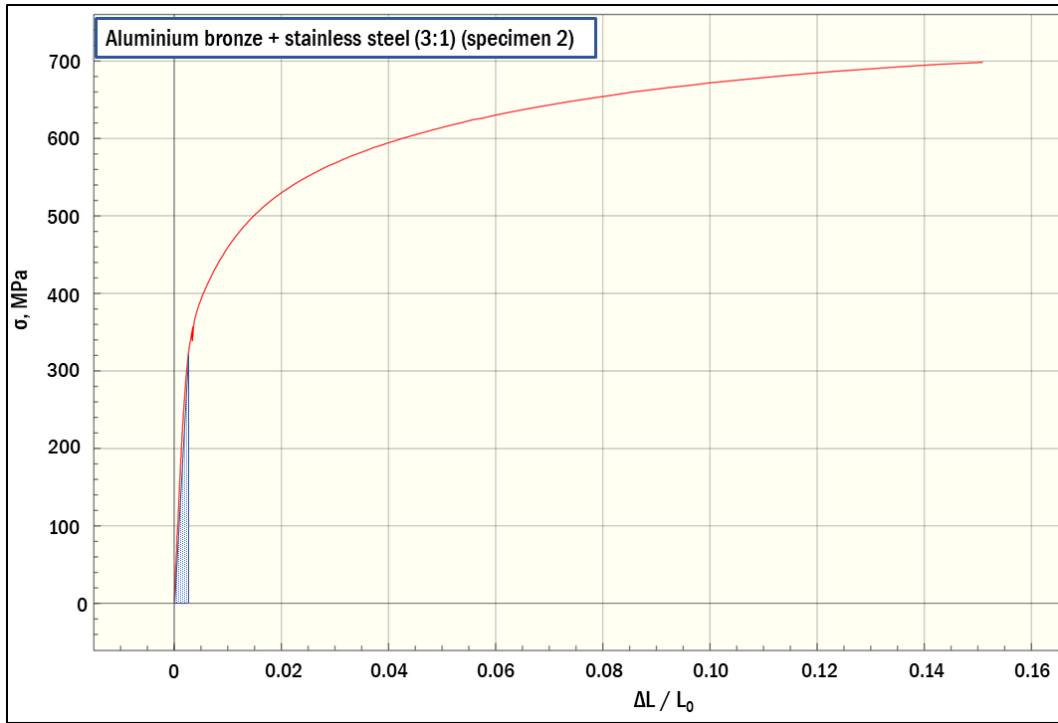


Figure S.8 – Engineering stress-strain curve of C61800 + SS 316L (75/25 wt.%) (group 4, specimen 2).

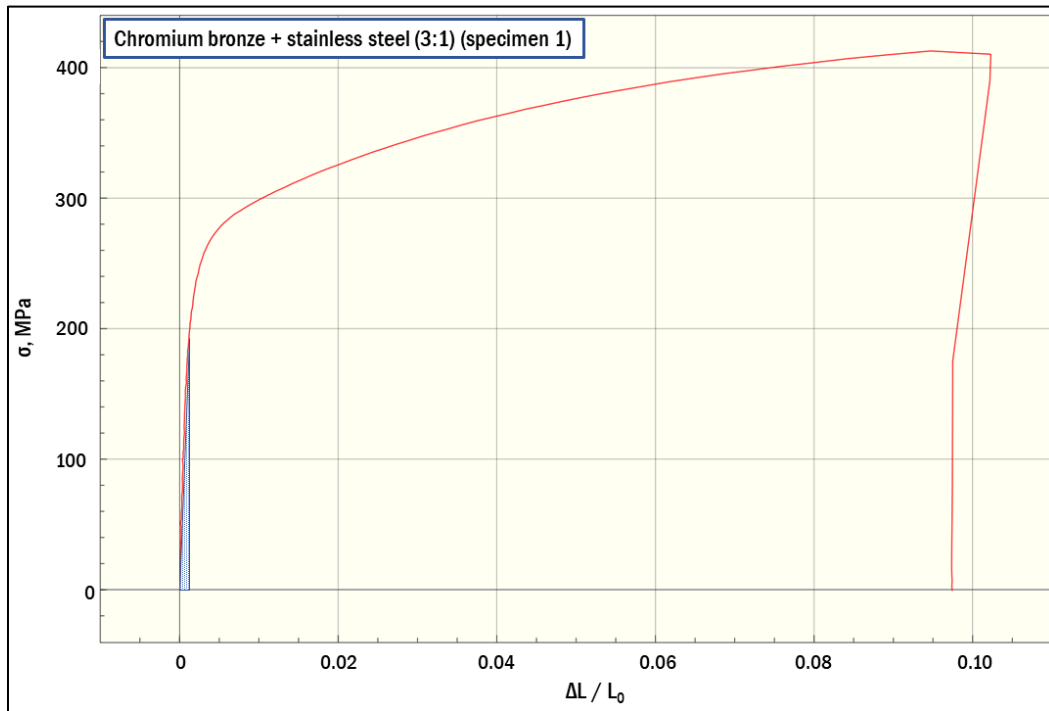
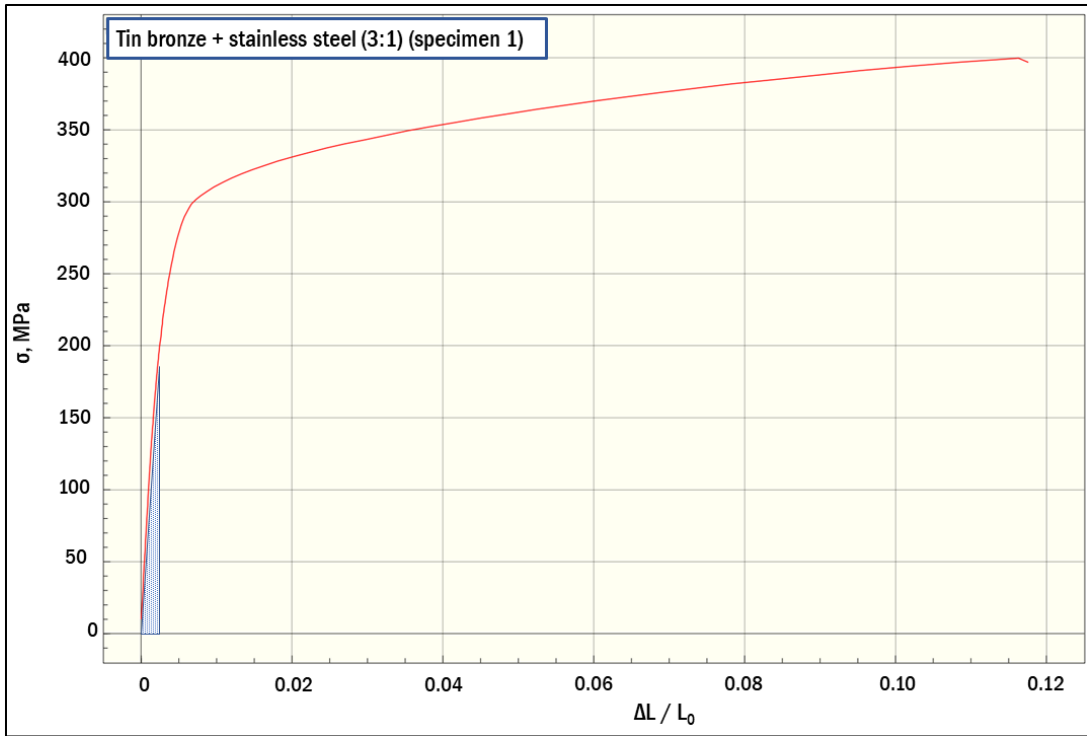
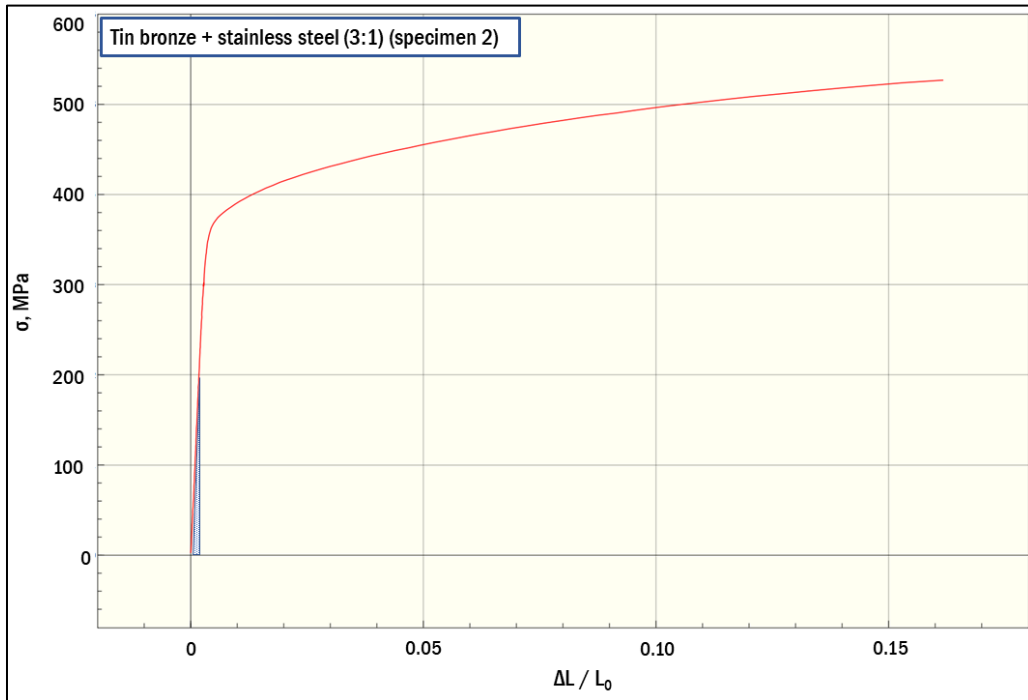


Figure S.9 – Engineering stress-strain curve of C18400 + SS 316L (75/25 wt.%) (group 5, specimen 1).



**Figure S.10** – Engineering stress-strain curve of CB480K + SS 316L (75/25 wt.%) (group 6, specimen 1).



**Figure S.11** – Engineering stress-strain curve of CB480K + SS 316L (75/25 wt.%) (group 6, specimen 2).

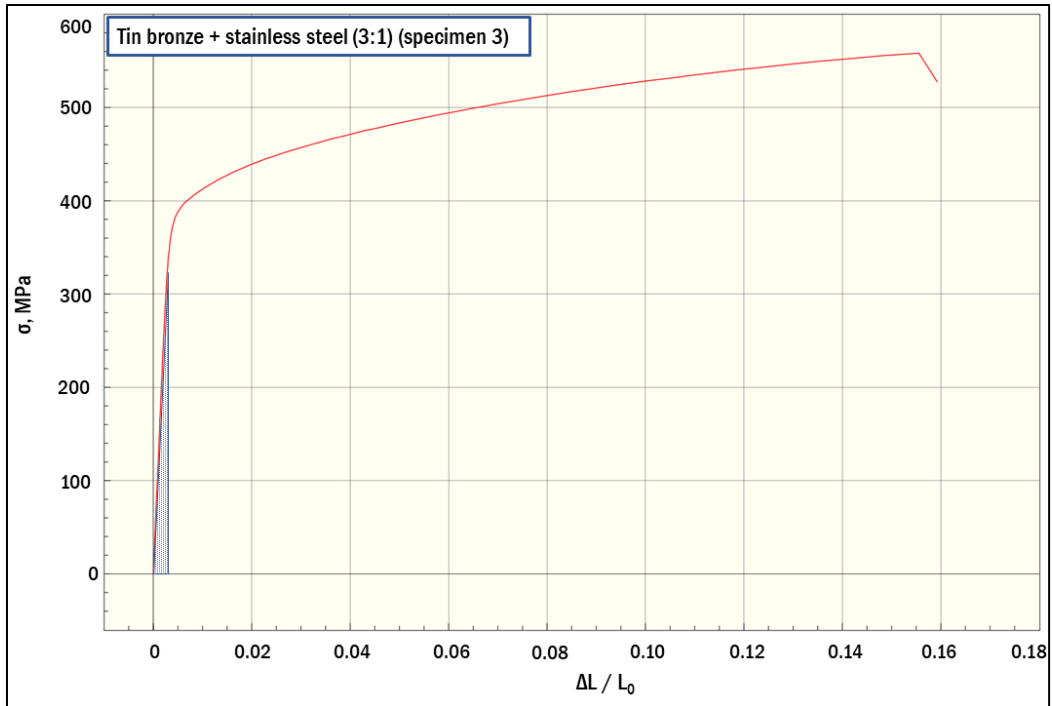


**Figure S.12** – Engineering stress-strain curve of CB480K + SS 316L (75/25 wt.%) (group 6, specimen 3).

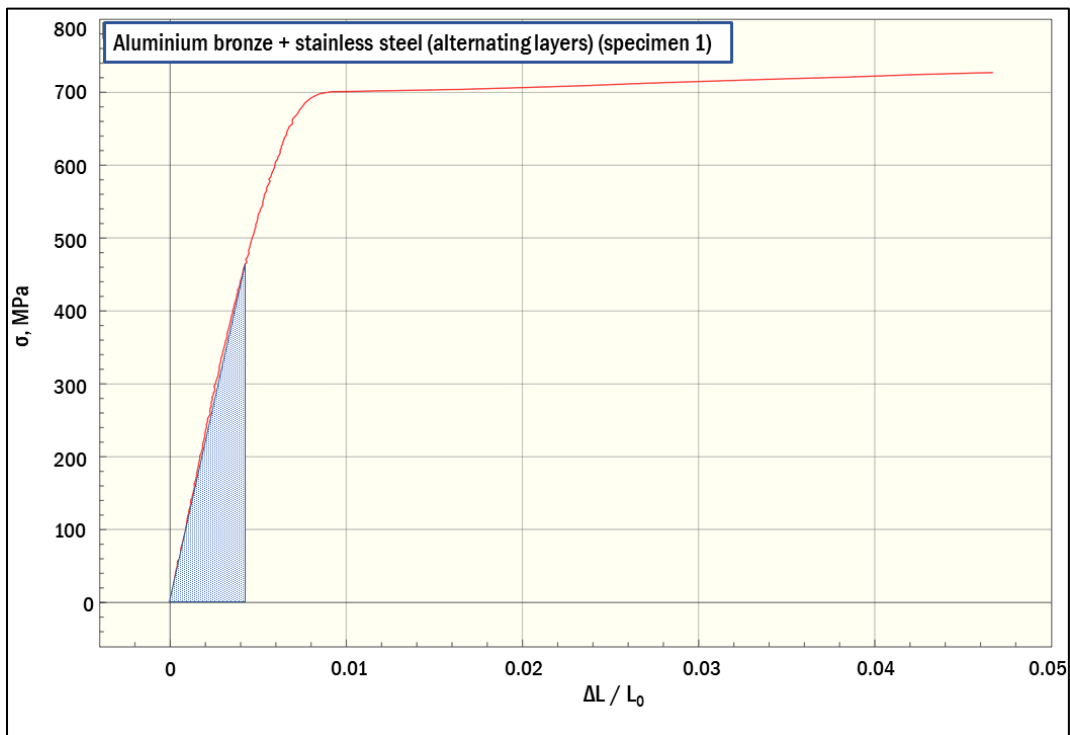


**Figure S.13** – Engineering stress-strain curve of C61800 + SS 316L (alt.) (group 7, specimen 1).

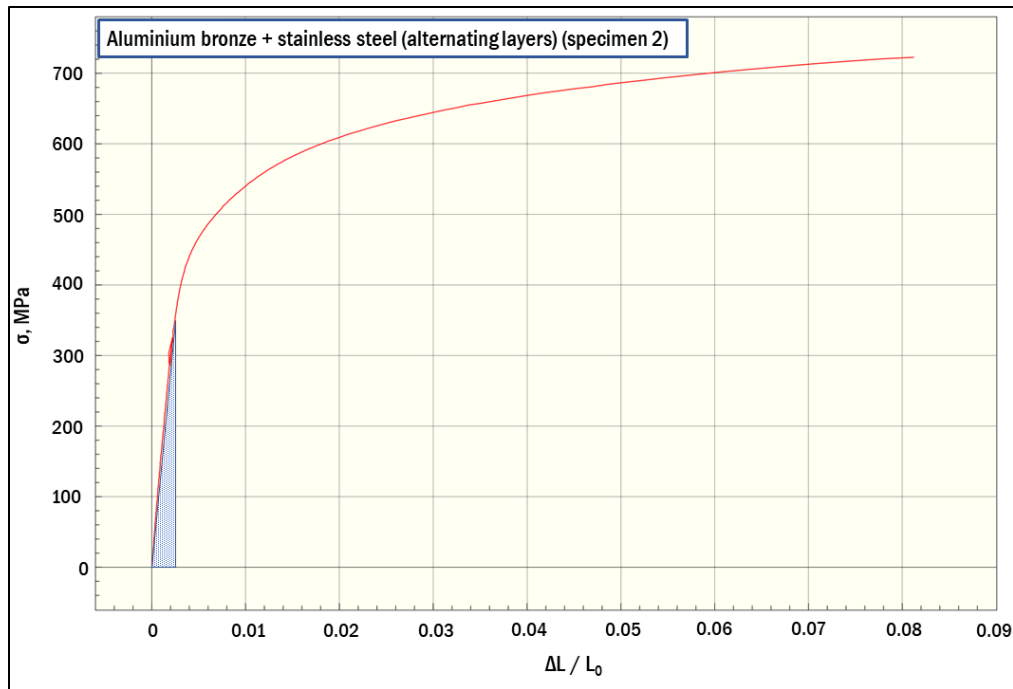


**Figure S.14** – Engineering stress-strain curve of C61800 + SS 316L (alt.) (group 7, specimen 2).

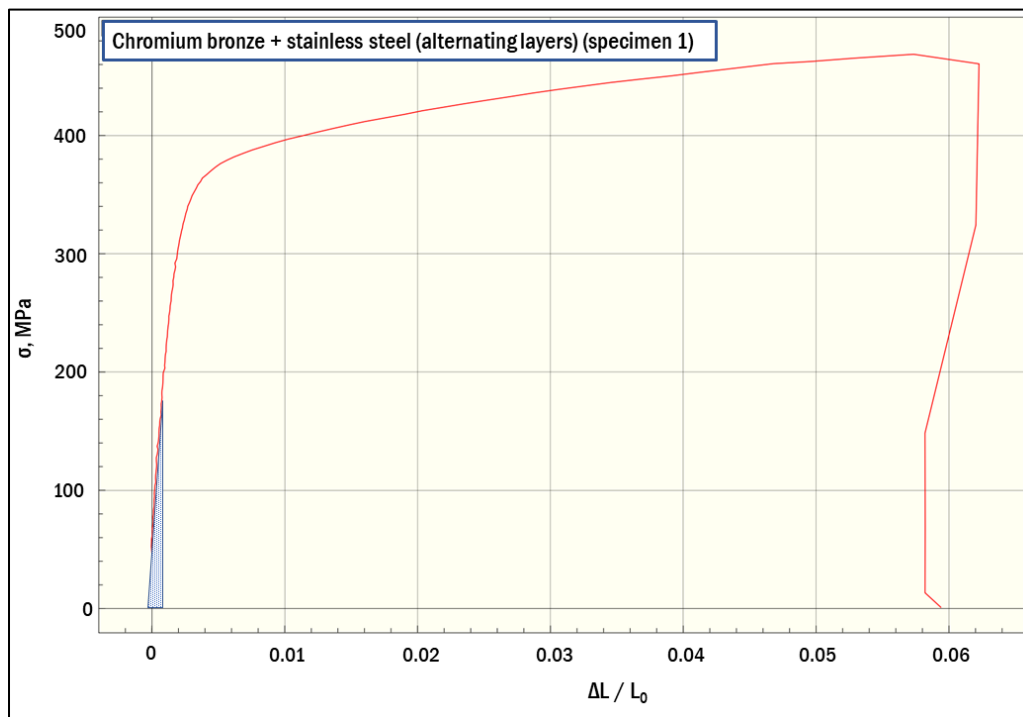


**Figure S.15** – Engineering stress-strain curve of C18400 + SS 316L (alt.) (group 8, specimen 1).

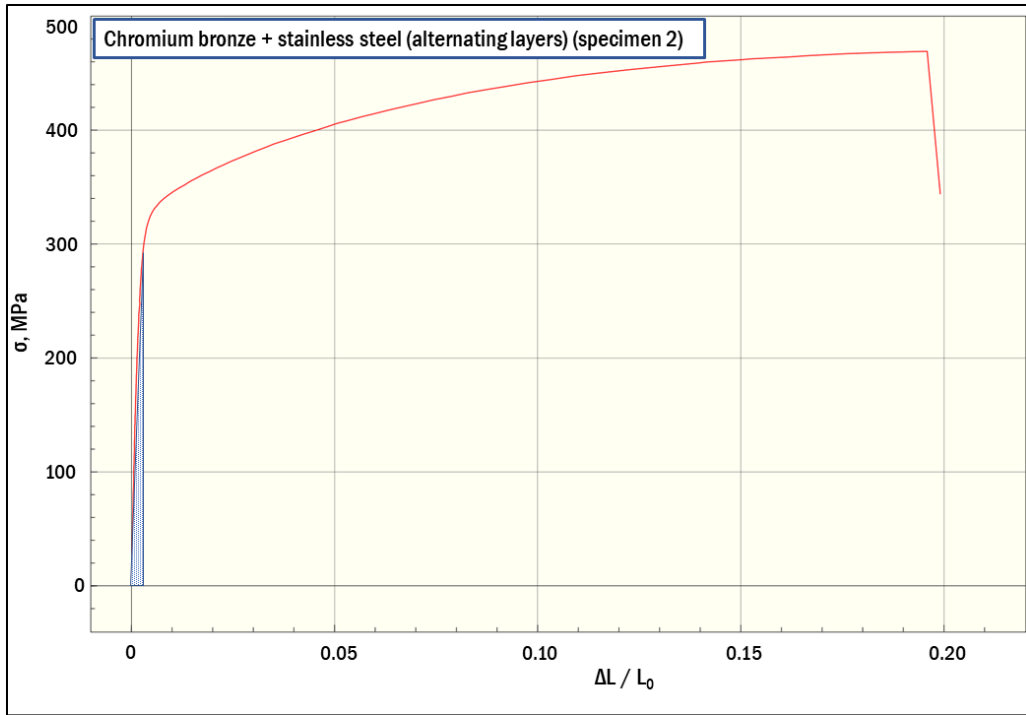


**Figure S.16** – Engineering stress-strain curve of C18400 + SS 316L (alt.) (group 8, specimen 2).

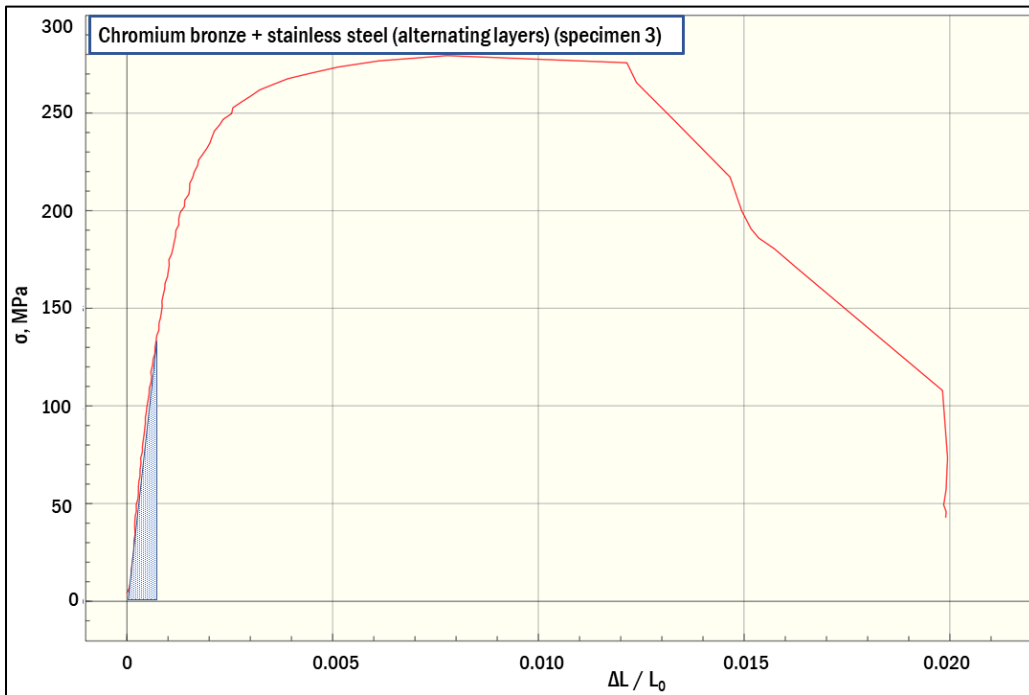


**Figure S.17** – Engineering stress-strain curve of C18400 + SS 316L (alt.) (group 8, specimen 3).

Table S.1 demonstrates the values of three strain tensor components determined from the results of tensile tests.

**Table S.1.** Max/min values of strain tensor components  $e_{xx}$ ,  $e_{xy}$ , and  $e_{yy}$  of all groups.

Component	Group 1	Group 2	Group 3	Group 4	Group 5	Group 6	Group 7	Group 8
$e_{xx}$	-0.0225	-0.045	-0.069	-0.06	-0.044	-0.066	-0.036	-0.0062
$e_{xy}$	0.0024	0.0031	0.0063	0.0046	0.0034	0.004	0.0029	-0.00028
$e_{yy}$	0.055	0.107	0.18	0.15	0.105	0.17	0.085	0.016